

University of Alberta Library



0 1620 3069297 2



EX LIBRIS
UNIVERSITATIS
ALBERTENSIS

The Bruce Peel
Special Collections
Library



Digitized by the Internet Archive
in 2025 with funding from
University of Alberta Library

<https://archive.org/details/0162030692972>

University of Alberta

Library Release Form

Name of Author: Scott Edward Irvine

Title of Thesis: High-Speed Magneto-Optic Modulation and Beam Deflection

Degree: Masters of Science

Year this Degree Granted: 2002

Permission is hereby granted to the University of Alberta Library to reproduced single copies of this thesis and to lend or sell such copies for private, scholarly or scientific research purposes only.

The author reserves all other publication and other rights in association with the copyright in the thesis, and except as herein before provided, neither the thesis nor any substantial portion thereof may be printed or otherwise reproduced in any material form whatever without the author's prior written consent.

University of Alberta

HIGH-SPEED MAGNETO-OPTIC MODULATION AND BEAM DEFLECTION

by

Scott Edward Irvine



A thesis submitted to the Faculty of Graduate Studies and Research in partial fulfillment
of the requirement for the degree of Master of Science

Department of Electrical and Computer Engineering

Edmonton, Alberta

Fall 2002

University of Alberta

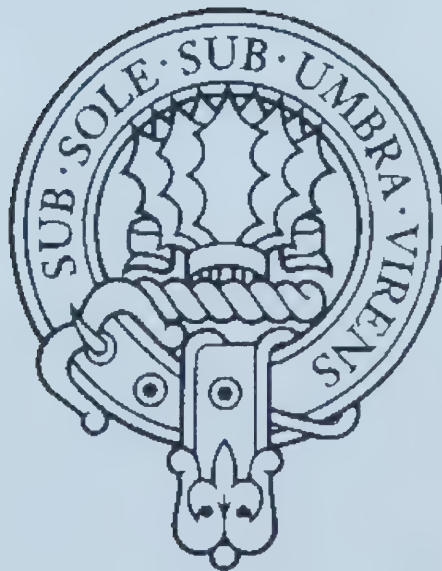
Faculty of Graduate Studies and Research

The undersigned certify that they have read, and recommended to the Faculty of Graduate Studies and Research for acceptance, a thesis entitled HIGH-SPEED MAGNETO-OPTIC MODULATION AND BEAM DEFLECTION submitted by Scott Edward Irvine in partial fulfillment of the requirement for the degree of Master of Science.

Acknowledgements

First of all I would like to thank my supervisor, Abdulhakem Y. Elezzabi, for his support, motivation, and guidance. Additionally I would like to thank my peers Jonathan F. Holzman and Michael D. Cummings for their assistance.

Equally important are the members of my family, who have given me everything: this thesis is truly dedicated to them.



Abstract

A high-speed magneto-optic (MO) modulation device based on the Faraday effect is designed and tested. The device utilizes a bismuth substituted yttrium iron garnet (Bi-YIG) thin film as an optical waveguide to modulate the polarization of a light-wave. Two operational modes of the device are demonstrated: resonant and non-resonant. Single frequency resonant modulation at a maximum frequency of 1.8 GHz is achieved, while non-resonant broadband modulation is established when electrical pulses as short as 2.3 ns are mapped onto an optical carrier. Moreover, the device demonstrates switching times as short as 343 ps.

The experimental work is complimented by a model that predicts the operation of the MO modulator. This model considers light wave propagation effects as well as the time evolution of the magnetization vector of the Bi-YIG film. Additionally, an MO beam deflector is proposed and analyzed using this model.

Table of Contents

1	Introduction	1
1.1	Thesis Objectives.....	2
1.2	Thesis Organization.....	2
1.3	Reference.....	3
2	Background.....	4
2.1	Magneto-Optic Effects and the Faraday Effect.....	4
2.1.1	The Faraday Effect.....	5
2.1.2	Origin of the Faraday Effect.....	11
2.2	Thin Film Bismuth Substituted Yttrium Iron Garnet.....	13
2.3	Time Evolution of the Magnetization in Ferromagnetic Materials.....	16
2.4	Diffraction from Magnetic Gratings	20
2.5	Review of Magneto-Optic Modulation and Beam Deflection.....	24
2.5.1	Magneto-Optic Modulation.....	24
2.5.2	Magneto-Optic Beam Deflection.....	29
2.5.3	Modeling of Passive Magneto-Optic Devices.....	31
2.6	References.....	32
3	Beam Propagation Method and Results.....	35
3.1	Beam Propagation in Magneto-Optic Materials.....	35
3.1.1	Derivation of the Beam Propagation Operators.....	36
3.1.2	Discretization of Beam Propagation Equations.....	41
3.2	Theoretical Modeling of the Magneto-Optic Modulator.....	47

3.2.1	Time-Independent Light Propagation in a Bulk Magneto-Optic Material.....	47
3.2.2	Geometry of the Magneto-Optic Modulator.....	49
3.2.3	Modeling of the Magneto-Optic Modulator at 1550 nm with Idealized Parameters.....	51
3.2.4	Effects of Birefringence on Static Mode Conversion at 800 nm.....	53
3.2.5	Magnetic Field due to a Transmission Line.....	57
3.2.6	Modeling of the Magneto-Optic Modulator at 800 nm with Experimental Parameters.....	61
3.3	Proposal of a High-Speed Magneto-Optic Beam Deflector.....	63
3.3.1	Geometry of the Magneto-Optic Beam Deflector.....	63
3.3.2	Concept of Magneto-Optic Beam Deflection.....	67
3.3.3	Theoretical Modeling of the Proposed Magneto-Optic Beam Deflector.....	68
3.4	Summary.....	76
3.5	References.....	76
4	Experimental Set-up and Results.....	78
4.1	Experimental Set-up for Magneto-Optic Modulation.....	78
4.1.1	The Magneto-Optic Modulator.....	78
4.1.2	Fabrication.....	80
4.1.3	The Transmission Line.....	81
4.1.4	Driving Electronics.....	81

4.1.5	The Lasers.....	83
4.1.6	The Optical Arrangement and Test Set-Up.....	83
4.1.7	Static Magnetic Field.....	87
4.1.8	Optical Alignment.....	88
4.2	Experimental Discussion and Results.....	89
4.2.1	Resonant Mode.....	89
4.2.2	Non-resonant Mode.....	97
4.2.3	Modulation Depth.....	113
4.3	Summary.....	114
4.4	References.....	114
5	Conclusion.....	116
5.1	References.....	120
Appendix A	Computer Algorithm for the BPM-LL Model.....	121
Appendix B	The Crank-Nicolson Discretization.....	143
Appendix C	Photodetectors and Circuits.....	145

List of Figures

2.1.	a) A light beam experiences a polarization rotation due to the Faraday effect when its passes through material having a net magnetization along the direction of propagation. b) The linear polarization of a wave traveling out of the page can be resolved into left and right circular polarizations.	6
2.2.	Ideal relationship between magnetization and applied magnetic field in a ferromagnetic material. After [2].	10
2.3.	Precessional motion of an electron in the presence of a static magnetic field and a perturbing magnetic field. The motion results in magnetization components m_x and m_y . After [5].	12
2.4.	a) The various lattice sites for a garnet crystal. b) The crystal lattice structure of garnet. After [7].	14
2.5.	A parametric plot of the temporal evolution of the magnetization for times ranging from -2.5 to 2.5 ns in response to a 20 mT, 1 ns FWHM Gaussian magnetic field pulse and DC magnetic field of 27.5 mT.	18
2.6.	The normalized z-component of the magnetization plotted in figure 2.5. Various biasing fields are used to illustrate the ferromagnetic precession of the magnetization.	19
2.7.	Schematic diagram of an MO phase grating. Even modes have polarization that is the same as that of the input beam while the odd modes have polarization that is orthogonal to that of the input beam.	22
2.8.	Ray analysis illustration of diffraction from an MO phase grating [6].	23

2.9.	Geometry of the MO modulator constructed by Le Craw. After [3,13].	25
2.10.	Experimental set-up used by Tien et al. [14], employing a Bi-YIG film as a waveguide MO modulator.	27
2.11.	Pump-probe arrangement used by Elezzabi and Freeman [10].	28
2.12.	Experimental arrangement employed by Prabhakar and Stancil [16].	30
3.1.	Geometrical light rays for a) TE and b) TM modes in a slab waveguide, and c) TE and d) TM modes in free space.	38
3.2.	Schematic representation of the matrices used for the beam propagation method.	45
3.3.	Propagation in a bulk material that has a non-zero Faraday rotation of 1.0 %/mm and index of refraction of 1. a) TE polarization , b) side view of the TE wave c) TM polarization , d) side view of the TM wave.	48
3.4.	Schematic diagram of the MO modulator.	50
3.5.	Static a) TE to b) TM mode conversion for constant magnetization along the z -direction. Complete mode conversion occurs at a distance of 396 μm .	52
3.6.	Simulated spatio-temporal output of the MO modulator corresponding to an input of three sequential current pulses at four selected FWHM of a) 1 ns, b) 200 ps, c) 100 ps, d) 50 ps.	54
3.7.	Effect of birefringence on TE (left hand column) to TM (right hand column) mode conversion for various values of index. a) $n_x=2.3$, $n_y=2.2602$, b) $n_x=2.3$, $n_y=2.259$, c) $n_x=2.3$, $n_y=2.25$.	56

3.8.	Cross-sectional view of a rectangular transmission line having width l and thickness d	58
3.9.	Spatial distribution of the magnitude of the magnetic field due to a transmission line of rectangular cross-section with $l=20\text{ }\mu\text{m}$, $d=2\text{ }\mu\text{m}$	60
3.10.	Time-dependent output of the MO modulator in response to an electrical input of a single 2.5 ns employing the actual transmission line structure. a) Time snapshot of the TM polarization throughout MO modulator. b) Time varying output of the MO modulator. $l=100\text{ }\mu\text{m}$, $d=60\text{ }\mu\text{m}$, $n_x=2.3$, $n_y=2.2602$, film thickness $a=0.25\text{ }\mu\text{m}$, Faraday rotation = 5400 %/cm.	62
3.11.	Schematic representation of a high-speed MO beam deflector. The proposed device is essentially a unit cell of the stripe diffraction grating depicted in figure 2.7.	64
3.12.	The distribution of the z -component of the magnetic field due to a single serpentine transmission line carrying a constant current of 1 A. For $d \gg l$, the magnetic field is uniform in the active region of the device.	66
3.13.	Diffraction pattern obtained with the time-independent BPM for a $20\text{ }\mu\text{m}$ thick stripe diffraction grating composed of alternating magnetizations for a wavelength of 633 nm, Faraday rotation of 11000 %/cm, and domain spacing $1.7\text{ }\mu\text{m}$. a) TE polarization, b) TM polarization.	69
3.14.	Time-independent deflected TM beam profile of the proposed MO beam deflector for a wavelength of 1550 nm and a Faraday rotation of 2500 %/cm. An outline indicating the boundaries of MO deflector is superimposed on the plot.	70

3.15.	The spatio-temporal distribution of the Faraday rotation due to a current transient in the transmission line at $z=75\text{ }\mu\text{m}$. The small oscillations near the trailing edge of the pulse are due to the ferromagnetic precession of the magnetization.	72
3.16.	Spatial snap shots of the output of the MO beam deflector showing the mode conversion and a subsequent TM diffraction pattern for a wavelength of 1550 nm. The MO deflector is driven with a 1 ns FWHM, 5 A (peak) Gaussian current pulse. The maximum response occurs at the peak of the current pulse at $t = 0\text{ ns}$. An outline indicating the boundaries of MO deflector is superimposed on the plot.	74
3.17.	Far-field spatio-temporal output (TM polarization) of the MO deflector taken at $z=300\text{ }\mu\text{m}$ in response to a 1 ns current pulse.	75
4.1.	a) Schematic diagram of the MO modulator. b) Picture of the MO modulator and surrounding set-up.	79
4.2.	Circuit used to differentiate 35 V steps to produce pulses.	82
4.3.	Experimental set-up used to test the MO modulator.	84
4.4.	Alternative experimental set-up employing balanced detection.	86
4.5.	Resonant output of the MO modulator for various driving signals at frequencies: (a) 1 MHz, (b) 50 MHz, (c) 200 MHz, (d) 500 MHz, (e) 750 MHz, and (f) 1 GHz. The corresponding biasing field strengths are measured to be (a) 6 mT, (b) 6.5 mT, (c) 8.5 mT, (d) 8 mT, (e) 14 mT, and (f) 20 mT.	90
4.6.	Impedance matching characteristics of the MO modulator.	92
4.7.	FMR frequency as a function of applied biasing magnetic field. Experimental values (circles and squares) and calculated values from Kittel's relation (dashed	

	line) are shown. For frequencies below 400 MHz (squares), the experimental data does not follow any obvious relation.	93
4.8.	The frequency response of the MO modulator for three individual FMR frequencies of 500 MHz, 750 MHz, and 1 GHz with biasing field strengths of 8, 14, and 20 mT, respectively.	96
4.9.	Single frequency modulation at 1.8 GHz.	98
4.10.	Pulse width: 1000 ns. Driving electrical pulse (top) and measured optical pulse (bottom). $b_y=6.8$ mT.	99
4.11.	Pulse width: 500 ns. Driving electrical pulse (top) and measured optical pulse (bottom). $b_y=6.8$ mT.	100
4.12.	Pulse width: 100 ns. Driving electrical pulse (top) and measured optical pulse (bottom). $b_y=6.8$ mT.	101
4.13.	Pulse width: 10 ns. Driving electrical pulse (top) and measured optical pulse (bottom). $b_y=7.8$ mT.	102
4.14.	Pulse width: 5 ns. Driving electrical pulse (top) and measured optical pulse (bottom). $b_y=8.2$ mT.	103
4.15.	Pulse width: 2.3 ns. Driving electrical pulse (top) and measured optical pulse (bottom). $b_y=15$ mT.	104
4.16.	Electrical input (dashed line) and optical output (solid line) of the MO modulator for a driving pulse with a FWHM=2.3 ns.	106
4.17.	The a) calculated and b) measured spectra of a 2.3 ns FWHM Gaussian-like electrical pulse. c) Display of the frequency characteristics of the MO modulator for $b_y=15$ mT.	107

4.18.	Several different outputs corresponding to the same electrical input, but for slight changes in the value of the static field, b_y	109
4.19.	a) Electrical driving pulse with a 10%-90% rise-time of 320 ps. Curves b), c), and d) show the corresponding MO modulator output for $b_y=22$, 39, and 52 mT, respectively.	110
4.20.	a) Frequency characteristics of the MO modulator, exhibiting a 1.5 GHz FMR for $b_y=30$ mT. Fourier power spectra of Gaussian pulses of various FWHM: b) 2 ns, c) 1 ns, d) 500 ps, e) 300 ps, and f) 100 ps.	112
C.1.	a) Mask used to create the circuit board. b) Circuit schematic for the photoreceiver module. c) Picture of the front and back of the enclosure containing the photoreceiver and its circuit board. d) Balanced diode circuit schematic.	146

List of Acronyms

a. u.	Arbitrary Units
Bi-YIG	Bimusth substituted Yttrium Iron Garnet
BPM	Beam Propagation Method
BPM-LL	Beam Propagation Method with Landau Lifshitz equation
CW	Continuous Wave
DC	Direct Current
FMR	Ferromagnetic Resonance
FWHM	Full Width at Half Maximum
GGG	Gadolinium Gallium Garnet
IG	Iron Garnet
ITO	Indium Tin Oxide
LL	Landau-Lifshitz equation
LPE	Liquid-Phase Epitaxy
MO	Magneto-Optic
PDE	Partial Differential Equation
RF	Radio Frequency
SMA	Subminiature version A
TE	Transverse Electric
TM	Transverse Magnetic
YIG	Yttrium Iron Garnet

Chapter 1

Introduction

Over the past several years the demand for high bandwidth networking has dramatically increased, encouraging the continued development of high-speed electrical and optical devices. A key device within this development is an optical modulator, which encodes electrical data on an optical carrier and, along with a host of other devices, allows large amounts of optical data to be transmitted through fiber-optic networks.

While the majority of current modulation techniques rely on the acousto-optic and electro-optic effects, very few modulation devices are based on the magneto-optic (MO) effect. Historically, this was due to the lack of MO materials with low infrared absorption and high Faraday rotations. However, with the discovery of bismuth substituted iron garnet films [1] came the promise of MO technologies with both a large Faraday rotation and low absorption in the infrared window. In addition to this, MO modulators based on iron garnet films are found to offer distinct advantages such as a tunable bandwidth and dual mode operation (resonant and non-resonant), both of which are controlled via an externally applied static magnetic field. With all these benefits, iron garnet MO modulators may prove to be a viable alternative to contemporary methods of optical modulation.

1.1 Thesis Objectives

The goal of this thesis is to demonstrate high-speed MO modulation utilizing a bismuth substituted yttrium iron garnet film. To achieve this, a prototype MO modulator is constructed and characterized. This experimental work is complimented with a theoretical model, which is employed to predict the operation of the MO modulator and a novel MO beam deflector.

1.2 Thesis Organization

This thesis is comprised of five chapters and four appendices that detail the experimental and theoretical work performed. Chapter 2 introduces the underlying mechanisms of MO modulation and gives an overview of previous experiments.

In Chapter 3, a model is developed for light-wave propagation in MO materials that have a time-dependent magnetization. For this, a beam propagation method is combined with a formalism that describes the time evolution of the magnetization vector. This model is employed to study the operation of the MO modulator and is then used to predict the operation of a novel high-speed MO beam deflection device.

The discussion section of Chapter 4 describes the experimental aspects of MO modulation. In this Chapter, the fabrication of the MO modulator is presented, and the components used to characterize the device are described in detail. This is followed by a presentation of the experimental results, which illustrates two modes of operation: resonant and non-resonant. These two operational modes of the modulator are studied

and discussed, as is the bandwidth of the device. Finally, the modulation depth is measured.

Chapter 5 summarizes and concludes the work performed in this thesis and provides a list of possible improvements for the next generation MO modulator.

1.3 Reference

- [1] S. Geller and M. A. Gilleo, "Structure and ferrimagnetism of yttrium and rare-earth-iron garnets," *Acta. Cryst.*, vol. 10, pp.239, 1957.

Chapter 2

Background

The present chapter provides the background knowledge and principles required to describe the concept of magneto-optic (MO) modulation. The chapter begins with a discussion outlining several MO effects such as magnetic linear birefringence and magnetic circular birefringence. The latter, also referred to as the Faraday effect, is of particular interest as it is this effect that underlies the operation of the MO modulator. The discussion is followed by a brief review of rare earth iron garnets and their utilization in MO devices. Since iron garnets are ferromagnetic, a model governing the temporal evolution of the magnetization vector is presented. Finally, the phenomenon of light diffraction from periodically reversed magnetization structures is introduced.

Following the background discussion, a literature review is presented that highlights relevant work performed in the area of MO modulation and light deflection.

2.1 Magneto-Optics Effects and the Faraday Effect

MO effects occur when certain optical properties of materials are changed with the application of a magnetic field. Several effects fall into this category and they are classified according to the direction of propagation of the optical beam with respect to the applied magnetic field. For example, a linearly polarized light beam traveling inside an MO material along a direction perpendicular to the applied magnetic field will become elliptically polarized. This effect is known as magnetic linear birefringence. Here, the

index of refraction for a light beam that is polarized along the magnetic field is different from the refractive index for light that has its polarization orthogonal to the magnetic field. A similar effect also occurs for the absorption coefficients of the two linear polarization states, and is termed magnetic linear dichroism.

Analogous effects occur for circularly polarized light if the applied magnetic field is along the direction of propagation. These effects are known as magnetic circular birefringence and magnetic circular dichroism. Magnetic circular birefringence is more commonly known as the Faraday effect and is usually employed in MO modulation/switching devices, including those presented and studied in this work. The Faraday effect is described in detail in the following section.

2.1.1 The Faraday Effect

As mentioned previously, the most fundamental physical process underlying the MO modulation device presented in this work is the Faraday effect. When a linearly polarized light beam passes through an MO material that has been placed in a magnetic field, the plane of polarization of the light beam is rotated with respect to its original orientation, as depicted in figure 2.1a. This is due to the fact that a circular birefringence has been induced by the presence of the applied magnetic field. The Faraday effect can be described as follows [1]. Consider a linearly polarized electromagnetic wave propagating along the z -direction with its polarization along the y -direction. This electromagnetic wave can be represented by

$$\vec{E} = E_0 \cos(\omega t - \frac{2\pi n z}{\lambda_0}) \hat{y} \quad (2.1.1)$$

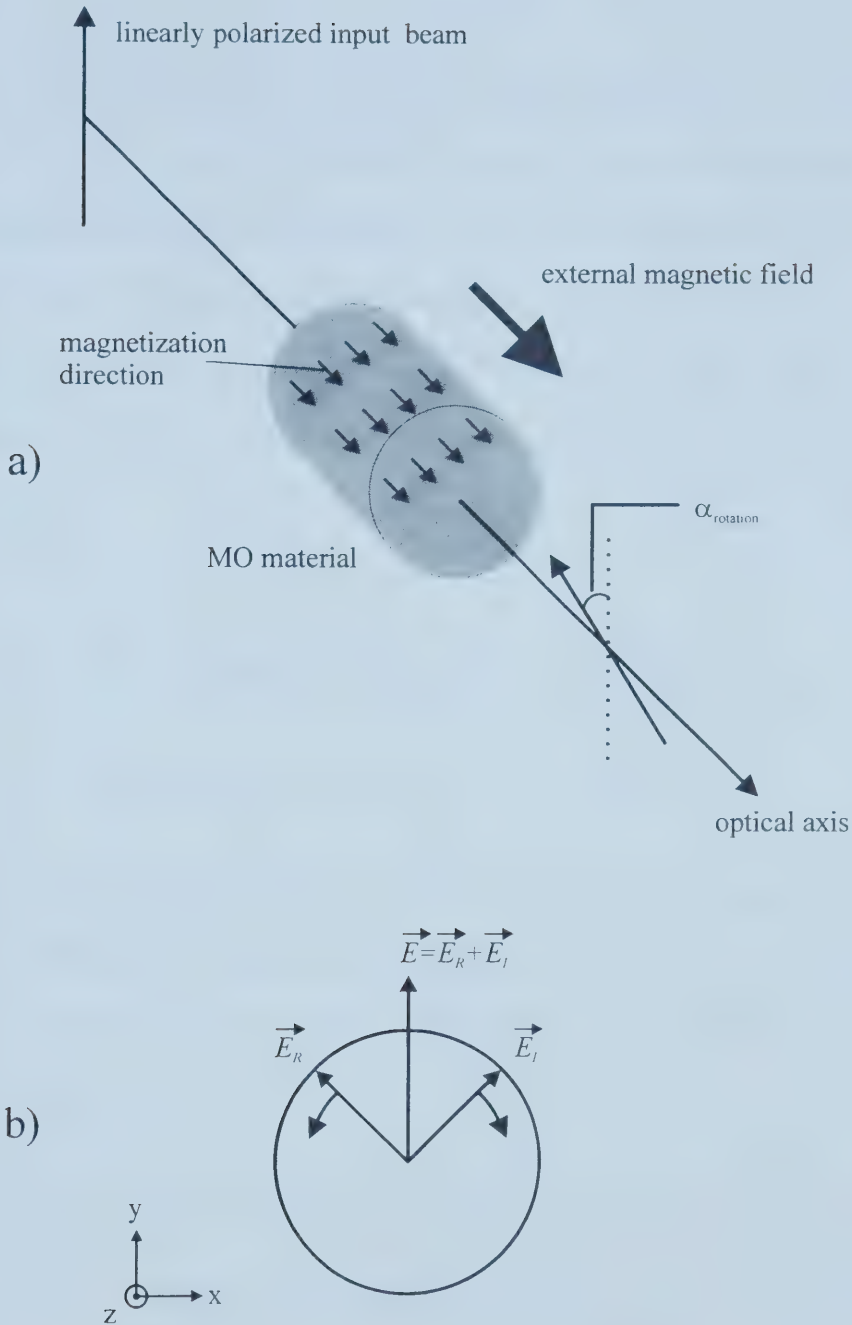


Figure 2.1. a) A light beam experiences a polarization rotation due to the Faraday effect when it passes through material having a net magnetization along the direction of propagation. b) The linear polarization of a wave traveling out of the page can be resolved into left and right circular polarizations.

where \vec{E} is the electric field vector, E_0 is the complex field amplitude, ω is the angular frequency, λ_0 is the vacuum wavelength of the light, n is the index of refraction of the material the light wave is traversing, and \hat{y} is a unit vector denoting the y -direction. As shown in figure 2.1b, the electric field vector of the electromagnetic wave given by equation 2.1.1 can be decomposed into left and right circularly polarized waves, according to

$$\vec{E} = \vec{E}_R + \vec{E}_L \quad (2.1.2)$$

where

$$\vec{E}_L = -\frac{E_0}{2} \sin(\omega t - \frac{2\pi n_L z}{\lambda_0}) \hat{x} + \frac{E_0}{2} \cos(\omega t - \frac{2\pi n_L z}{\lambda_0}) \hat{y} \quad (2.1.3)$$

$$\vec{E}_R = \frac{E_0}{2} \sin(\omega t - \frac{2\pi n_R z}{\lambda_0}) \hat{x} + \frac{E_0}{2} \cos(\omega t - \frac{2\pi n_R z}{\lambda_0}) \hat{y} \quad (2.1.4)$$

Here, n_R is the refractive index for a right circularly polarized wave and n_L is the refractive index for a left circularly-polarized wave. If the indices of refraction n_R and n_L are equal, equation 2.1.2 reduces to 2.1.1. Equation 2.1.2 can be reformulated in a more meaningful form using

$$\cos(\alpha) + \cos(\beta) = 2 \cos(\frac{\alpha}{2} + \frac{\beta}{2}) \cos(\frac{\alpha}{2} - \frac{\beta}{2}) \quad (2.1.5)$$

$$\sin(\alpha) - \sin(\beta) = 2 \cos(\frac{\alpha}{2} + \frac{\beta}{2}) \sin(\frac{\alpha}{2} - \frac{\beta}{2}) \quad (2.1.6)$$

to yield the following alternate representation:

$$\begin{aligned} \vec{E} = E_0 & \left(\cos\left(\omega t - \frac{\pi(n_L + n_R)z}{\lambda_0}\right) \sin\left(\frac{\pi(n_L - n_R)z}{\lambda_0}\right) \hat{x} \right. \\ & \left. + \cos\left(\omega t - \frac{\pi(n_L + n_R)z}{\lambda_0}\right) \cos\left(\frac{\pi(n_L - n_R)z}{\lambda_0}\right) \hat{y} \right) \end{aligned} \quad (2.1.7)$$

This equation reveals the mechanism of polarization rotation given a circular birefringence. In each of the terms of equation 2.1.7, the first function represents a propagating wave while the second function represents a harmonic modulation of the amplitudes as the wave propagates along the z -direction. As the wave travels through the MO material, the polarization vector of the wave is rotated from the y -direction and into the x -direction. It is possible that the polarization could be rotated 360° if either the optical-material interaction length or if the Faraday rotation is large enough. The angle of polarization rotation with respect to the initial polarization (which was along the y -axis) is given by

$$\phi = \tan^{-1} \left(\frac{\vec{E} \cdot \hat{x}}{\vec{E} \cdot \hat{y}} \right) = \frac{\pi(n_L - n_R)z}{\lambda_0} \quad (2.1.8)$$

For diamagnetic and paramagnetic materials, the amount of polarization rotation is directly proportional to the magnetic field and is given by [2]

$$\alpha_{rotation} = VBd \quad (2.1.9)$$

where $\alpha_{rotation}$ is the angle of rotation experienced by the plane of polarization, V is the Verdet constant of the sample, d is the interaction length, and B is the component of magnetic field along the direction of light propagation. This relationship between polarization rotation and magnetic field exists for diamagnetic and paramagnetic substances since these types of materials exhibit no ordering of their atomic magnetic dipoles (the atoms of diamagnetic materials have no net magnetic dipole moments).

In contrast, ferromagnetic substances do exhibit spin ordering, which can allow these materials to have a non-zero magnetization in the absence of an externally applied field. In addition, ferromagnetic materials exhibit a saturated magnetization state, in which all of the magnetic domains within the material are aligned with a sufficiently large magnetic field.

For ferromagnetic MO materials, equation 2.1.9 cannot be used since the amount of polarization rotation is fundamentally dictated by the degree of magnetization of the MO sample in question. Instead, the following equation can be used [3]:

$$\theta_F = \frac{M_z}{M_s} \theta_{spec} \quad (2.1.10)$$

where θ_F is the Faraday rotation, M_z is the component of the magnetization along the direction of propagation (which is taken to be the z -direction), M_s is the saturation magnetization, and θ_{spec} is the specific Faraday rotation of the sample, which is defined to be the value of the Faraday rotation at saturation magnetization (this value of the Faraday rotation is usually quoted for MO ferromagnetic materials).

A simplified relationship between the Faraday rotation and the applied magnetic field is shown in figure 2.2 [2], where B_{sat} is the magnetic field necessary to saturate the magnetization of the sample. For this figure, it is assumed the direction of the applied field is along the optical propagation direction. For magnetic fields between $-B_{sat}$ and B_{sat} , the magnetization follows the applied magnetic field linearly. Above B_{sat} or below $-B_{sat}$, the magnetization is the constant value of M_s or $-M_s$, depending on the direction of applied field. In actual ferromagnetic systems, samples would exhibit hysteresis owing to effects of magnetic domains [4].

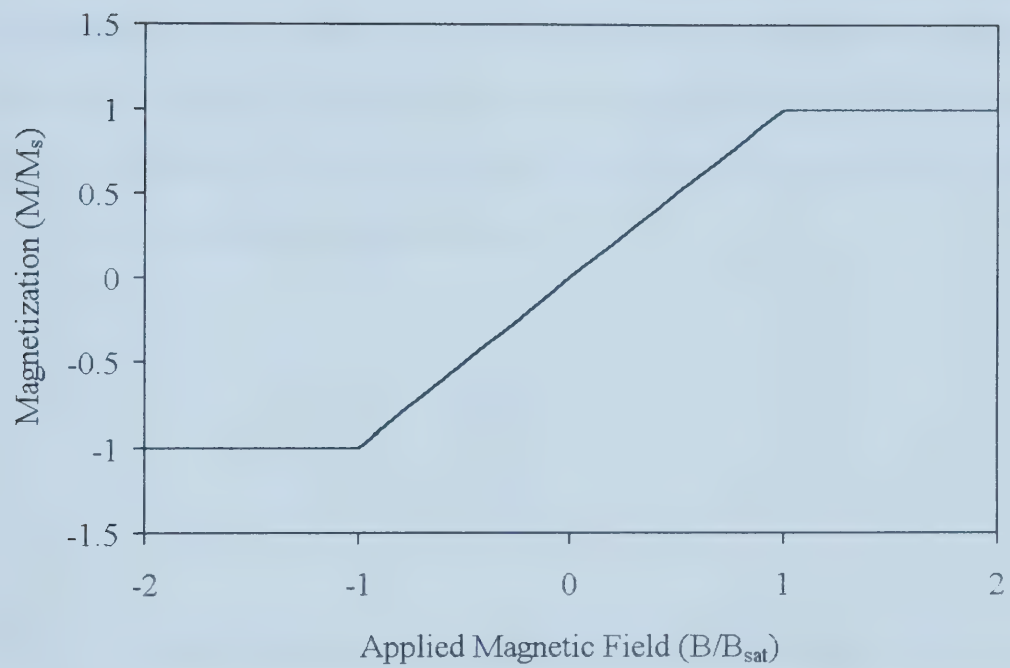


Figure 2.2. Ideal relationship between magnetization and applied magnetic field in a ferromagnetic material. After [2].

2.1.2 Origin of the Faraday Effect

Fundamentally, the Faraday effect arises from the precession of the electrons in the material through which the light-wave is propagating [5]. The situation is depicted in figure 2.3. The motion of the electron results from the application of an external static magnetic field and a perturbing magnetic field, the latter of which can be caused by an electromagnetic wave at optical frequency. This circular-like motion of the electron (which has a non-zero magnetic dipole moment) contributes non-zero off-diagonal elements to the magnetic susceptibility tensor. For an applied static magnetic field along the z -direction, these elements are of the form [5]

$$\begin{aligned}\mu_{xy} &= -iC \frac{\omega}{\omega_0^2 - \omega^2} \\ \mu_{yx} &= iC \frac{\omega}{\omega_0^2 - \omega^2}\end{aligned}\tag{2.1.11}$$

where C is a material dependent parameter, ω_0 is the precessional frequency, and ω is the frequency of the optical wave. Using these elements, the effective permeabilities for the left and right circular polarizations are derived to be [5]

$$\begin{aligned}\mu_{left} &= \mu_0 \left(1 - \frac{C}{\omega_0 + \omega} \right) \\ \mu_{right} &= \mu_0 \left(1 - \frac{C}{\omega_0 - \omega} \right)\end{aligned}\tag{2.1.12}$$

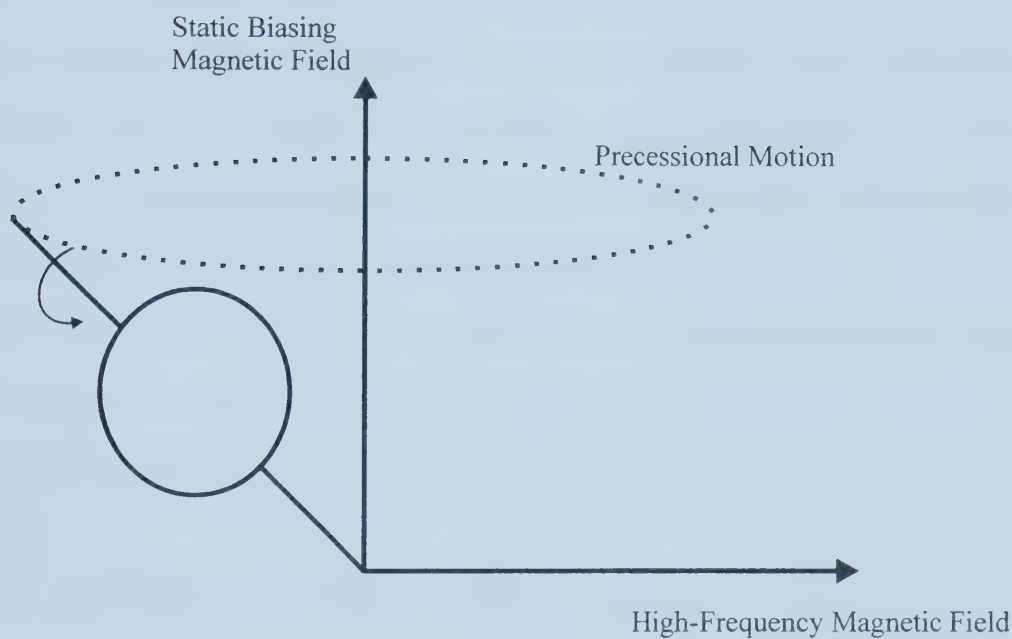


Figure 2.3. Precessional motion of an electron in the presence of a static magnetic field and a perturbing magnetic field. The motion results in magnetization components m_x and m_y . After [5].

From equation 2.1.12, it is observed that the two states of circular polarization have different values of permeabilities. This leads to circular birefringence, i.e. the Faraday effect. It should be noted that in the above calculations damping has been ignored. To include such effects, imaginary terms can be included in equation 2.1.12, which will limit the permeability magnitudes to finite values at resonance.

In ferromagnetic material, such as iron garnets discussed in the following section, the situation is more complicated. Here, strong interactions between neighboring magnetic dipoles in ferromagnetic substances gives rise to magnetic domains and internal fields. These strong interactions also create many optical resonances of varying strengths and frequencies, which leads to a complex dependence of the Faraday rotation on the optical wavelength. This interaction manifests itself as a splitting of the energy levels associated with the preferential absorption between left and right circularly polarized electromagnetic waves.

2.2 Thin Film Bismuth Substituted Yttrium Iron Garnet

Much effort has been devoted to the research and development of yttrium iron garnet (YIG). This material is attractive for MO device applications as it has a significant specific Faraday rotation and small absorption in the wavelength range between 1.2 μm and 5 μm [6]. The crystal lattice of YIG is depicted in figure 2.4 [7]. The lattice is a subclass of the more general category of garnet materials having a general formula: $\{\text{R}_3\}\{\text{A}_2\}(\text{D}_3)\text{O}_{12}$, where R, A, and D denote specific lattice sites and O denotes the element oxygen. The lattice consists of three main sites: dodecahedral, octahedral and

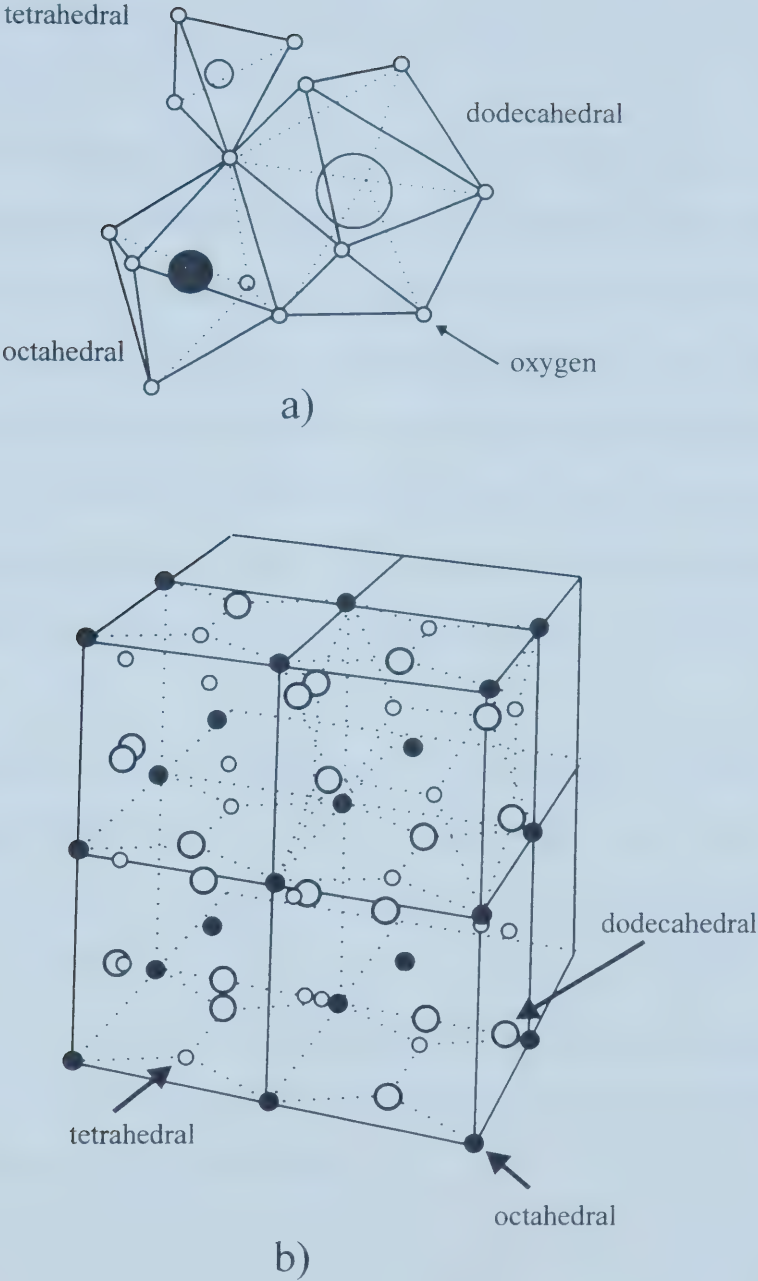


Figure 2.4. a) The various lattice sites for a garnet crystal. b) The crystal lattice structure of garnet. After [7].

tetrahedral sites. These sites are occupied by elements of type R, A and D, respectively. As shown in figure 2.4, YIG has $R=Y$, $A=Fe$, and $D=Fe$, and therefore its chemical composition is $Y_3Fe_5O_{12}$.

Interestingly, the MO properties of YIG can be altered substantially with the substitution of various elements composing the garnet. The enhancement of the Faraday rotation can be achieved by replacing a fraction of the yttrium atoms with bismuth atoms ($Bi_xY_{3-x}Fe_5O_{12}$ with $x \leq 0.5$, [2]). This preferential substitution results in an increase of the Faraday rotation by as much as a factor of 10 without appreciable increase of absorption [8]. YIG and Bi-YIG are typically grown as thin films by means of liquid phase epitaxy on (111)-oriented gadolinium gallium garnet (GGG). Often, the Bi-YIG is substituted with a variety of elements to ensure that the lattice spacing of the film and substrate are matched.

An important parameter for Bi-YIG films, known as the figure of merit, is defined to be the ratio of the specific Faraday rotation to the absorption (usually quoted in units of degrees or degrees per dB). For example, the figures of merit for pure YIG and $Y_{2.3}Bi_{0.7}Fe_5O_{12}$ (at a wavelength of 633 nm) are 0.96° and 12.5° , respectively [2]. Even though the figure of merit is higher for Bi-YIG, absorption is still an important parameter to consider. In order to fabricate MO devices based on Bi-YIG, the optical interaction length must be on the order of one absorption length.

2.3 Time Evolution of the Magnetization in Ferromagnetic Materials

The principle of MO modulation involves the perturbation of material magnetization using externally applied static and transient magnetic fields. The transient field is used to switch the magnetization in the Bi-YIG film along the direction of light propagation. The static field is applied in a direction perpendicular to the transient magnetic field to return the magnetization to a well-defined state before the next transient field is applied and to ensure a homogeneous magnetization in the sample.

In order to characterize the efficiency and switching speed of the MO modulator, a model describing the response of the magnetization to static and time-varying magnetic fields is required. Since the MO modulator investigated in this work is based on a ferromagnetic Bi-YIG film, the response of the magnetization to modulating magnetic fields is complex, as it is a spin system under the application of an external torque [9]. The formalism of Landau-Lifshitz (LL) [9]

$$\frac{\partial \mathbf{M}}{\partial t} = \frac{\gamma}{\mu_0} (\mathbf{M} \times \mathbf{b}) - \frac{\eta}{M^2} \mathbf{M} \times (\mathbf{M} \times \mathbf{b}) \quad (2.3.1)$$

is adopted to describe the uniform motion of the magnetization vector, \mathbf{M} . Here, $\gamma = 2\pi(28 \text{ GHz/T})$ is the gyromagnetic ratio, μ_0 is the permeability of free space, and η is the damping rate due to spin relaxation. The magnetic field, \mathbf{b} , in the above equation is the sum of the static, b_y , and time-varying, $b_z(t)$, magnetic fields. Damping times are typically $\sim 100 \text{ ns}$ [10], and as such, are ignored in all calculations since they are much longer than any modulation interval ($\sim 1 \text{ ns}$) considered. If longer pulse widths are modeled ($\sim 100 \text{ ns}$), the effects of damping should be included. Equation 2.3.1 is non-linear and closed

form solutions are unattainable; therefore, a numerical fourth order Runge-Kutta method [11] is used to obtain a solution. The method was encoded in Visual C++ (Appendix A).

Figure 2.5 illustrates a typical solution to the LL equation for $(M_x(t), M_y(t), M_z(t))$ as a function of time. The parametric plot shows the evolution of the magnetization (i.e the tip of the magnetization vector is traced) for times ranging from -2.5 to 2.5 ns. This motion of the magnetization is in response to a transient magnetic field of Gaussian form, the peak of which is centered in 0 ns. The amplitude of this transient pulse is 20 mT and the full-width at half-maximum (FWHM) is 1 ns. The static field is applied along the y -direction, and has a value of $b_y=27.5$ mT, which initially saturates the magnetization along the y -direction. Precessional behavior can clearly be observed in the figure as the tip of the magnetization vector orbits the axis of the biasing magnetic field.

Of interest is the temporal response of the magnetization component along the direction of propagation, $M_z(t)$, as it is this component which determines the amount of Faraday rotation. Figure 2.6 illustrates the temporal progression of $M_z(t)$ normalized to the magnitude of the magnetization vector for various biasing magnetic fields. For biasing fields below 70 mT, the responses show distinct oscillatory behavior. These oscillations are due to the uniform ferromagnetic precession of the magnetization, whose frequency is given by [12]

$$\nu = \frac{\gamma}{2\pi} b_y, \quad (2.3.2)$$

where ν is the ferromagnetic resonance (FMR) frequency for the uniform precessional mode. Although the LL model does not consider size effects, shape effects,

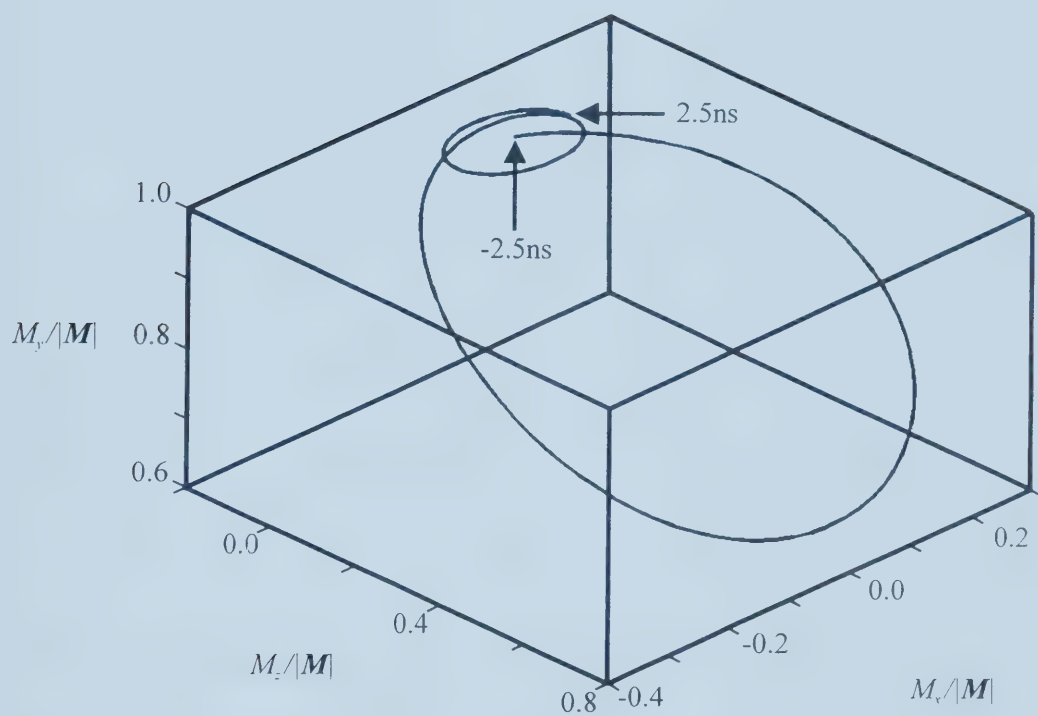


Figure 2.5. A parametric plot of the temporal evolution of the magnetization for times ranging from -2.5 to 2.5 ns in response to a 20 mT, 1 ns FWHM Gaussian magnetic field pulse and DC magnetic field of 27.5 mT.

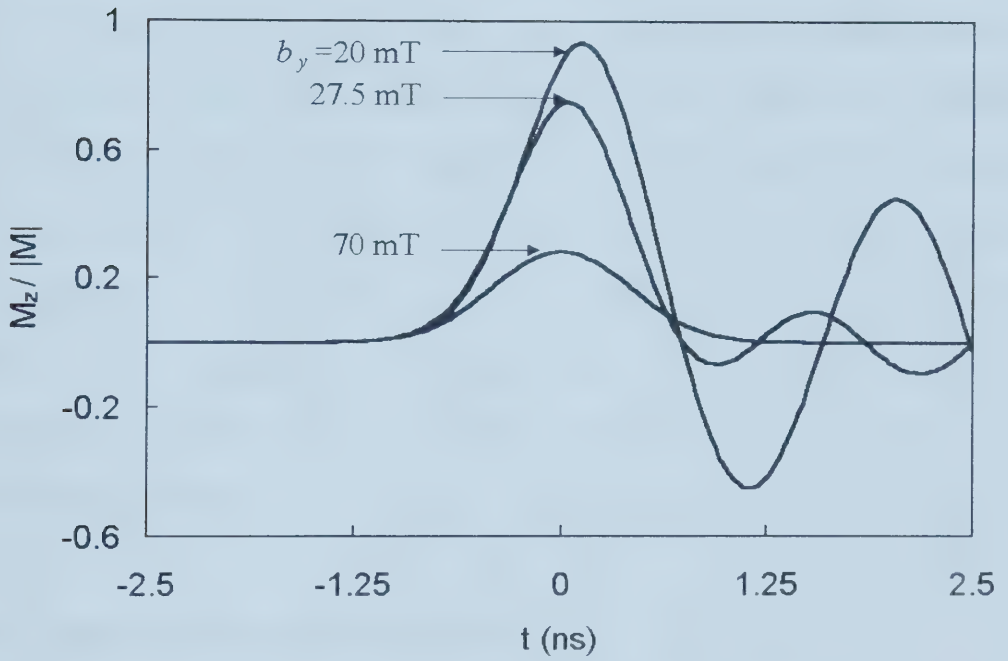


Figure 2.6. The normalized z-component of the magnetization plotted in figure 2.5. Various biasing fields are used to illustrate the ferromagnetic precession of the magnetization.

or reduced dimensionality, this equation for the FMR can be derived for thin film samples where the static magnetic field, b_y , is in the plane of the film [12]:

$$\nu^2 = |\gamma/2\pi|^2 \{b_y(b_y + \mu_0 M_s)\}. \quad (2.3.3)$$

The oscillations due to FMR can be damped by applying a larger static magnetic field as shown in figure 2.6. For biasing magnetic fields above 70 mT, the temporal response follows the input magnetic field transient, however, the overall amplitude of the response has decreased. The reduction in the amplitude is attributed to the fact that a stronger transient magnetic field is required to tip the magnetization away from the direction of the static magnetic field. Clearly, the bias magnetic field is an important parameter in determining the bandwidth, the temporal signal shape, and the MO response. Therefore, an optimum field must be chosen to maximize signal amplitude while maintaining the appropriate signal shape.

2.4 Diffraction from Magnetic Gratings

Diffraction gratings, in general, produce a periodic spatial modulation of incident electromagnetic wave amplitudes and/or phase fronts. Various portions of the incoming wave experience modulated phase retardations corresponding to the regions of propagation. In the far field, interference between the emerging wave fronts results in the formation of a diffraction pattern.

A similar effect takes place in an MO phase gratings, in which the magnetization (and therefore, the Faraday rotation) is periodically reversed. Consider the case as

depicted in figure 2.7. Here, an input beam of transverse electric (TE) polarization is incident upon an MO film which has its magnetization periodically reversed. Different portions of the input beam traveling through different regions of the MO material will experience rotations ($\pm\theta_F d$, where d is the thickness of the film) of their planes of polarization that depend on the sign of M_z . As a result, the polarization of the output electric field vector varies with a spatial frequency corresponding to the periodicity of M_z . This results in an effective modulation of the phase front. In the distant far field, the waves can be reconstructed using Huygen's principle to yield a diffraction pattern and the diffraction orders. These orders obey the standard diffraction grating equation:

$$m\lambda = 2\delta \sin(\alpha_m) \quad (2.4.1)$$

where m is the diffraction order, λ is the wavelength, 2δ is the magnetization modulation period (alternatively, δ is the spacing between adjacent domains), and α_m is the diffraction angle of order m . A unique aspect of this MO grating is that its diffraction orders are polarized according to their odd/even parity. To illustrate this effect, consider the ray analysis method presented in figure 2.8 [6] with the input beam being TE polarized, that is, the electric field vector of every ray of the input beam is oriented out of the page. When the light beam passes through the film, the electric field vectors of each ray are slightly rotated, and the emerging rays have electric field components that are both perpendicular (E_{perp}) and parallel (E_{par}) to the initial electric field of the input beam. In the lowest order mode ($m=0$), the adjacent rays have their E_{par} components aligned in the same direction, and therefore, these components add. However, the E_{perp} components

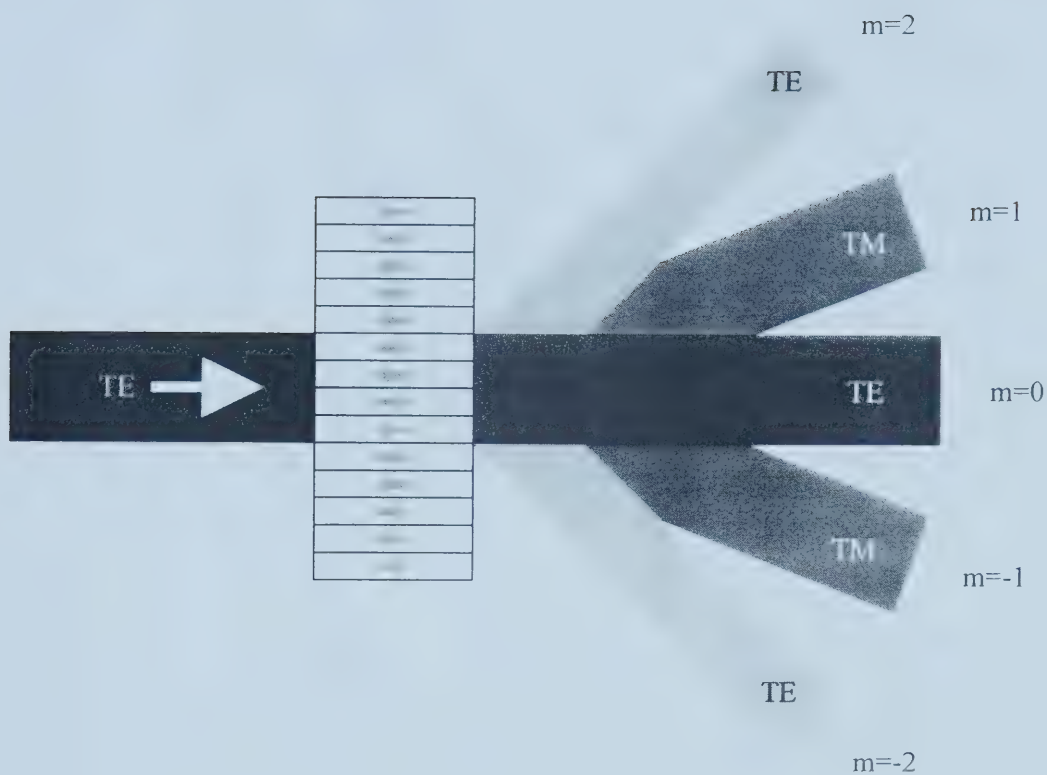


Figure 2.7. Schematic diagram of an MO phase grating. Even modes have polarization that is the same as that of the input beam while the odd modes have polarization that is orthogonal to that of the input beam.

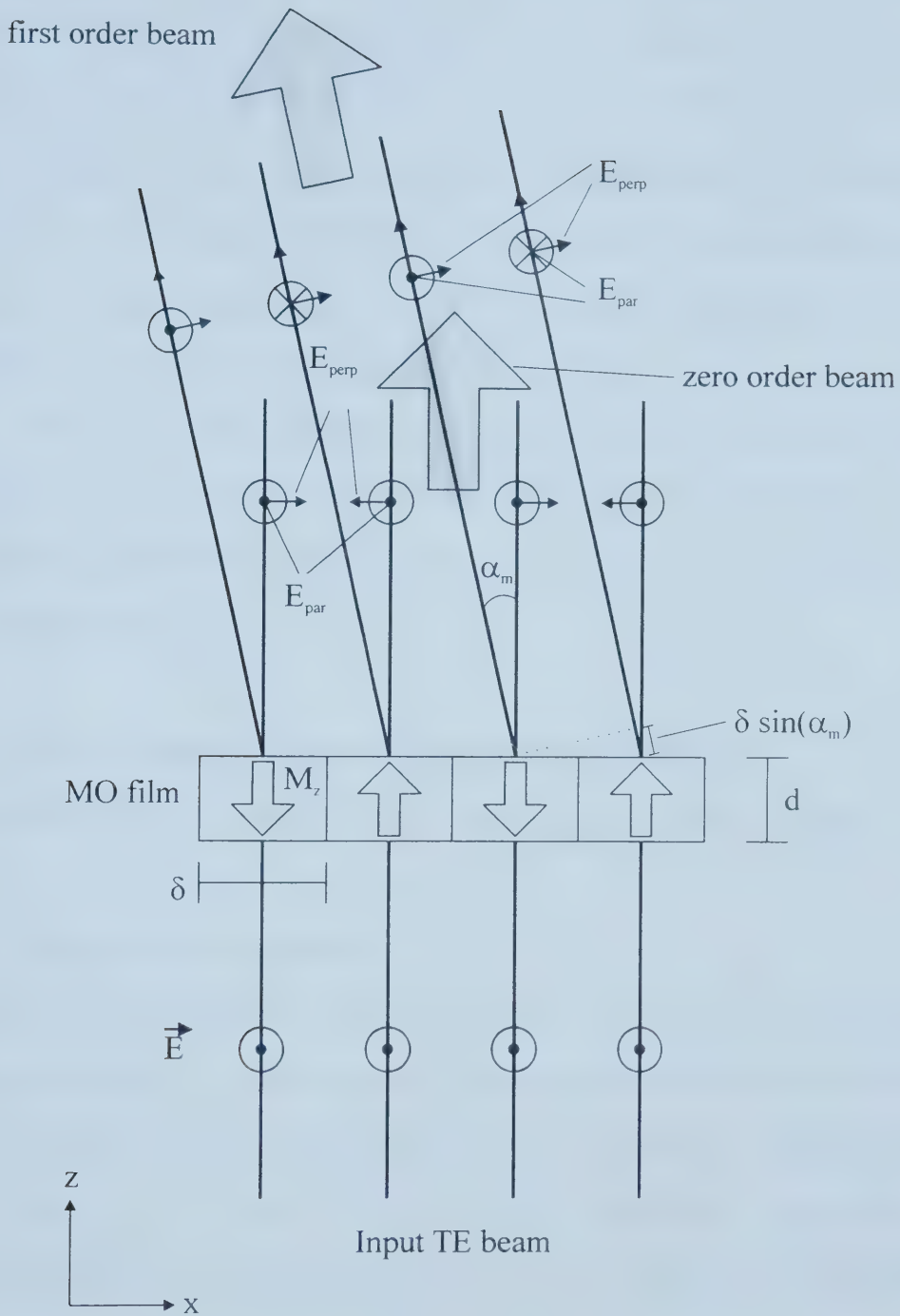


Figure 2.8. Ray analysis illustration of diffraction from an MO phase grating [6].

of adjacent rays cancel each other since they are of equal magnitude and opposite direction. Therefore, the lowest diffraction order ($m=0$) maintains the original TE polarization. Now consider the first order ($m= \pm 1$) beam, where adjacent rays have a phase difference of π . Here, the E_{par} components cancel, while the E_{perp} components add, resulting in a TM polarized diffracted mode. This pattern of alternating polarization continues for higher orders, where even diffraction orders have TE polarization and odd diffraction orders have transverse magnetic (TM) polarization.

Based on this effect, an MO deflector can be constructed where the magnetization orientation can be actively switched by externally applied magnetic fields. Several experiments demonstrate the principle of MO beam deflection and are discussed in the following literature review.

2.5 Review of Magneto-Optic Modulation and Beam Deflection

This section reviews previous work relevant to MO modulation and beam deflection.

2.5.1 Magneto-Optic Modulation

It was recognized early that devices based on the MO effect could be important for telecommunications. In 1966, LeCraw [3,13] developed a modulation device employing the Faraday effect in rod of gallium substituted YIG. The geometry is shown in figure 2.9, where a coil was used to apply a transient magnetic field that switch the magnetization of the MO rod. This caused a polarization rotation of a $1.52 \mu\text{m}$ optical beam traveling along the axis of the rod and a subsequent intensity modulation after a polarization analyzer. The bandwidth of the system was 200 MHz.

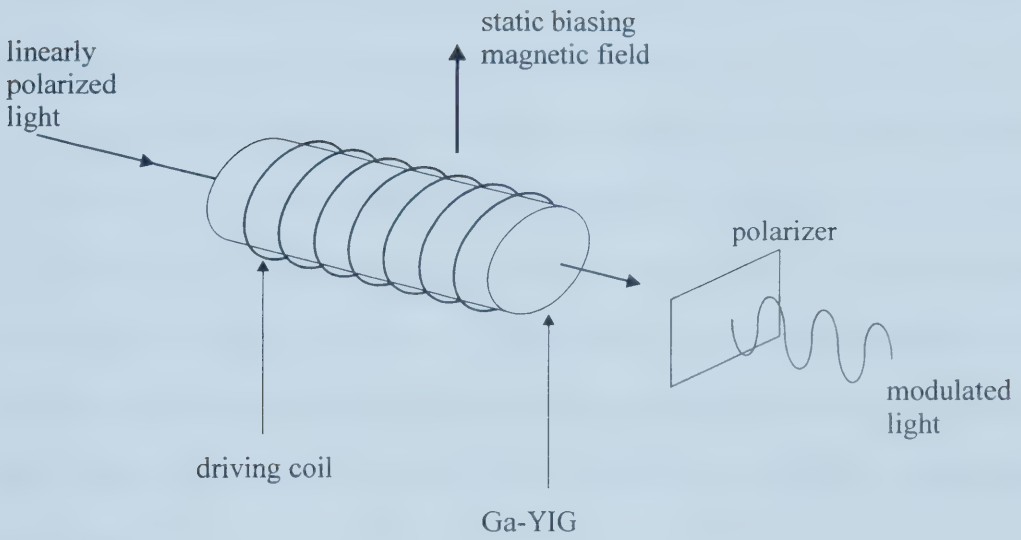


Figure 2.9. Geometry of the MO modulator constructed by Le Craw. After [3,13].

MO modulation in a thin film iron garnet waveguide was first demonstrated by Tien et al. [14]. This was achieved using a $\text{Y}_3\text{Ga}_{1.1}\text{Sc}_{0.4}\text{Fe}_{3.5}\text{O}_{12}$ film in the experimental arrangement shown in figure 2.10. Prisms were used to couple TM polarized light, at a wavelength of $1.152\text{ }\mu\text{m}$, into and out of the MO film waveguide. A serpentine transmission line was employed to compensate for birefringence and effectively switch the magnetization of the film and cause a modulation in the output TE and TM beams. With this setup, a maximum modulation frequency of 80 MHz was achieved with a mode conversion efficiency of approximately 52%. This experiment demonstrated the feasibility of high-speed devices based on iron garnet films.

More recent experiments by Elezzabi and Freeman [10] revealed the ultra-fast capabilities of iron garnet materials. The experimental arrangement is shown in figure 2.11, where a $(\text{Y}_{0.6}\text{Bi}_{0.4}\text{LuPr})_3(\text{FeGa})_5\text{O}_{12}$ film was used to detect picosecond current pulses generated by a photoconductive switch. Using a pump-probe arrangement, the current transients were measured at the center of a gold micro-coil using the Faraday effect in the Bi-YIG film. The bandwidth of the sampling system had an upper limit of 82.3 GHz.

In similar time-resolved experiments performed by Jones and Elezzabi [15], a Bi-YIG film was employed as a modulator to impart electrical information from a transmission line onto an optical carrier. Current transients in the transmission line were used to modulate the magnetization of the Bi-YIG in a region where an optical beam was traversing. As a result of the Faraday effect, the polarization of the beam was modulated. The maximum bandwidth of the modulation system was 11.7 GHz.

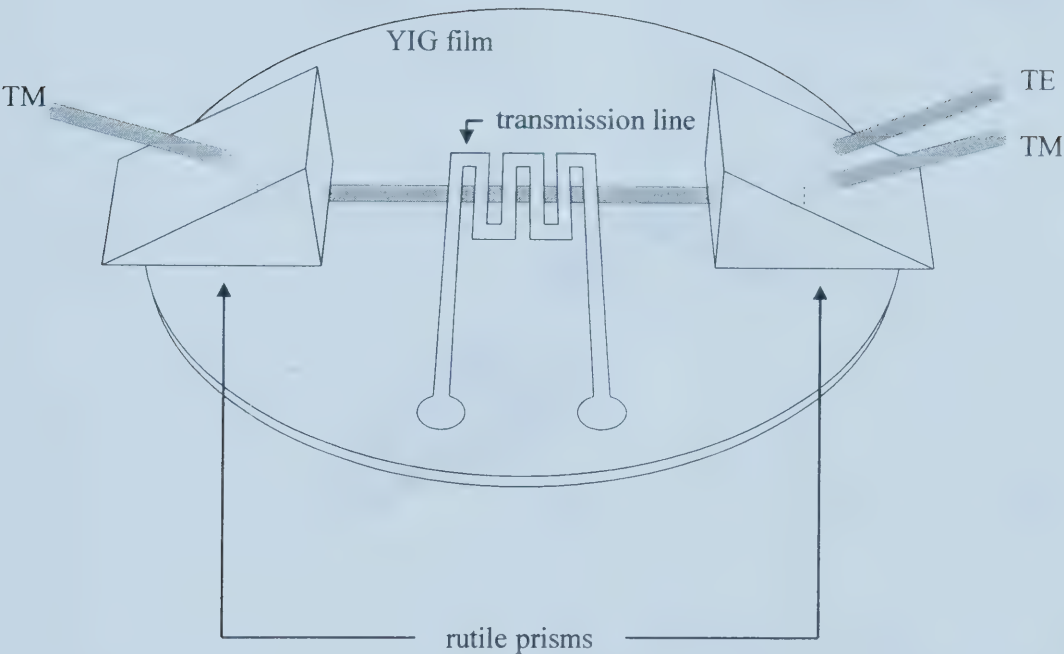


Figure 2.10. Experimental set-up used by Tien et al. [14], employing a Bi-YIG film as a waveguide MO modulator.

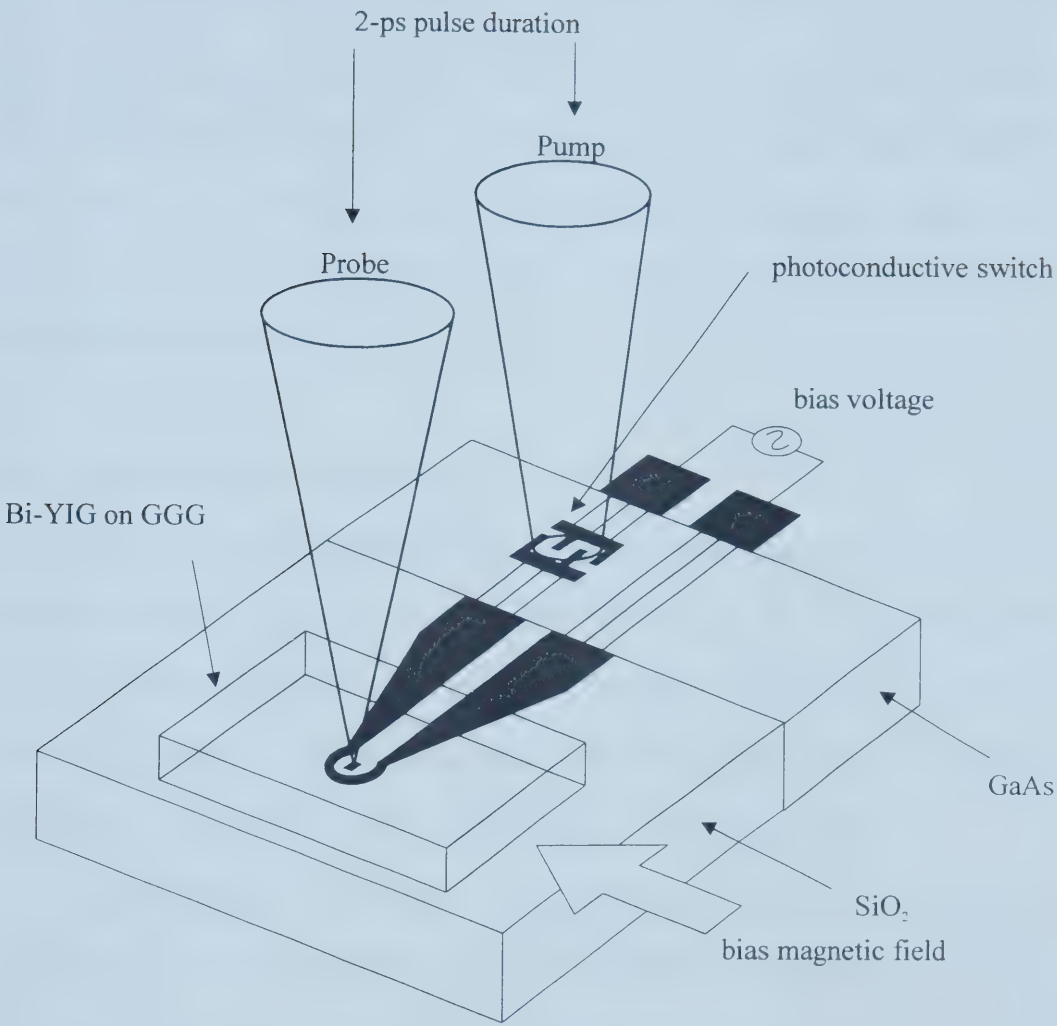


Figure 2.11. Pump-probe arrangement used by Elezzabi and Freeman [10].

Additional experiments by Prabhakar and Stancil [16] showed the high-speed response times of a bismuth substituted lutetium iron garnet film as depicted in figure 2.12. A microstrip transducer was placed in contact with the MO film, and a TM optical beam of wavelength $1.3\text{ }\mu\text{m}$ was edge-coupled into the thin film waveguide. Magnetic field transients from the microstrip transducer modulated the magnetization of the MO film, which in turn, modulated the polarization of the beam that had been coupled to the waveguide. Using this setup, the bandwidth of the device was measured to be 3 GHz centered around 5.75 GHz.

2.5.2 Magneto-Optic Beam Deflection

MO beam deflection utilizing straight magnetic domains of alternating magnetization (as illustrated in figure 2.7) was first demonstrated Johansen et al. [17]. Using an epitaxially grown $25\text{ }\mu\text{m}$ thick YIG film and by varying an in-plane magnetic field (i.e. parallel to the magnetic film), the magnetic domain stripe widths were varied from $30\text{ }\mu\text{m}$ to $3\text{ }\mu\text{m}$. A maximum deflection angle of 5° was achieved for a wavelength of 560 nm.

Similar deflection experiments were performed by Numata et al. [18] in $(\text{BiNdYb})_3\text{Fe}_5\text{O}_{12}$ and in YIG-coated $(\text{YSmLuCa})_3(\text{FeGe})_5\text{O}_{12}$ films. In the absence of the in-plane magnetic field and for a stripe domain width of $0.65\text{ }\mu\text{m}$, a significantly large beam deflection angle of 30° at a wavelength of 632.8 nm was demonstrated using the $(\text{BiNdYb})_3\text{Fe}_5\text{O}_{12}$ film. However, the deflection efficiency (defined as the ratio of the deflected intensity to the total transmitted intensity) was $\sim 1\%$.

Realizing the strong dependence of the deflection efficiency on both the amount of the Faraday rotation and on the interaction length in the MO film, Hepner et al. [19]

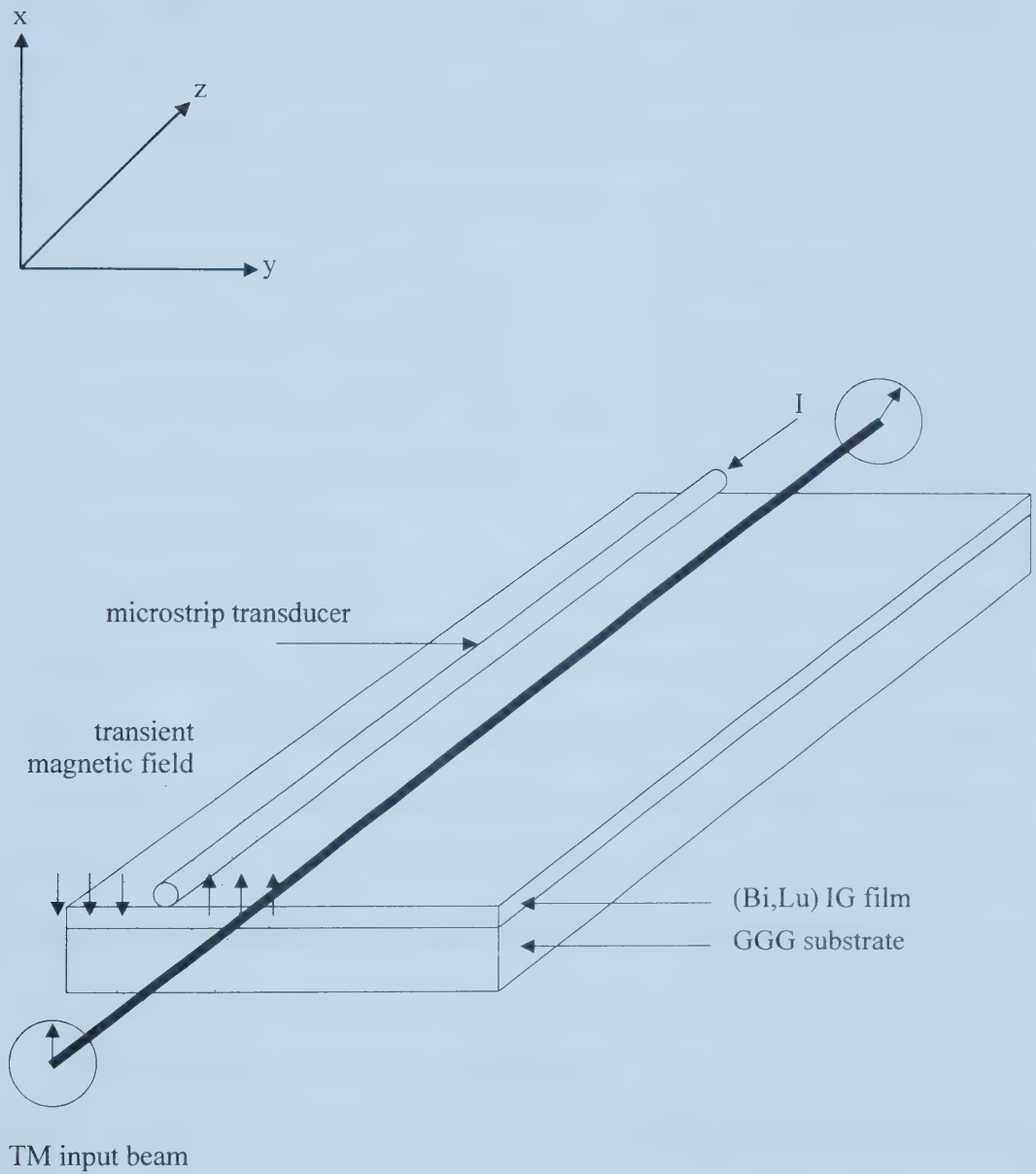


Figure 2.12. Experimental arrangement employed by Prabhakar and Stancil [16].

employed a guided wave configuration in their deflector design. By prism coupling 1150 nm laser radiation into a 4.4 μm thick $\text{Gd}_{0.45}\text{Y}_{2.55}\text{Fe}_{4.2}\text{Ga}_{0.8}\text{O}_{12}$ film, they managed to obtain a diffraction efficiency of 15% in an interaction length of 1 cm.

The possibility of dynamic light modulation and deflection by oscillating domain lattices in periodic stripe domains in a Bi-YIG film was first realized by Sauter et al. [20]. Fast switching ($\sim 1 \mu\text{s}$) of 630 nm beams into a multi-port fiber network was demonstrated using only in-plane magnetic fields. In order to increase the switching speed, Blanke et al. [21] exploited the high-frequency ferromagnetic resonance response of a variety of bismuth substituted garnet films ($\text{Y}_{2.17}\text{Bi}_{0.8}\text{Pb}_{0.07}\text{Fe}_{4.07}\text{Al}_{0.9}\text{Pt}_{0.02}\text{O}_{12}$, $\text{Tm}_{2.54}\text{Bi}_{0.46}\text{Fe}_{3.87}\text{Ga}_{1.01}\text{Al}_{0.5}\text{Pt}_{0.07}\text{O}_{12}$, $\text{Y}_{2.13}\text{Bi}_{0.8}\text{Pb}_{0.07}\text{Fe}_{4.83}\text{Pt}_{0.3}\text{O}_{12}$, $\text{Y}_{1.65}\text{Bi}_{1.29}\text{Pb}_{0.06}\text{Fe}_{4.98}\text{Pt}_{0.02}\text{O}_{12}$). A 2 GHz resonance and tunable single frequency modulation of a 630 nm laser beam were demonstrated. The high frequency deflection modulation was achieved through the application of an RF magnetic field perpendicular to both the film and to an in-plane applied magnetic field. With this configuration, the relative stripe domain width is modulated at a domain lattice resonance frequency and this modulation is mapped into a regular angular deflection of the optical beam.

2.5.3 Modeling of Passive Magneto-Optic Devices

To model passive MO devices, Erdmann and Hertel [22] have derived a two-dimensional finite difference beam propagation method (BPM). Starting with Maxwell's equations and the constitutive equations for a material having a non-zero Faraday rotation, beam propagation operators are derived. This model is then applied to a variety of non-reciprocal devices employing magnetic linear birefringence and the Faraday effect. These

devices include a Mach-Zehnder interferometer, a directional coupler, and a mode converter.

2.6 References

- [1] The Faraday Effect [Online]. Available:
http://web.mit.edu/afs/athena/course/8/8.13/JLExperiments/JLExp_08.pdf
- [2] M. N Deeter, G. W. Day, and A. H. Rose, "Magneto optic Materials," *CRC Handbook of Laser Science and Technology, Supplement 2*, pp. 367-402, CRC Press, Boca Raton, 1995.
- [3] G. B. Scott and D. E. Lacklison, "Magneto optic Properties and Applications of Bismuth Substituted Iron Garnets," *IEEE Trans. Magn.*, vol. MAG-12, pp. 292-309, 1976.
- [4] R. A. McCurrie, *Ferromagnetic Materials: Structure and Properties*. New York: Academic Press, 1994, pp. 1-21.
- [5] H. W. Katz (editor), *Solid State Magnetic and Dielectric Devices*. New York: John Wiley & Sons Inc., 1994, pp. 268-272.
- [6] P. Paroli, "Magneto-Optical Devices Based on Garnet Films," *Thin Solid Films*, vol. 114, pp. 187-219, 1984.
- [7] S. Geller, "Crystal and Static Magnetic Properties of Garnets," in *Physics of Magnetic Garnets*, A. Paoletti, Ed. New York: North-Holland Publishing, 1978, pp.1-6.

- [8] H. Takeuchi, S. Ito, I. Mikami, and S. Taniguchi, "Faraday rotation and optical absorption of a single crystal of bismuth-substituted gadolinium iron garnet," *J. Appl. Phys.*, vol. 44, pp. 4789-4790, 1973.
- [9] R. F. Soohoo, *Microwave Magnetics*. New York, NY: Harper and Row, 1985, pp. 116-120.
- [10] A.Y. Elezzabi and M. R. Freeman, "Ultrafast magneto-optic sampling of picosecond current pulses," *Appl. Phys. Lett.*, vol. 68, pp. 3546-3548, 1996.
- [11] S. C. Chappra and R. P. Canale, *Numerical Methods for Engineers*. New York: McGraw-Hill, pp. 603-604, 1988.
- [12] C. Kittel, *Introduction to Solid State Physics*, 7th Ed. New York: Wiley, 1996, pp. 487-506.
- [13] R. C. LeCraw, "Broadband magneto-optic garnet modulator," U.S. Patent 3,495,189, April 19, 1966.
- [14] P. K. Tien, R.J. Martin, R. Wolfe, R.C. Le Crow, and S.L. Blank, "Switching and modulation of light in magneto-optic waveguides of garnet films," *Appl. Phys. Lett.*, vol. 21, pp.394-396, 1972.
- [15] G. Jones and A. Y. Elezzabi, "Ultrafast broadband tunable-bandwidth magneto-optic modulator," in *Proc. SPIE*, 1999, pp. 145-152.
- [16] A. Prabhakar and D. D. Stancil, "Wideband optical modulation via the magneto-optic interaction in a bismuth-lutetium-iron garnet film," *Appl. Phys. Lett.*, vol. 71, pp.151-153, 1997.

- [17] T. R. Johansen, D. I. Norman, and E. J. Torok, "Variation of Stripe-Domain Spacing in a Faraday Effect Light-Deflector," *J. Appl. Phys.*, vol. 42, pp. 1715-1716, 1971.
- [18] T. Numata, Y. Ohbuchi, and Y. Sakurai, "Stripe Domain Control in Garnet Films," *IEEE Trans. Magn.*, vol. MAG-16, pp.1197-1199, 1980.
- [19] G. Hepner, J. P. Castéra, and B. Désormière, "Magnetic stripe domain deflector in integrated optics," *Appl. Opt.*, vol. 15, pp.1683-1684, 1976.
- [20] G. F. Sauter, R. W. Honebrink, and J. A. Krawczak, "Alterable grating fiber-optic switch," *Appl. Opt.*, vol. 20, pp.3566-3572, 1981.
- [21] K. Blanke, B. Lührmann, U. Wallenhorst, H. Dötsch, and W. Tolksdorf, "High-Frequency Modulation and Deflection of Light by Oscillating Domain Lattices," *Phys. Stat. Sol. A.*, vol. 124, pp.359-369, 1991.
- [22] A. Erdmann and P. Hertel, "Beam-Propagation in Magneto optic Waveguides," *IEEE J. Quantum Electron.*, vol. 31, pp. 1510-1516, 1995.

Chapter 3

Beam Propagation Method and Results

In this section, a two-dimensional beam propagation method (BPM) is presented and is combined with the Landau-Lifshitz (LL) equation to model MO devices. This model, which will be referred to as the BPM-LL, is used to characterize the MO modulator and a novel high-speed MO beam deflector. This theoretical framework, which has been published previously [1,2], is not limited to the two devices mentioned above, as it can serve as an initial test for other potential MO devices.

3.1 Beam Propagation in Magneto-Optic Materials

A crucial first step in the design of a practical device is the formulation of an accurate theoretical model. For high-speed MO devices a practical model must incorporate magnetization dynamics, which ultimately governs the speed of the device. In addition, since the MO modulator proposed and tested in this work is comprised of a thin film waveguide, it is important to consider light-wave propagation effects (such as TE/TM mode conversion, birefringence, etc.). Therefore, it is necessary to combine two models in order to accurately predict the behavior of high-speed MO devices. The first part of the model is the LL formalism, in which the motion of the magnetization is predicted. The second part of the model is a time-independent BPM for MO structures (derived by Erdmann and Hertel [3] for the modeling of passive MO devices) that describes spatial effects due to propagating light waves.

To my knowledge, this BPM-LL is the first model to incorporate magnetization dynamics with light-wave effects in MO materials. This combination is an important step for future modeling of high-speed MO devices.

3.1.1 Derivation of the Beam Propagation Operators

To accurately predict the behavior of MO devices, one must consider light-wave propagation in a material having a time-dependent Faraday rotation, $\theta_F(t)$. The propagation of the light waves through a material having a non-zero Faraday rotation can be modeled strictly in terms of the electric field polarization of the electromagnetic wave. In such a case the material is taken to be non-magnetic with dielectric tensor given by [3]:

$$\hat{\epsilon}(t) = \begin{pmatrix} \epsilon_x & i\xi(t) & 0 \\ -i\xi(t) & \epsilon_y & 0 \\ 0 & 0 & \epsilon_z \end{pmatrix}, \quad (3.1.1)$$

where ϵ_x , ϵ_y , ϵ_z are the static dielectric constants in the x , y , z directions, respectively, and

$$\xi(t) = \frac{\lambda_0 \sqrt{\epsilon_z} \theta_F(t)}{\pi}. \quad (3.1.2)$$

The time variation of the Faraday rotation can be calculated from the degree of magnetization along the light propagation direction, $M_z(t)$, which in turn is calculated from the LL model presented in Chapter 2 and the following equation:

$$\theta_F(t) = \frac{M_z(t)}{M_s} \theta_{spec} \quad (3.1.3)$$

where: θ_F is the Faraday rotation, M_s is the saturation magnetization, and θ_{spec} is the specific Faraday rotation of the sample (i.e. the value of the Faraday rotation at saturation). The LL equation (2.3.1) calculates the fraction of $M_z(t)/M_s$, which is inserted into equation 3.1.1 to

determine the Faraday rotation. This value of the Faraday rotation is then used in equations 3.1.1 and 3.1.2 to determine the dielectric tensor at any instant in time.

Using equations 3.1.1 and 3.1.2, along with Maxwell's equations, the vector wave equations

$$\nabla^2 \vec{E} - \nabla(\nabla \cdot \vec{E}) + \omega^2 \mu_0 \epsilon_0 \hat{\epsilon}(t) \vec{E} = 0 \quad (3.1.4)$$

and,

$$-\nabla \times (\hat{\epsilon}^{-1}(t) \nabla \times \vec{H}) + \omega^2 \mu_0 \epsilon_0 \vec{H} = 0 \quad (3.1.5)$$

are derived assuming a time-varying harmonic field of the form $\exp(i\omega t)$. Since changes in the Faraday rotation occur on a time scale much longer than a single cycle of the propagating optical wave, the physical process can be treated in a quasi-static regime where time-derivatives of the dielectric tensor are ignored.

To simplify the calculations, a two dimensional approach is used where the structure is assumed to be infinite in the y -direction. In this situation, the polarization of an electromagnetic wave is a superposition of the non-zero TE field components (H_x, E_y, H_z) and the non-zero TM field components (E_x, H_y, E_z). For example, figure 3.1 shows the TE and TM polarizations for two different scenarios. One case is free space propagation at an arbitrary angle with respect to the z -direction and the other is propagation in a slab waveguide. In either case, the TE waves have their electric field vectors perpendicular to the x and z directions (i.e. $E_x=E_z=0$), while the TM waves have their magnetic field perpendicular to the x and z directions (i.e. $H_x=H_z=0$). Thus, for the BPM presented below, a semi-vector representation is chosen where E_y represents the TE mode and H_y represents the TM mode. With this in mind, beam propagation operators are derived from equations 3.1.4 and 3.1.5 as follows. Using the y -component of equation 3.1.4,

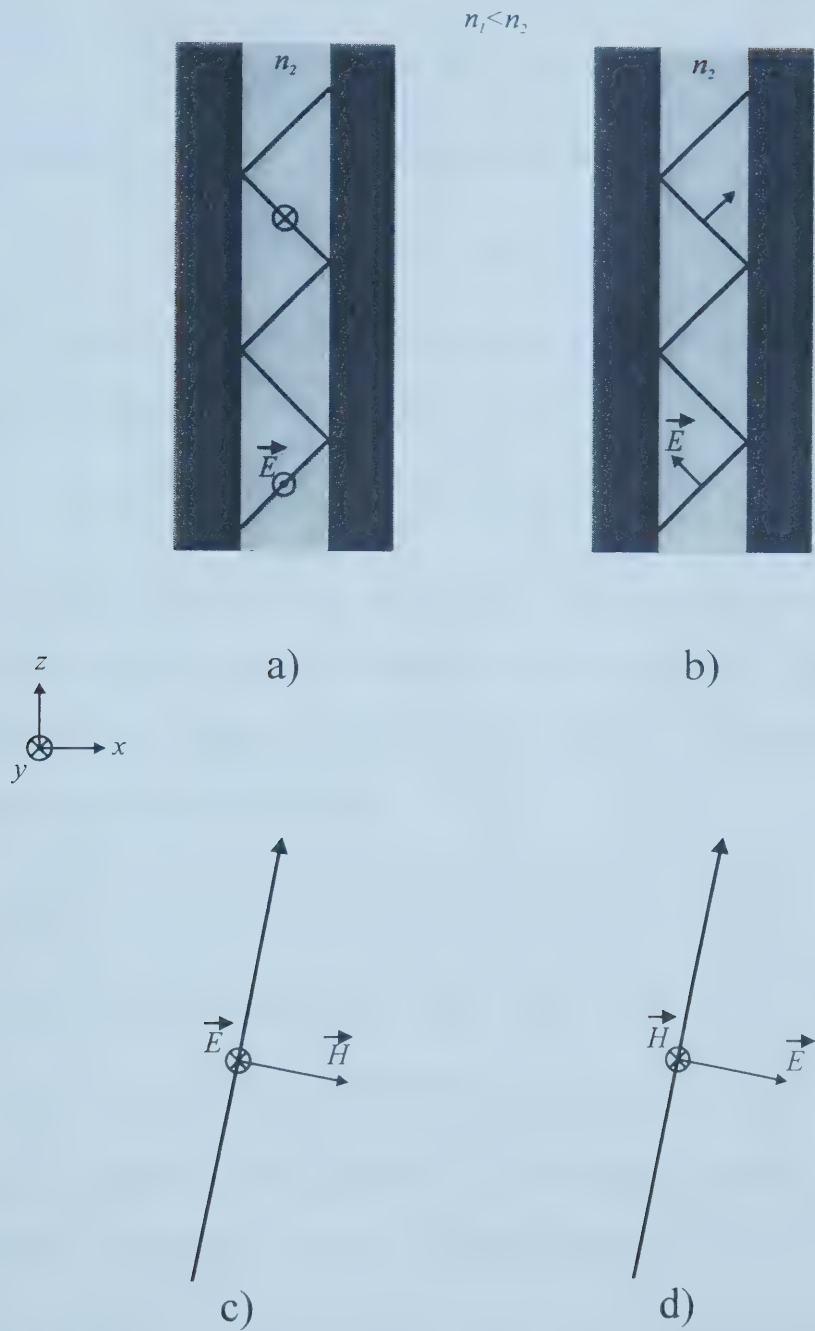


Figure 3.1. Geometrical light rays for a) TE and b) TM modes in a slab waveguide, and c) TE and d) TM modes in free space.

$$\frac{\partial^2 E_y}{\partial x^2} + \frac{\partial^2 E_y}{\partial z^2} - \omega^2 \mu_0 \epsilon_0 i \xi E_x + \omega^2 \mu_0 \epsilon_0 \epsilon_y E_y = 0, \quad (3.1.6)$$

the x -component of Ampere's Law which relates E_x and E_y to H_y ,

$$-\frac{\partial H_y}{\partial z} = i\omega \epsilon_0 (\epsilon_x E_x + i \xi E_y), \quad (3.1.7)$$

and by neglecting terms quadratic in ξ (as they are a small perturbation to the dielectric tensor), the following equation is obtained:

$$\frac{\omega \mu_0 \xi}{\epsilon_x} \frac{\partial H_y}{\partial z} + \frac{\partial^2 E_y}{\partial x^2} + \frac{\partial^2 E_y}{\partial z^2} + \omega^2 \mu_0 \epsilon_0 \epsilon_y E_y = 0. \quad (3.1.8)$$

While equation 3.1.8 is an appropriate form, since the Faraday effect (i.e. polarization rotation) couples the both the TE and the TM modes, a second equation is required to form a solution for E_y and H_y . Such a relation can be obtained by considering the y -component of equation (3.1.5),

$$\frac{\partial}{\partial x} \frac{1}{\epsilon_x} \frac{\partial H_y}{\partial x} + \frac{\partial}{\partial z} \frac{1}{\epsilon_x} \frac{\partial H_y}{\partial z} - \frac{\partial}{\partial z} \frac{i \xi}{\epsilon_x \epsilon_y} \left(\frac{\partial H_z}{\partial x} - \frac{\partial H_x}{\partial z} \right) + \omega^2 \mu_0 \epsilon_0 H_y = 0 \quad (3.1.9)$$

and the y -component of Amperes law relating H_x , H_z , and E_y ,

$$-\frac{\partial H_z}{\partial x} + \frac{\partial H_x}{\partial z} = i\omega \epsilon_0 (-i \xi E_x + \epsilon_y E_y). \quad (3.1.10)$$

Again, by neglecting terms quadratic in ξ , the following equation is obtained by substituting the third term of equation 3.1.9 with the left hand side of 3.1.10:

$$-\epsilon_x \frac{\partial}{\partial z} \frac{\omega \epsilon_0 \xi}{\epsilon_x} E_y + \epsilon_x \frac{\partial}{\partial x} \frac{1}{\epsilon_x} \frac{\partial H_y}{\partial x} + \epsilon_x \frac{\partial}{\partial z} \frac{1}{\epsilon_x} \frac{\partial H_y}{\partial z} + \omega^2 \mu_0 \epsilon_0 \epsilon_x H_y = 0. \quad (3.1.11)$$

Equations 3.1.8 and 3.1.11 can be further simplified by considering only forward wave propagation along the z -axis. To do this, the following substitutions are made:

$E_y = E \exp(-i\beta z)$ and $H_y = H \exp(-i\beta z)$, where E and H are the field amplitudes of the TE and TM modes and β is the propagation constant. Under the slowly varying amplitude approximation, in which second order z derivatives of the amplitudes are ignored, the following equation is obtained:

$$\hat{P} \begin{pmatrix} E \\ H \end{pmatrix} + \hat{Q} \frac{\partial}{\partial z} \begin{pmatrix} E \\ H \end{pmatrix} = 0, \quad (3.1.12)$$

where \hat{P} and \hat{Q} are the following differential operators

$$\hat{P} = \begin{pmatrix} \frac{\partial^2}{\partial x^2} + \omega^2 \epsilon_0 \epsilon_y \mu_0 - \beta^2 & -i \frac{\beta \omega \mu_0}{\epsilon_x} \xi(t) \\ i \beta \omega \epsilon_0 \xi(t) & \epsilon_x \frac{\partial}{\partial x} \frac{1}{\epsilon_z} \frac{\partial}{\partial x} + \omega^2 \epsilon_0 \epsilon_x \mu_0 - \beta^2 \end{pmatrix} \quad (3.1.13)$$

and

$$\hat{Q} = \begin{pmatrix} -2i\beta & \frac{\omega \mu_0}{\epsilon_z} \xi(t) \\ -\omega \epsilon_0 \xi(t) & -2i\beta \end{pmatrix}. \quad (3.1.14)$$

Equation 3.1.12 describes the propagation of light-waves in a material with a time-dependent Faraday rotation.

The value of β must be calculated separately and depends on the geometry under investigation. For example, in the modeling of the MO modulator, β is calculated for the first order mode of a waveguide from the equation

$$\beta = \sqrt{\left(\frac{k_0}{n}\right)^2 - \left(\frac{\pi}{a}\right)^2} \quad (3.1.15)$$

which has been derived for a slab waveguide configuration [4]. Here, k_0 is the free-space wave-vector, n is the refractive index of the mode, and a is the width of the slab.

In arriving at these results, it has been assumed that the refractive index and Faraday rotation profiles do not vary with z or are slowly varying. Therefore, derivatives, with respect to z of the dielectric constants and the Faraday rotation are assumed to be zero.

3.1.2 Discretization of Beam Propagation Equations

Equation 3.1.12 derived above does not have a closed form solution, and therefore, it is converted into difference equation that is solved numerically. To begin the process of discretization, equation 3.1.12 is expanded to give

$$\frac{\partial^2 E}{\partial x^2} + k_0^2 \varepsilon_y E - \beta^2 E - i\beta \sqrt{\frac{\mu_0}{\varepsilon_0}} k_0 \frac{\xi}{\varepsilon_x} H - 2i\beta \frac{\partial E}{\partial z} + \sqrt{\frac{\mu_0}{\varepsilon_0}} k_0 \frac{\xi}{\varepsilon_x} \frac{\partial H}{\partial z} = 0 \quad (3.1.16)$$

and

$$i\beta \sqrt{\frac{\varepsilon_0}{\mu_0}} k_0 \xi E + \varepsilon_x \frac{\partial}{\partial x} \frac{1}{\varepsilon_x} \frac{\partial H}{\partial x} + k_0^2 \varepsilon_x H - \beta^2 H - \sqrt{\frac{\varepsilon_0}{\mu_0}} k_0 \xi \frac{\partial E}{\partial z} - 2i\beta \frac{\partial H}{\partial z} = 0 \quad (3.1.17)$$

where ω has been replaced with $k_0 / \sqrt{\varepsilon_0 \mu_0}$.

To obtain numerical solutions, the treatment proposed by Erdmann and Hertel [3] is followed and equations 3.1.16 and 3.1.17 are discretized using the Crank-Nicolson scheme [5]. The difference forms for the derivatives are given in Appendix B [5,6], and are applied to equations 3.1.16 and 3.1.17 to give

$$\begin{aligned} & \frac{E_{m+1}^l - 2E_m^l + E_{m-1}^l}{2(\Delta x)^2} + \frac{E_{m+1}^{l+1} - 2E_m^{l+1} + E_{m-1}^{l+1}}{2(\Delta x)^2} + k_0^2 \varepsilon_y^{(m,l)} \left(\frac{E_m^{l+1} + E_m^l}{2} \right) \\ & - \beta^2 \left(\frac{E_m^{l+1} + E_m^l}{2} \right) - i\beta \sqrt{\frac{\mu_0}{\varepsilon_0}} k_0 \frac{\xi}{\varepsilon_x^{(m,l)}} \left(\frac{H_m^{l+1} + H_m^l}{2} \right) \\ & - 2i\beta \left(\frac{E_m^{l+1} - E_m^l}{\Delta z} \right) + \sqrt{\frac{\mu_0}{\varepsilon_0}} k_0 \frac{\xi}{\varepsilon_x^{(m,l)}} \left(\frac{H_m^{l+1} - H_m^l}{\Delta z} \right) = 0 \end{aligned} \quad (3.1.18)$$

and

$$\begin{aligned}
& i\beta\sqrt{\frac{\varepsilon_0}{\mu_0}}k_0\xi^{(m,l)}\left(\frac{E_m^{l+1}+E_m^l}{2}\right)+\left(k_0^2\varepsilon_x^{(m,l)}-\beta^2\right)\left(\frac{H_m^{l+1}+H_m^l}{2}\right) \\
& -\sqrt{\frac{\varepsilon_0}{\mu_0}}k_0\xi^{(m,l)}\left(\frac{E_m^{l+1}-E_m^l}{\Delta z}\right)-2i\beta\left(\frac{H_m^{l+1}-H_m^l}{\Delta z}\right) \\
& -\frac{\varepsilon_x^{(m,l)}}{2(\Delta x)^2}\left(\frac{2}{\varepsilon_z^{(m+1,l)}+\varepsilon_z^{(m,l)}}(H_{m+1}^l-H_m^l)-\frac{2}{\varepsilon_z^{(m,l)}+\varepsilon_z^{(m-1,l)}}(H_{m+1}^l-H_m^l)\right. \\
& \left.+\frac{2}{\varepsilon_z^{(m+1,l)}+\varepsilon_z^{(m,l)}}(H_{m+1}^{l+1}-H_m^{l+1})-\frac{2}{\varepsilon_z^{(m,l)}+\varepsilon_z^{(m-1,l)}}(H_{m+1}^{l+1}-H_m^{l+1})\right)=0
\end{aligned} \tag{3.1.19}$$

where Δx and Δz are the step sizes in the x and z directions, respectively. The dielectric and Faraday rotation functions are evaluated at $x=m\Delta x$ and $z=l\Delta z$.

The above equations are multiplied by $i\Delta z$ and terms are collected according to the position in z ; l terms are moved to the right-hand side and $l+1$ terms are moved to the left-hand side. This results in the following set of equations:

$$\begin{aligned}
& -2\beta E_m^{l+1}-i\sqrt{\frac{\mu_0}{\varepsilon_0}}k_0\frac{\xi^{(m,l)}}{\varepsilon_x^{(m,l)}}H_m^{l+1} \\
& -\frac{i\Delta z}{2}\left(\frac{E_{m+1}^{l+1}-2E_m^{l+1}+E_{m-1}^{l+1}}{(\Delta x)^2}+k_0^2\varepsilon_y^{(m,l)}E_m^{l+1}-\beta^2-i\beta\sqrt{\frac{\mu_0}{\varepsilon_0}}k_0\frac{\xi^{(m,l)}}{\varepsilon_x^{(m,l)}}H_m^{l+1}\right)= \\
& -2\beta E_m^l-i\sqrt{\frac{\mu_0}{\varepsilon_0}}k_0\frac{\xi^{(m,l)}}{\varepsilon_x^{(m,l)}}H_m^l \\
& +\frac{i\Delta z}{2}\left(\frac{E_{m+1}^l-2E_m^l+E_{m-1}^l}{(\Delta x)^2}+k_0^2\varepsilon_y^{(m,l)}E_m^l-\beta^2-i\beta\sqrt{\frac{\mu_0}{\varepsilon_0}}k_0\frac{\xi^{(m,l)}}{\varepsilon_x^{(m,l)}}H_m^l\right)
\end{aligned} \tag{3.1.20}$$

and

$$\begin{aligned}
& i \sqrt{\frac{\varepsilon_0}{\mu_0}} k_0 \xi^{(m,l)} E_m^{l+1} - 2\beta H_m^{l+1} \\
& - \frac{i\Delta z}{2} \left[i\beta \sqrt{\frac{\varepsilon_0}{\mu_0}} k_0 \xi^{(m,l)} E_m^{l+1} - \frac{\varepsilon_x^{(m,l)}}{(\Delta x)^2} \left(\frac{2}{\varepsilon_z^{(m+1,l)} + \varepsilon_z^{(m,l)}} (H_{m+1}^{l+1} - H_m^{l+1}) \right) \right. \\
& \quad \left. - \left(\frac{2}{\varepsilon_z^{(m,l)} + \varepsilon_z^{(m-1,l)}} (H_{m,l}^{l+1} - H_{m-1,l}^{l+1}) \right) + (k_0^2 \varepsilon_x^{(m,l)} - \beta^2) H_m^{l+1} \right] \\
& = i \sqrt{\frac{\varepsilon_0}{\mu_0}} k_0 \xi^{(m,l)} E_m^l - 2\beta H_m^l \\
& \quad + \frac{i\Delta z}{2} \left[i\beta \sqrt{\frac{\varepsilon_0}{\mu_0}} k_0 \xi^{(m,l)} E_m^l - \frac{\varepsilon_x^{(i)}}{(\Delta x)^2} \left(\frac{2}{\varepsilon_z^{(m+1,l)} + \varepsilon_z^{(m,l)}} (H_{m+1}^l - H_m^l) \right) \right. \\
& \quad \left. - \left(\frac{2}{\varepsilon_z^{(m,l)} + \varepsilon_z^{(m-1,l)}} (H_m^l - H_{m-1}^l) \right) + (k_0^2 \varepsilon_x^{(m,l)} - \beta^2) H_m^l \right]
\end{aligned} \tag{3.1.21}$$

These equations can be represented more elegantly in the matrix form:

$$\left(\hat{R} - \frac{i\Delta z}{2} \hat{S} \right) \vec{v}_{l+1} = \left(\hat{R} + \frac{i\Delta z}{2} \hat{S} \right) \vec{v}_l, \tag{3.1.22}$$

where $\vec{v}_l = (E_0^l, E_1^l, \dots, E_m^l, \dots, E_M^l, H_0^l, H_1^l, \dots, H_m^l, \dots, H_M^l)$ and \hat{R} and \hat{S} are propagation matrices whose non-zero elements (evaluated at $z=l\Delta z$) are:

$$(\hat{R})_{m,m} = -2\beta$$

$$(\hat{R})_{m,m+M} = -i \sqrt{\frac{\mu_0}{\varepsilon_0}} k_0 \frac{\xi^{(m)}}{\varepsilon_z^m}$$

$$(\hat{S})_{m,m-1} = \frac{1}{(\Delta x)^2}$$

$$(\hat{S})_{m,m} = -\frac{2}{(\Delta x)^2} + k_0^2 \varepsilon_y^{(m)} - \beta^2$$

$$(\hat{S})_{m,m+1} = \frac{1}{(\Delta x)^2}$$

$$(\hat{S})_{m,m+M} = -i \sqrt{\frac{\mu_0}{\epsilon_0}} k_0 \beta \frac{\xi^{(m)}}{\epsilon_z^{(m)}}$$

$$(\hat{R})_{m+M,m} = i \sqrt{\frac{\epsilon_0}{\mu_0}} k_0 \xi^{(m)}$$

$$(\hat{R})_{m+M,m+M} = -2\beta$$

$$(\hat{S})_{m+M,m} = i \sqrt{\frac{\epsilon_0}{\mu_0}} k_0 \beta \xi^{(m)}$$

$$(\hat{S})_{m+M,m+M-1} = \frac{2\epsilon_x^{(m)}}{(\Delta x)^2 (\epsilon_z^{(m-1)} + \epsilon_z^{(m)})}$$

$$(\hat{S})_{m+M,+M} = -\frac{2\epsilon_x^{(m)}}{(\Delta x)^2 (\epsilon_z^{(m-1)} + \epsilon_z^{(m)})} - \frac{2\epsilon_x^{(m)}}{(\Delta x)^2 (\epsilon_z^{(m)} + \epsilon_z^{(m+1)})} + k_0^2 \epsilon_x^{(m)} - \beta^2$$

$$(\hat{S})_{m+M,m+M+1} = \frac{2\epsilon_x^{(m)}}{(\Delta x)^2 (\epsilon_x^{(m)} + \epsilon_x^{(m+1)})}$$

Each component of \vec{v}_l in equation 3.1.22 represents the amplitudes of the TE and TM modes at mesh point ($x=m\Delta x$, $z=l\Delta z$). Equation 3.1.22 can be solved for \vec{v}_{l+1} , and the entire mesh of points can be determined iteratively from an initial vector \vec{v}_0 . It should be noted that the vector \vec{v}_l has $2M+2$ elements, and \hat{R} and \hat{S} are $(2M+2) \times (2M+2)$ matrices, where M is the total number of points in the x -direction.

Figure 3.2 gives a schematic representation of typical \hat{R} and \hat{S} matrices used in these calculations. The matrix can be effectively divided into four quadrants as shown in figure 3.2. Quadrants I and IV govern wave propagation while quadrants II and III govern coupling between the TE and TM modes. For regions without Faraday rotation, $\xi=0$, all

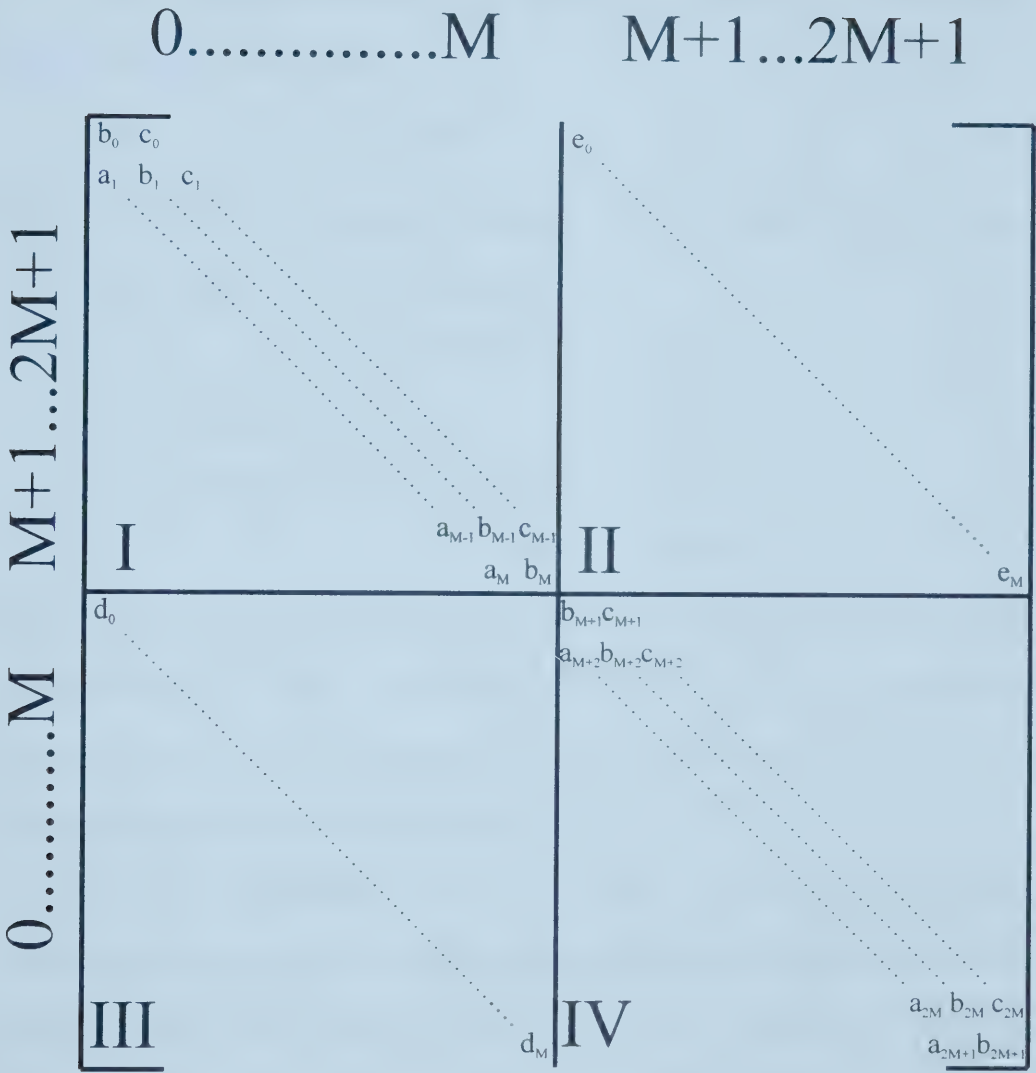


Figure 3.2. Schematic representation of the matrices used for the beam propagation method.

elements of quadrants II and III become zero, and the propagation matrices become tri-diagonal. In this case, the TE and TM mode propagation is independent and not coupled.

To solve equation 3.1.22 effectively in a numerical algorithm, the right-hand side is computed first to give the form

$$\hat{A}\vec{v}_{l+1} = \hat{b} \quad (3.1.23)$$

where \hat{A} is a matrix of the form shown in figure 3.2. It is observed that \hat{A} is a sparse matrix, and the number of non-zero elements is:

Center diagonal	2M+2
Off diagonals in quadrants I and IV	+2*2M
Diagonals in quadrants II and III	<u>+2*(M+1)</u>
Total	=8M+4

The total number of elements is $(2M+2)^2$, and therefore, the fraction of non-zero elements is $(8M+4)/(2M+2)^2$. A typical value for M was 200, and in such a case, the fraction of non-zero elements are ~ 0.01 . Therefore, an iterative Jacobi method [7] is employed to reduce computation time in solving equation 3.1.22.

Since the computational window is of finite dimension, proper boundary conditions must be employed to avoid erroneous effects. If no condition is placed on the boundary, incident waves will be reflected. To damp such reflections an absorbing boundary mesh is used. For this condition, a decaying exponential is applied, along the x-direction, to both the TE and TM profiles at the computational window boundaries. This condition is applied separately at each step in z. The number of points used for this typically comprised 10-20% of the total number of points in x.

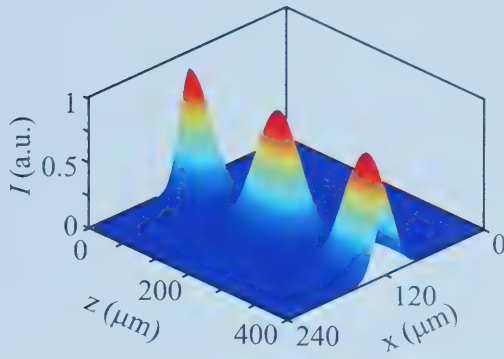
With all these equations in mind, a computer algorithm was written in Visual C++ to generate the outputs in the following simulations. This computer algorithm is reproduced in Appendix A.

3.2 Theoretical Modeling of the Magneto-Optic Modulator

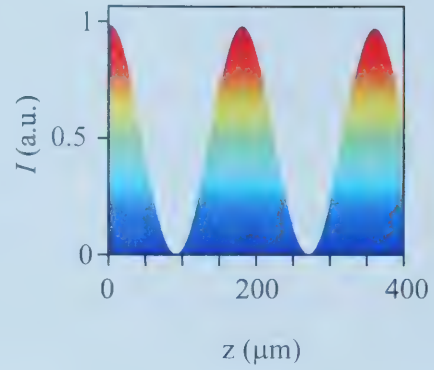
This section describes the modeling of MO modulation using the BPM-LL derived above. Before modeling the MO modulator, the results from a simple test run are discussed. Following this, the general geometry of the MO modulator is presented and described, and the BPM-LL is used to model its operation at a wavelength of 1550 nm with ideal parameters. Next, the MO modulator operation is modeled again at 800 nm, since the experimental set-up described in Chapter 4 is designed for this wavelength. The effects of birefringence on mode conversion are addressed, leading to the simulation results for the MO modulator using actual experimental parameters.

3.2.1 Time-Independent Light Propagation in a Bulk Magneto-Optic Material

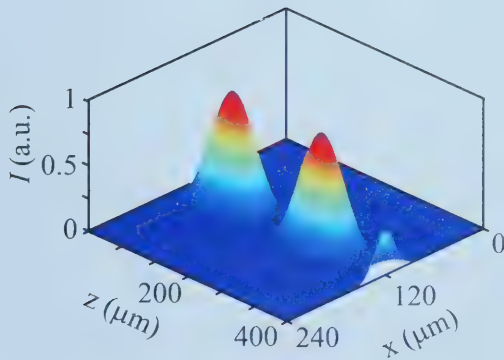
To verify the program operation, an initial test, in which the results are easily calculable, is performed. For this, consider the hypothetical case of propagation in a bulk MO material with no birefringence, an index of refraction of 1.0, and a constant Faraday rotation of $1^\circ/\mu\text{m}$. Therefore, if a TE mode is launched, it is expected that full mode conversion into the TM polarization will occur at a distance of $90\ \mu\text{m}$ (i.e. the polarization will be rotated 90°). Using these parameters, the time-independent BPM calculates the data presented in figure 3.3 in a run-time of approximately 4 minutes (on a Pentium III 866 MHz system). Here, a Gaussian beam with FWHM equal to $40\ \mu\text{m}$ is



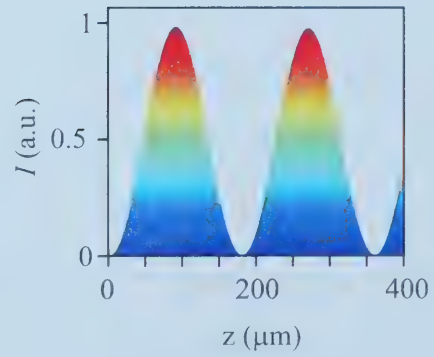
a)



b)



c)



d)

Figure 3.3. Propagation in a bulk material that has a non-zero Faraday rotation of $1.0^\circ/\mu\text{m}$ and index of refraction of 1. a) TE polarization , b) side view of the TE wave c) TM polarization , d) side view of the TM wave.

launched with a TE polarization at a wavelength of 800 nm. The plots in figure 3.3 illustrate that the polarization is, indeed, completely converted from TE to TM at a distance of 90 μm . The TE mode power is continuously reduced to zero as the corresponding TM power increases towards the value of the original power launched in the TE mode. Once the polarization has been completely rotated into the TM mode, the polarization begins to rotate back into the TE mode, which has its second maximum at 180 μm . This process of polarization rotation continues indefinitely in such an MO medium.

3.2.2 Geometry of the Magneto-Optic Modulator

The BPM-LL developed above can now be applied to study the MO modulator depicted in figure 3.4. It is assumed that a Bi-YIG film has been grown on a gadolinium gallium garnet (GGG) substrate. A typical value of the refractive index for the Bi-YIG is 2.3, although the refractive indices of the TE and TM modes will be varied (in section 3.2.4) to demonstrate the effects of birefringence. The GGG substrate has a refractive index of 1.94, and a cladding layer of a refractive index of 1.94 is placed atop the Bi-YIG film. Experimentally, an additional layer of metal layer would be placed over the cladding to serve as a transmission line. However, since the cladding layer is 1.0 μm thick, the effects of the metal transmission line are not considered in the model. To couple light to the Bi-YIG film, a Gaussian beam is launched with a FWHM equal to the width of the waveguide. Since absorption is not included in the model, the device length, d , will be limited to one propagation length at the specified wavelength (1550 or 800 nm).

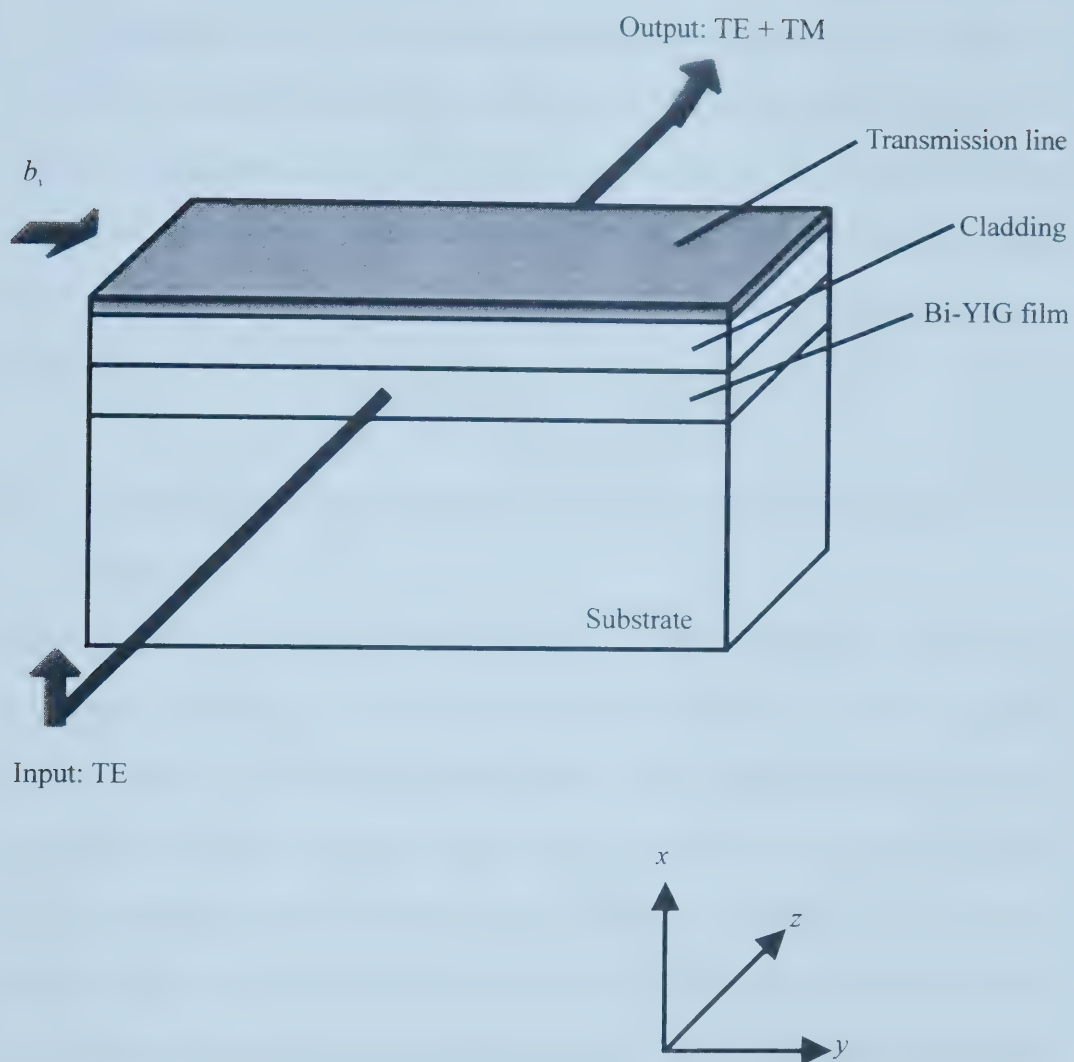


Figure 3.4. Schematic diagram of the MO modulator.

Here, the direction of the externally applied biasing magnetic field is taken to be along the y -direction. As discussed in section 2.3, this static magnetic field is required to switch magnetization of the Bi-YIG film into and out of the direction of optical propagation. Since the LL model considers a uniformly magnetized film, it is assumed that this biasing field initially saturates the magnetization of the Bi-YIG film along the y -direction.

3.2.3 Modeling of the Magneto-Optic Modulator at 1550 nm with Idealized Parameters

Using the BPM-LL, the MO modulation device is modeled under ideal conditions at a wavelength of 1550 nm. At this wavelength, the Bi-YIG film is set to have a specific Faraday rotation of 2500 %/cm and a thickness of 1.0 μm . To properly match the TM and TE propagation rates, the refractive indices are set to their optimum values of $n_x=2.2400$ and $n_y=2.2300$ (the effects of birefringence are addressed in section 3.2.4). To illustrate the fact that the velocities of the modes are properly matched, the BPM is used to model the static mode conversion of the device assuming a constant saturated magnetization along the z -direction. The results are shown in figure 3.5, where a complete mode conversion occurs at a distance of 396 μm . Realistically, one absorption depth is at most 300 μm , and therefore, the length of the device, d , is taken to be this value. According to the simulation output in figure 3.5, the mode conversion reaches 80 % at 300 μm .

The next step is to include the time-dependence of the device and model its response to modulating magnetic field pulses produced by electrical signals carried by the

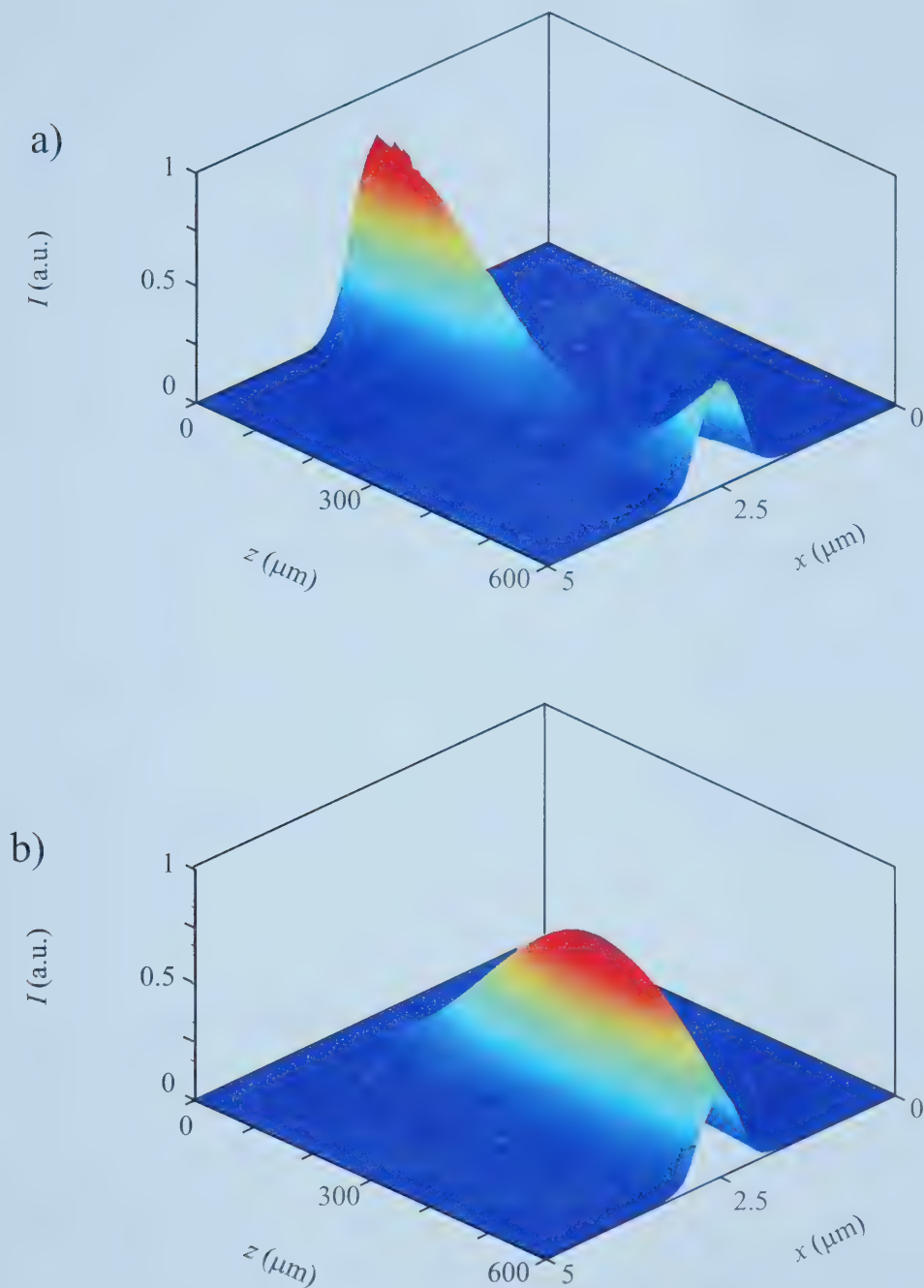


Figure 3.5. Static a) TE to b) TM mode conversion for constant magnetization along the z -direction. Complete mode conversion occurs at a distance of $396 \mu\text{m}$.

transmission line. As outlined in section 3.1, this is achieved by incorporating the LL formalism in the BPM. In order to provide a realistic representation of an actual modulator performance, the electrical input is chosen to be a signal train consisting of three Gaussian pulses with amplitudes corresponding to a peak magnetic field transient of 50 mT. The pulse spacing is chosen to be four times longer than the FWHM of a single pulse so that the individual pulses do not overlap. Figure 3.6 illustrates the typical output intensity (i.e. TM polarization) of the modulator, where it is observed that the electrical pulse train is effectively mapped onto the optical carrier. Static magnetic field values of 60, 90, 375, 750 mT are used for pulses with FWHM of 1 ns, 200 ps, 100 ps, and 50 ps, respectively. These magnetic fields are chosen in order to maximize the device output. Dynamic mode conversions efficiencies of 42%, 11%, 4% and 1% are obtained for driving pulses of 1 ns, 200 ps, 100 ps, and 50 ps, respectively. The residual inter-pulse oscillation due to FMR is present, but is quite small (<3% of the main signal amplitude) and can be eliminated by using a higher biasing magnetic field strength.

3.2.4 Effects of Birefringence on Static Mode Conversion at 800 nm

Since the experimental set-up discussed in Chapter 4 is designed for a wavelength of 800 nm, the BPM simulations for the MO modulator are repeated at this wavelength to gain an understanding of the device and predict its efficiency.

It is well known that TE and TM modes have different propagation velocities in waveguides; an effect known as geometrical birefringence. Hence, a non-zero value for the material birefringence must be used to compensate for the geometrical birefringence to allow complete mode conversion to occur. Using the optimal values of the refractive

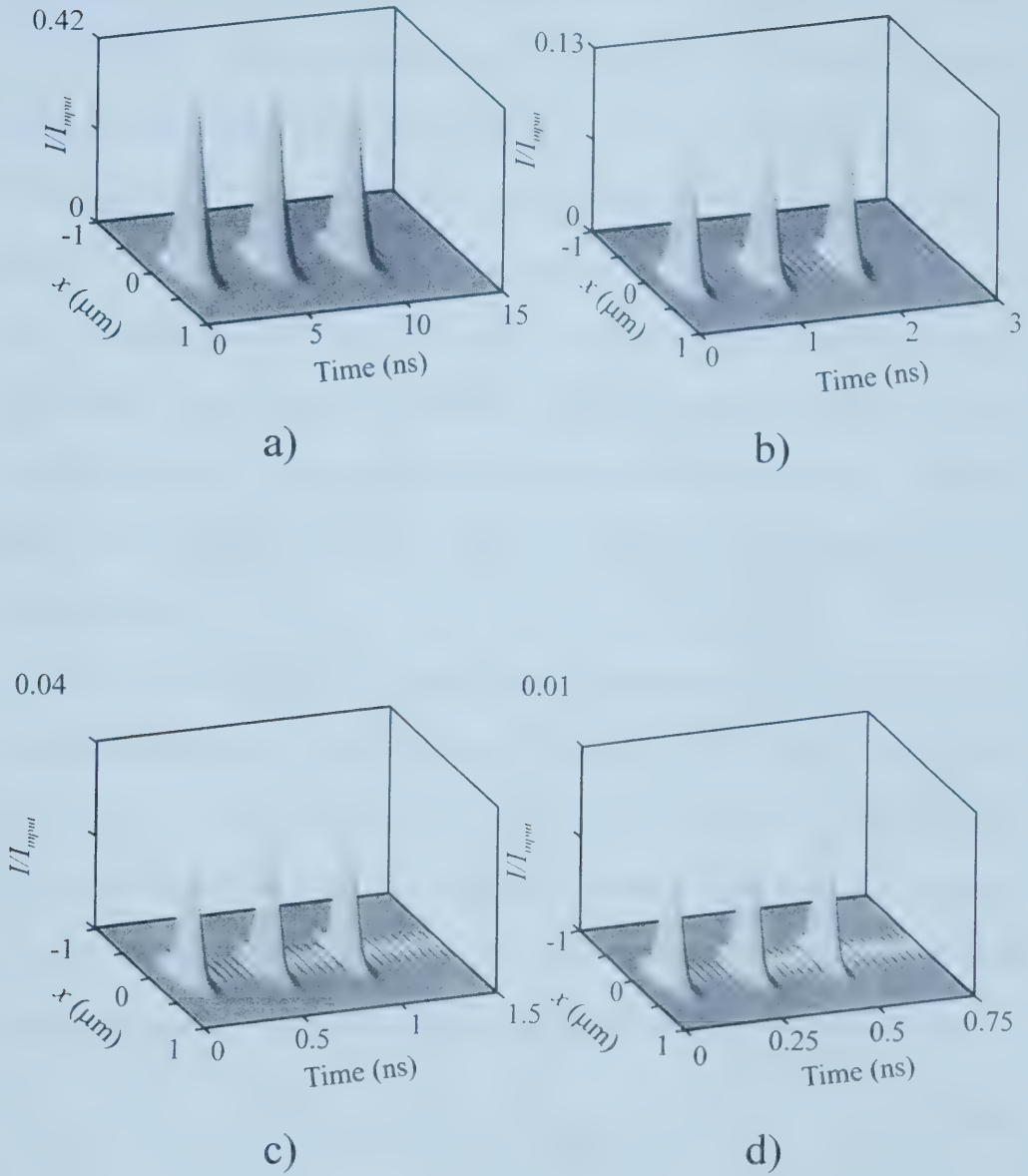


Figure 3.6. Simulated spatio-temporal output of the MO modulator corresponding to an input of three sequential current pulses at four selected FWHM of a) 1 ns, b) 200 ps, c) 100 ps, d) 50 ps.

indices $n_x=2.3000$ and $n_y=2.2602$, the static mode conversion of the modulator is shown in figure 3.7a, where the intensity of the TE and TM modes are plotted as functions of transverse (x) and longitudinal (z) directions. At a wavelength of 800 nm, the Faraday rotation and the thickness of the Bi-YIG film are taken to be 5400 °/cm and 0.25 μm , respectively. It can be seen in the figure that complete mode conversion occurs at a distance of 175 μm . The propagation constants of the two polarization modes are properly matched, and as a result, 100% mode conversion occurs. In reality, absorption would limit the device length to one absorption depth at 800 nm. For the Bi-YIG material discussed in Chapter 4, one absorption depth at 800 nm corresponds to $\sim 25 \mu\text{m}$. As indicated by the simulation results in figure 3.7a, mode conversion reaches 5% at a distance of 25 μm .

Plots b and c of figure 3.7 demonstrate the result of varying the refractive indices from their optimal values of $n_x=2.3000$ and $n_y=2.2602$. The index along the x -direction is fixed, while n_y is changed to 2.259 and 2.25 for figures 3.7b and 3.7c, respectively. As the velocity mismatch is increased, the coupling efficiency between the modes is reduced. It has been shown from coupled-mode theory that the maximum efficiency of mode conversion for a given value of the birefringence, $\Delta\beta$, and the Faraday rotation is [8]

$$\eta_{\text{efficiency}} = \frac{\theta_F^2}{\left(\theta_F^2 + \left(\frac{\Delta\beta}{2} \right)^2 \right)}. \quad (3.2.1)$$

This is an important consideration, as birefringence (both material and geometrical) is inherent in Bi-YIG films, and proper devices based on such films should have the birefringence compensated to properly match the TE and TM modes to increase the device efficiency [9].

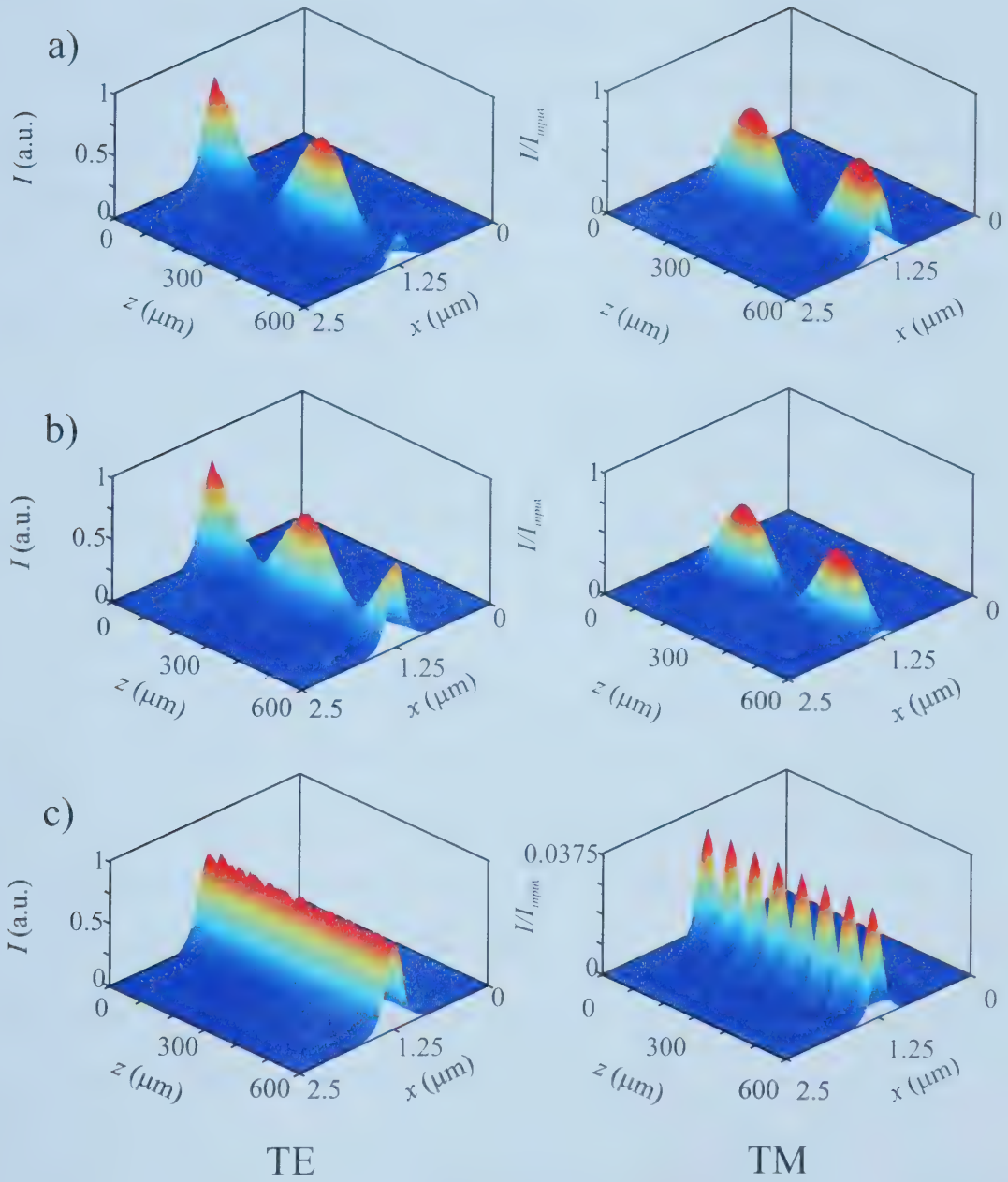


Figure 3.7. Effect of birefringence on TE (left hand column) to TM (right hand column) mode conversion for various values of index. a) $n_i=2.3$, $n_t=2.2602$, b) $n_i=2.3$, $n_t=2.259$, c) $n_i=2.3$, $n_t=2.25$.

3.2.5 Magnetic Field due to a Transmission Line

In modeling the MO modulator with actual experimental conditions, it is essential to properly calculate the magnetic field distribution due a transmission line of rectangular cross-section, which is the type of transmission line that is used for the actual MO modulator described in Chapter 4. To allow accurate estimates of efficiency, this transmission line configuration has been incorporated into the BPM-LL model for calculating the magnetic field spatial distribution, and is derived as follows.

Using Ampere's law for a simple current carrying wire with infinite extent in the y -direction, the magnetic field spatial distribution outside the wire is given by

$$B' = \frac{\mu_0 I}{2\pi R} (-\sin(\theta) \hat{x} + \cos(\theta) \hat{z}) \quad (3.2.2)$$

where I is the current passing through the wire, R is the distance from the wire, θ is the angle in a polar coordinate system measured from the positive x -axis towards the positive z -axis, and \hat{x} and \hat{z} are the unit vectors in the x and z directions, respectively. Since we require the magnetic field distribution due to a transmission line with a rectangular cross section and constant current density, integration of equation 3.2.2 must be performed over the region of interest for each current-wire element, as depicted in figure 3.8. Equation 3.2.2 can be represented in a Cartesian coordinate system by the following:

$$B' = \frac{\mu_0 I}{2\pi\sqrt{x^2 + z^2}} \left(-\frac{z}{\sqrt{x^2 + z^2}} \hat{x} + \frac{x}{\sqrt{x^2 + z^2}} \hat{z} \right). \quad (3.2.3)$$

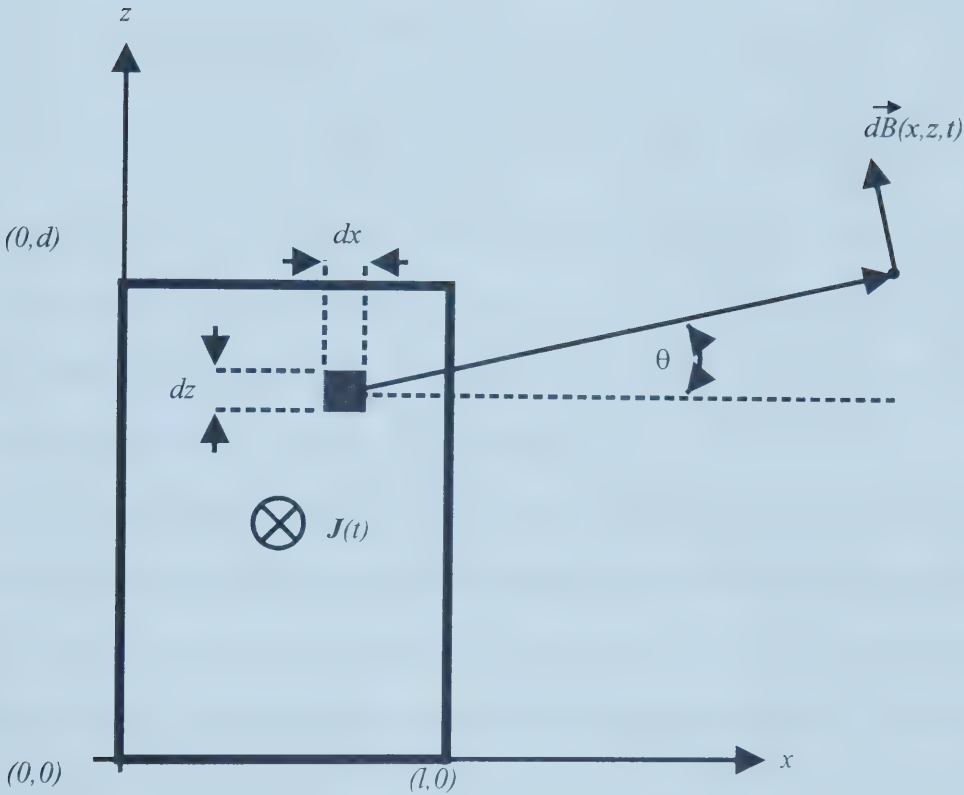


Figure 3.8. Cross-sectional view of a rectangular transmission line having width l and thickness d .

To arrive at an analytical solution for the magnetic field, equation 3.2.3 is integrated over to obtain:

$$B'_z(x,z) = \frac{\mu_0 I}{2\pi ld} \left[\begin{aligned} &(l-x) \arctan\left(\frac{z}{x-l}\right) + (x-l) \arctan\left(\frac{z-d}{x-l}\right) \\ &+ \frac{1}{2} (z-d) \ln \left[\frac{(x-l)^2 + (z-d)^2}{x^2 + (z-d)^2} \right] \\ &+ \frac{1}{2} z \ln \left(\frac{z^2 + x^2}{(x-l)^2 + z^2} \right) + x \left[\arctan\left(\frac{z}{x}\right) - \arctan\left(\frac{z-d}{x}\right) \right] \end{aligned} \right] \quad (3.2.4)$$

where l and d are the dimensions of the transmission line in the x and z directions, respectively (the coordinate system is given in figure 3.8). Figure 3.9 displays the spatial distribution of the magnitude of the magnetic field due to a single transmission of rectangular cross-section with $l=20 \mu\text{m}$ and $d=2 \mu\text{m}$.

In this simulation, the modulation times are much longer ($\sim 1 \text{ ns}$) than the transit time of electromagnetic fields (a few picoseconds), thus, the changes in the magnetic field are considered to be instantaneous along the transmission line. For the calculations discussed below, a time-dependent factor of Gaussian form is included in $B'_z(x,t)$ such that the transient field is of the form

$$b_z(x,z,t) = B'_z(x,z) \exp[-t^2]. \quad (3.2.5)$$

The time and spatially varying magnetic field can be incorporated into the BPM-LL by calculating the z -component of the magnetic field at each mesh point. Each point on the space-mesh is considered to be an independent domain and the LL equation is applied to that node to calculate the degree of magnetization along z , $M_z(t)$, and hence, the Faraday rotation.

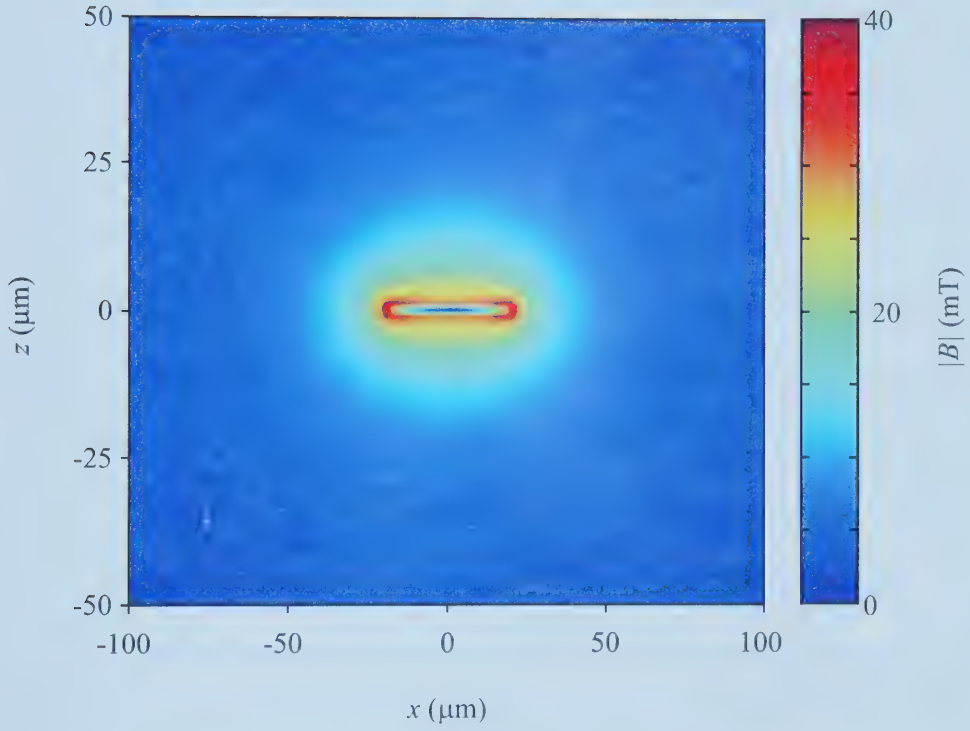


Figure 3.9. Spatial distribution of the magnitude of the magnetic field due to a transmission line of rectangular cross-section with $l=20\text{ }\mu\text{m}$, $d=2\text{ }\mu\text{m}$.

3.2.6 Modeling of the Magneto-Optic Modulator at 800 nm with Experimental Parameters

With the aid of the BPM-LL and the transmission line model discussed in section 3.2.5, a great deal of information about the efficiency of the device is gained. Using the actual parameters of the Bi-YIG film, the MO modulator and the driving pulses, the output of the device is calculated and illustrated in figure 3.10. This figure displays a still picture of the device at 2.5 ns (2.5 ns is the center of the Gaussian), along with the time-dependent output. The parameters of the Bi-YIG and the MO modulator are listed in the figure caption, and since no measured values for the birefringence are available at this wavelength, the optimum value for mode conversion efficiency is used. The electrical input consisted of a single Gaussian pulse with a width of 2.5 ns with a current amplitude of 18 mA. The value of the biasing field is equal to 22.5 mT which was chosen to maximize the signal amplitude.

The overall efficiency of the device, defined to be the ratio of output power in the TM mode to the input power of the TE mode, calculated from figure 3.10, is 3.3×10^{-6} and corresponds to a polarization rotation angle of 0.1° . However, due to absorption, the actual value for the efficiency is $3.3 \times 10^{-6} * e^{(-60/25)} = 0.3 \times 10^{-6}$. It should be noted that in order to match the experimental situation, the device length, d , was chosen to be $60 \mu\text{m}$ to provide a realistic value for the efficiency.

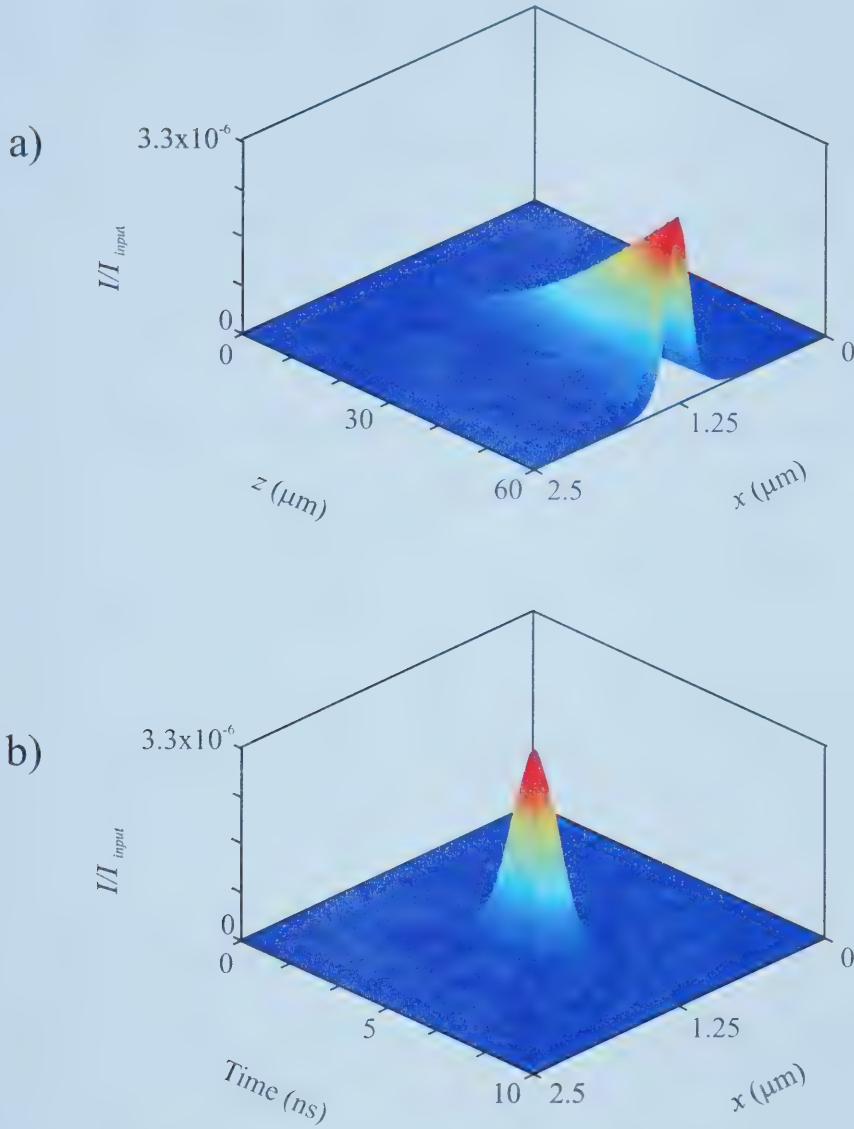


Figure 3.10. Time-dependent output of the MO modulator in response to an electrical input of a single 2.5 ns employing the actual transmission line structure. a) Time snapshot of the TM polarization throughout MO modulator. b) Time varying output of the MO modulator. $l=100 \mu\text{m}$, $d=60 \mu\text{m}$, $n_i=2.3$, $n_f=2.2602$, film thickness $a=0.25 \mu\text{m}$, Faraday rotation = 5400 $^\circ/\text{cm}$.

3.3 Proposal of a High-Speed Magneto-Optic Beam Deflector

A novel device for fiber-optic communications is a MO beam deflector. This section describes such a device that is based on the MO Faraday effect. The device may find applications for wavelength division multiplexing and high-speed switching. The device proposed would act essentially as a diffraction grating, and much like the passive diffraction phase grating, the deflected optical beams diffract at different angles that are defined by their wavelengths and the anti-parallel magnetization period. Additionally, the MO beam deflector also has the unique abilities of active control at multi-gigahertz bandwidths and polarization selectivity of the deflected beam, where the odd and even diffraction orders have orthogonal polarizations.

The following sections outline the MO beam deflector and its basic operation. The first section describes its geometry, and the second models its operation and predicts its performance using the BPM-LL.

3.3.1 Geometry of the Magneto-Optic Beam Deflector

As outlined in section 2.4, when light passes through an MO sample with alternating magnetization, a diffraction output pattern is produced. The MO deflector under investigation is illustrated in figure 3.11, and is effectively a dynamically activated unit cell of the magnetic stripe domain diffraction grating discussed in section 2.4. Alternatively, one can consider it as two adjacent MO modulators with opposite Faraday rotations. The device consists of two 6.0 μm thick Bi-YIG films. The MO film Faraday rotation, absorption length, and refractive index (for both TE and TM) at the wavelength

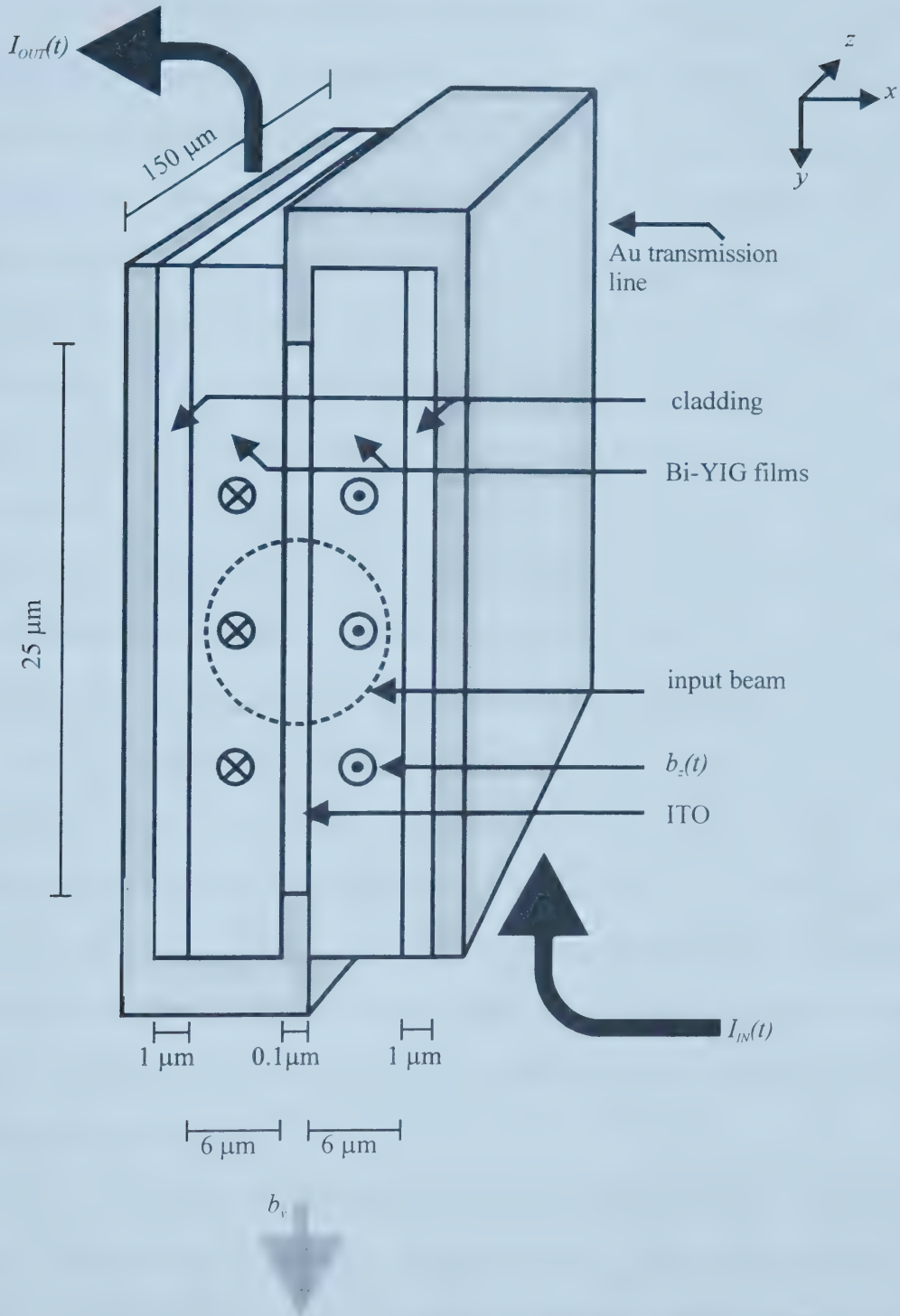


Figure 3.11. Schematic representation of a high-speed MO beam deflector. The proposed device is essentially a unit cell of the stripe diffraction grating depicted in figure 2.7.

of 1550 nm are 2500°/cm, 150 μm , and 2.3, respectively. The active region extends 25 μm in the transverse direction (y -direction) and, since optical attenuation is not directly included in the model, the device length (i.e. extent in the z -direction) is chosen to equal one propagation length. The two MO films are separated by a central layer of 0.1 μm thick indium-tin-oxide (ITO). The ITO layer has a refractive index of 1.96 (at 1550 nm) and a high transparency ($\sim 90\%$) at 1550 nm. This layer serves as part of the transmission line system used to propagate the high-speed current transients, $I_{in}(t)$ and $I_{out}(t)$. The relatively low resistivity value of $2 \times 10^{-6} \Omega \cdot \text{m}$ [10], high frequency response, and high optical transparency of ITO are well suited for this application. In order to confine the optical beam in the active MO region and to eliminate losses due to the outer gold transmission lines, 1.0 μm thick cladding layers of refractive index 1.94 are placed on the outermost surfaces of the MO films. Here, the 0.1 μm thick layers of gold are employed to serve, in conjunction with the central ITO layer, as the transmission line. With this serpentine transmission line configuration, the current transients in the transmission line run perpendicular to the z -direction such that the induced magnetic field is either parallel or anti-parallel to the z -direction, i.e. the direction of light propagation (the MO films will have the opposing magnetization directions required for diffraction to take place.) For the given dimensions of the active device Au/ITO transmission line, the total DC resistance is calculated to be $\sim 3.5 \Omega$.

For the serpentine transmission line used for the beam deflector, the magnetic field z -components of three independent transmission lines, as calculated in section 3.2.4, with 1 A anti-parallel currents are superposed and illustrated in figure 3.12. Although we consider the most general case of rectangular cross-section, the x -component of the

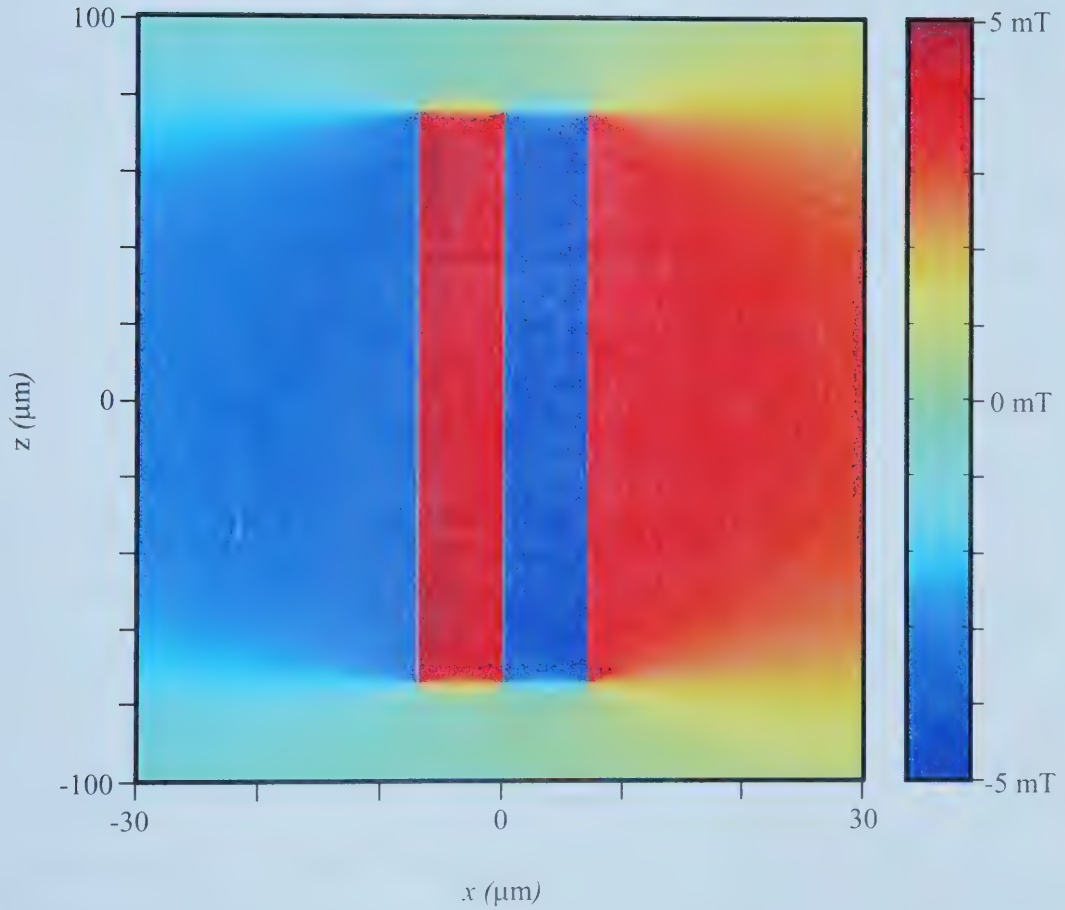


Figure 3.12. The distribution of the z -component of the magnetic field due to a single serpentine transmission line carrying a constant current of 1 A. For $d \gg l$, the magnetic field is uniform in the active region of the device.

magnetic field is small in the MO active region as $d \gg l$. Additionally, the fringing magnetic fields due to the transmission line interconnects/crossovers (located at the top and bottom of the schematic in figure 3.11) are negligible since they are far enough from the MO active region. Indeed, the magnetic field is quite uniform between the transmission lines, presenting an ideal situation for this problem as a homogenous magnetization is required to achieve well-defined phase fronts, and thus, high contrast deflection is expected.

As in the case of the MO modulator, the MO beam deflector also requires an external biasing DC magnetic field, since the magnetization must be switched into and out of the direction of optical propagation effectively. The transmission line system of the deflector serves to momentarily change the state of magnetization within the active region, as per the discussion in section 2.3. This was also the case for the MO modulator, and therefore, the overall time-dependent operation of the beam deflector is very similar. The magnetic field along the z direction is calculated at each mesh point and the resultant value is used in the LL model to evaluate the temporal evolution of the device.

3.3.2 Concept of Magneto-Optic Beam Deflection

As an initial test of the concept of the periodic magnetizations reversals and its effect on a propagating optical beam, time-independent simulations were performed on a single Bi-YIG film that has alternating magnetization in the direction of optical propagation. The geometry and experimental parameters are similar to those in [11] and the situation is depicted in figure 2.7. Here, the configuration is one in which the optical propagating beam travels perpendicular to the film plane. The magnetic stripe domains are aligned parallel and anti-

parallel to the direction of propagation and alternate in the transverse direction. The Bi-YIG film thickness, and thus the optical interaction length, is $20\text{ }\mu\text{m}$, and the Faraday rotation is $11000\text{ }^\circ/\text{cm}$ at 633 nm . The input optical beam has waist of $16\text{ }\mu\text{m}$, a wavelength of 633 nm , and is TE polarized. Figure 3.13 shows the diffraction orders for both TE and TM polarizations, resulting from a static phase grating with a domain spacing of $1.7\text{ }\mu\text{m}$. As indicated in the figure, the even diffraction orders have a polarization state that is the same as the input beam polarization (TE), and the odd diffraction orders have one that is orthogonal (TM). Moreover, the diffraction efficiency of the device is calculated to be 9%, which compares well with a typical experimental value of 5% [11].

3.3.3 Theoretical Modeling of the Proposed Magneto-Optic Beam Deflector

After verifying the concept of MO beam deflection in the previous section, the proposed MO beam deflector is now modeled. Figure 3.14 shows the time-independent spatial distribution of the TM beam inside and outside the device that has been proposed in figure 3.11, where a spatially uniform and static Faraday rotation throughout the MO films is considered. Unlike the case illustrated in figure 3.13, where the optical beam propagates perpendicular to one MO film, the proposed device channels the optical beam lengthwise along two films in a waveguide configuration. TE polarized light at 1550 nm with a $12\text{ }\mu\text{m}$ FWHM Gaussian beam profile is used to couple into the waveguides. Mode conversion occurs along the entire $150\text{ }\mu\text{m}$ length of the device until it reaches the end of the active MO region, upon which a near-field interference pattern emerges, later manifesting itself as diffraction orders in the far-field. The beam begins to diverge after leaving the waveguide region with a cone angle of $\sim 3^\circ$. For complete anti-parallel

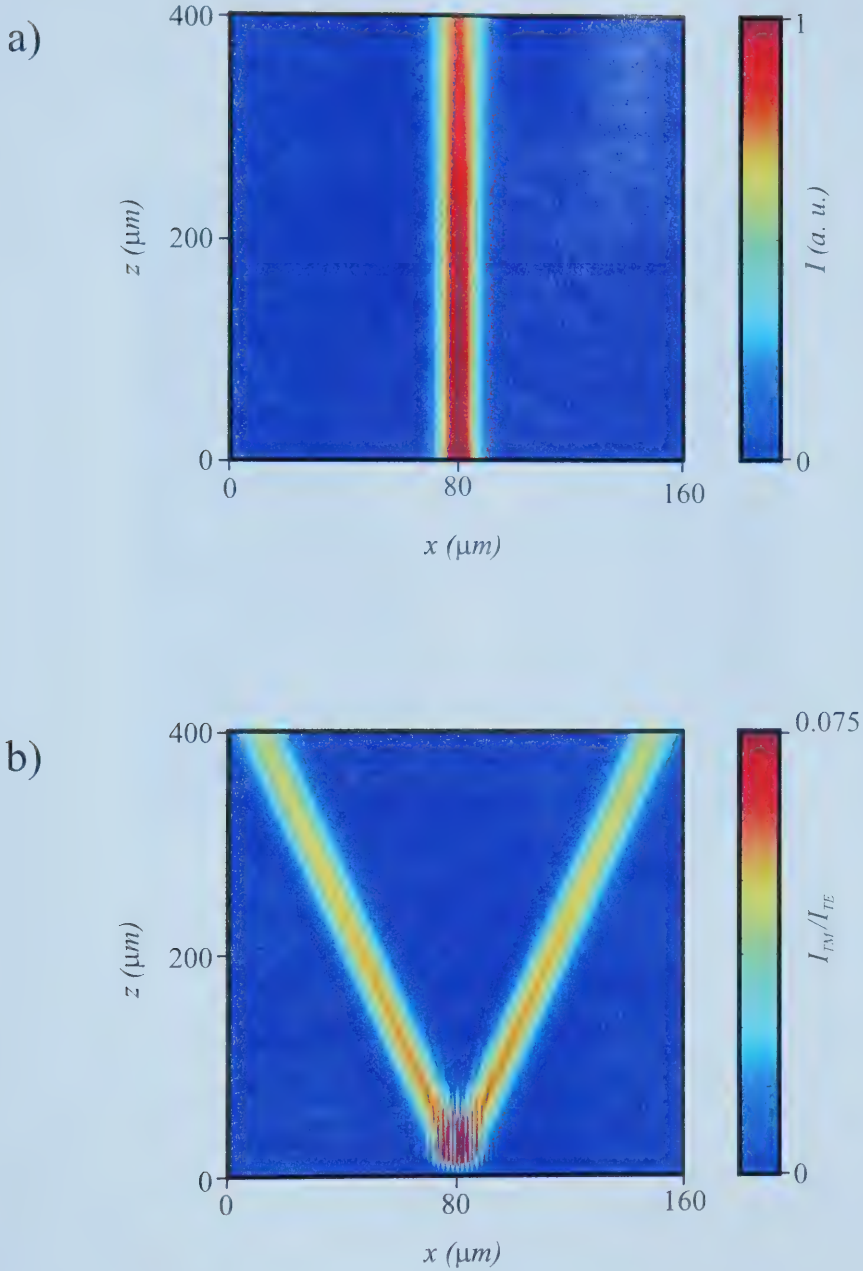


Figure 3.13. Diffraction pattern obtained with the time-independent BPM for a $20\text{ }\mu\text{m}$ thick stripe diffraction grating composed of alternating magnetizations for a wavelength of 633 nm , Faraday rotation of $11000\text{ }^\circ/\text{cm}$, and domain spacing $1.7\text{ }\mu\text{m}$. a) TE polarization, b) TM polarization.

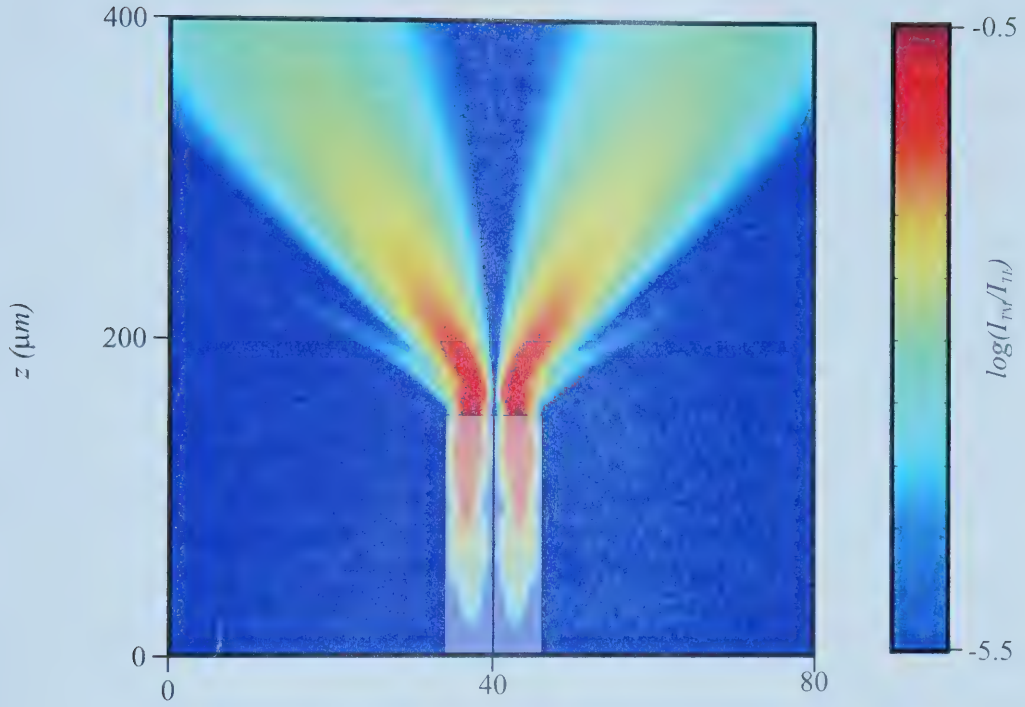


Figure 3.14. Time-independent deflected TM beam profile of the proposed MO beam deflector for a wavelength of 1550 nm and a Faraday rotation of 2500 %/cm. An outline indicating the boundaries of MO deflector is superimposed on the plot.

alignment of the magnetization, the conversion efficiency is calculated to be 31% (defined here to be the ratio of the amount energy in the TM mode to that of the input energy). Certainly, higher conversion efficiencies can be achieved using materials having a lower absorption coefficient

Upon establishing the diffraction effects due to static, opposing magnetization of the device, the next step is to include the effects of the magnetization dynamics through the Landau-Lifshitz equation. This will allow the realization of the high-speed performance and efficiency of this unique device. In evaluating the operation of the MO deflector, we consider a Gaussian electrical current transient traveling down the serpentine transmission line with a peak amplitude of 5 A and a FWHM of 1 ns [12], and the resulting magnetic field distribution is calculated using equation 3.2.5. The magnitude of the DC biasing magnetic field (27.5 mT) is chosen to maximize the signal amplitude while minimizing the amplitude of the resulting ferromagnetic precession (i.e. oscillations presents after the application of the pulse due to FMR). This ringing can be eliminated with the application of a higher biasing magnetic field, however, depending on the application at hand, this may not be necessary.

Figure 3.15 illustrates the Faraday rotation spatio-temporal distribution in response to the applied transient and static magnetic fields at $z = 75 \mu\text{m}$ (the center of the deflector). Near the edges of the transmission line there is slight enhancement of the Faraday rotation, however, the average Faraday rotation throughout one film is found to be 2000 %/cm (at the peak). This is about 20% lower than that achieved with complete anti-parallel alignment of the magnetization (2500 %/cm) and indicates that, at this applied

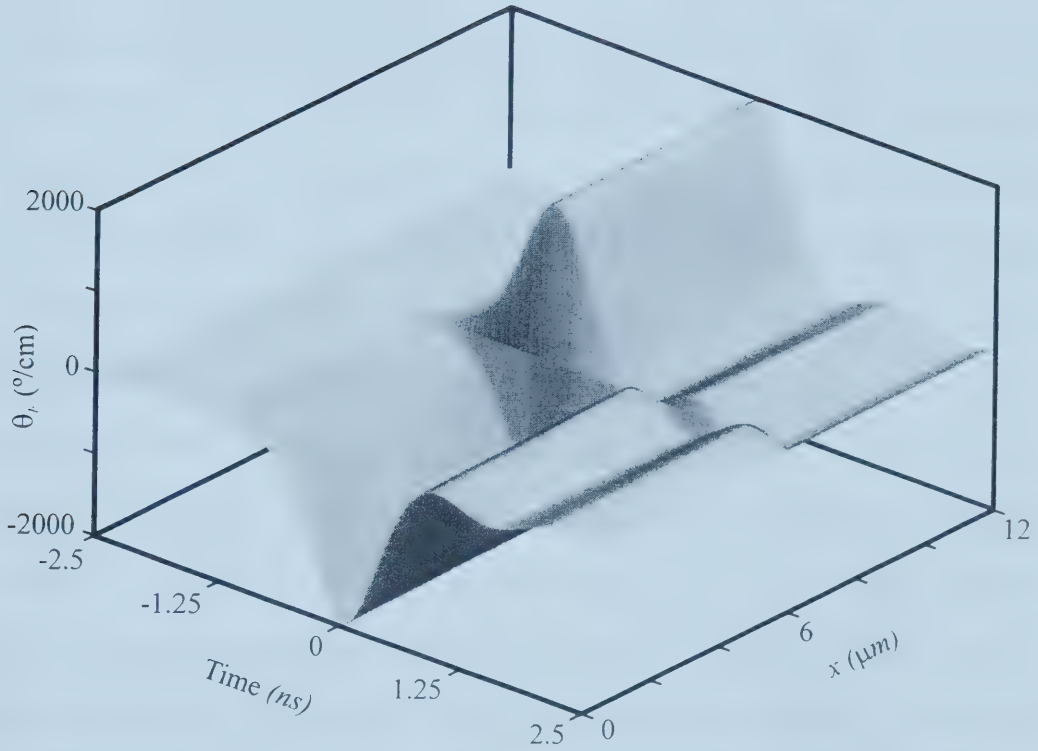


Figure 3.15. The spatio-temporal distribution of the Faraday rotation due to a current transient in the transmission line at $z=75 \mu\text{m}$. The small oscillations near the trailing edge of the pulse are due to the ferromagnetic precession of the magnetization.

transient current pulse, the magnetization is not totally aligned along the direction of propagation.

The spatio-temporal distribution of the Faraday rotation shown in figure 3.15 is now used to model the time-dependent operation of the MO deflector. Figure 3.16 shows six snap shots of the TM light inside and outside the MO deflector during its operation. The spatial images are taken at various times (-1.5 ns, -0.5 ns, -0.25 ns, 0 ns, 0.5 ns, 0.75 ns) in response to a 1 ns FWHM, 5 A (peak) Gaussian current pulse, which has its maximum centered at 0 ns. Overall, the diffraction pattern, polarization effects, and mode propagation resemble those of the static situation. The diffraction angle for the first order is measured to be $\sim 7^\circ$, which compares to 7.4° calculated from the diffraction grating equation 2.4.1. The deflected beam intensity rises with the onset of the electrical pulse, reaching its highest intensity at the peak of the 1 ns electrical current pulse and subsequently decreases to zero after the excitation passes. The calculated dynamical efficiency is 20% (or 67% relative to the static case). At a biasing DC magnetic field of 27.5 mT, relatively small intensity temporal oscillations ($< 1\%$ of the main signal) are observed after the initial pulse has passed. A more representative illustration of the high-speed operation of the deflector is depicted in figure 3.17, which shows the time dependent output of the device. Here, the oscillations (due to FMR) following the pulse are more clearly observed, and have a frequency of 0.77 GHz. Increasing the biasing field will eliminate these oscillations, but at the expense of signal amplitude.

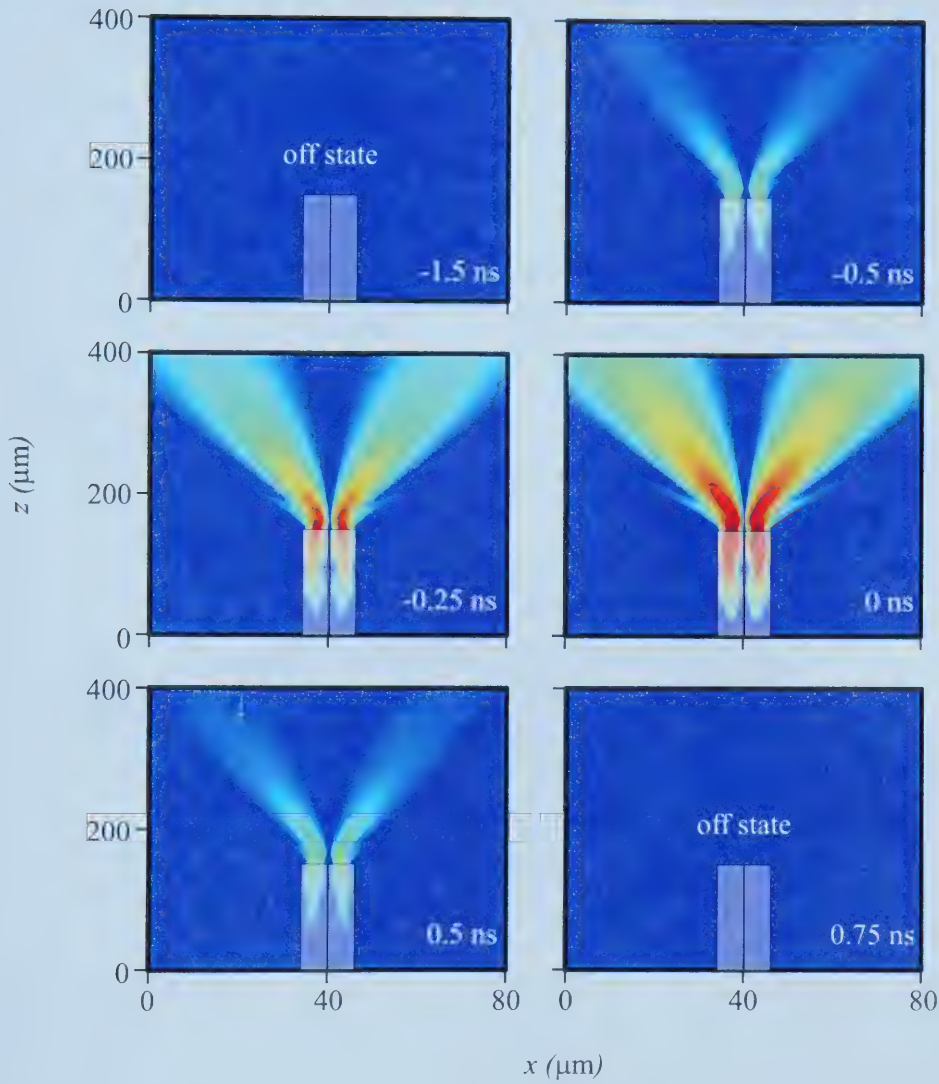


Figure 3.16. Spatial snap shots of the output of the MO beam deflector showing the mode conversion and a subsequent TM diffraction pattern for a wavelength of 1550 nm. The MO deflector is driven with a 1 ns FWHM, 5 A (peak) Gaussian current pulse. The maximum response occurs at the peak of the current pulse at $t = 0$ ns. An outline indicating the boundaries of MO deflector is superimposed on the plot.

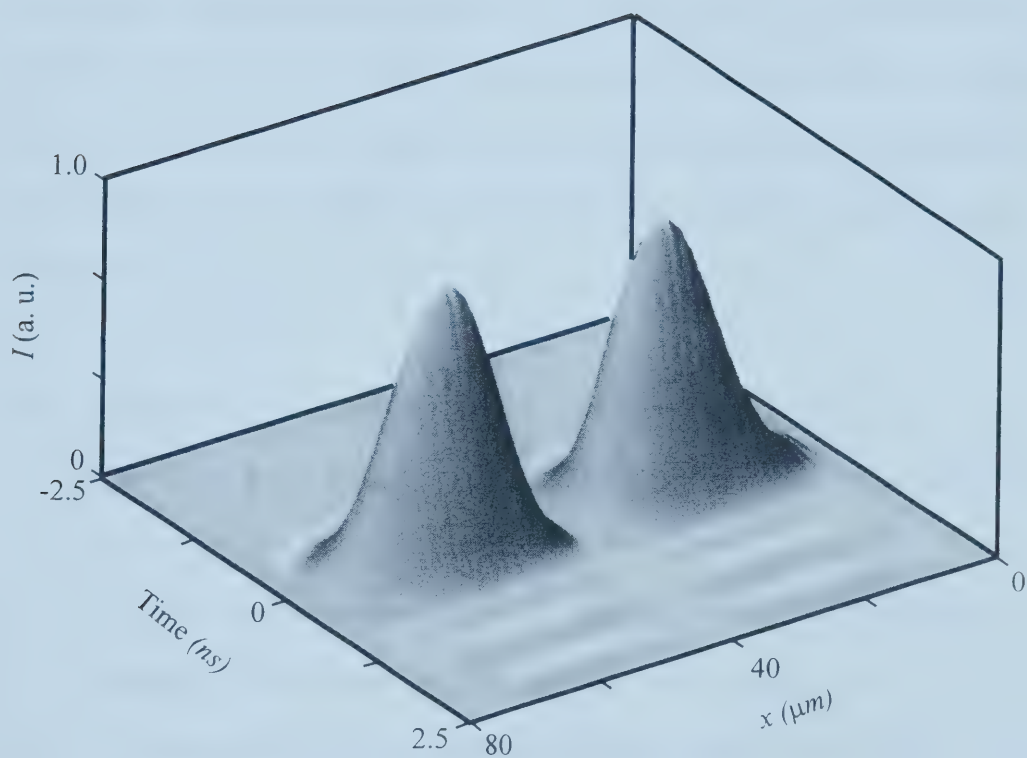


Figure 3.17. Far-field spatio-temporal output (TM polarization) of the MO deflector taken at $z=300 \mu\text{m}$ in response to a 1 ns current pulse.

3.4 Summary

Overall, a unique method, the BPM-LL, for modeling MO devices is derived and discussed in detail. The two processes of magnetization dynamics and light-wave propagation are included in the model, as these processes are fundamental in the modeling and understanding of MO effects. The BPM-LL is used to predict the operation and performance of the MO modulator, and following this, it is used in the proposal and modeling of a novel high-speed MO beam deflector. The analysis used here provides a practical framework for designing and optimizing MO applications and other magneto-phonic devices.

3.5 References

- [1] S. E. Irvine and A. Y. Elezzabi, "High-Speed Magneto-Optic Beam Deflection," *IEEE J. of Quantum Electron.*, (to appear October, 2002).
- [2] S. E. Irvine and A. Y. Elezzabi, "Multi-Gigahertz Guided Wave Magneto-Optic Modulator," *IEEE Photon. Technol. Lett.*, vol. 14, pp. 798-800, 2002.
- [3] A. Erdmann and P. Hertel, "Beam-Propagation in Magneto-optic Waveguides," *IEEE J. Quantum Electron.*, vol. 31, pp. 1510-1516, 1995.
- [4] P. Lorrain, D. R. Corson, and F. Lorrain, *Electromagnetic Fields and Waves*, 3rd Ed. New York: W H. Freeman and Company, 1987, pp. 630.
- [5] S. C. Chapra and R. P. Canale, *Numerical Methods for Engineers*. New York: McGraw-Hill, pp. 742-744, 1988.

- [6] W. H. Press, S. A. Teukolsky, W. T. Vetterling, and B. P. Flannery, *Numerical Recipes in C*. New York: Cambridge University Press, pp. 850, 1988.
- [7] D. I. Steinberg, *Computational Matrix Algebra*. New York: McGraw-Hill, pp. 103-112, 1974.
- [8] A. Yariv, "Coupled-Mode Theory for Guided-Wave Optics," *IEEE J. of Quantum Electron.*, vol. QE-9, pp. 919-933, 1973.
- [9] R. Wolfe, V. J. Fratello, and M. McGlachan-Powell, "Thin-film garnet materials with zero linear birefringence for magneto-optic waveguide devices," *J. Appl. Phys.*, vol. 63, pp. 3099-3103, 1988.
- [10] S. A. Bashar, Ph.D. thesis, Department of Electronic Engineering, University of London, 1998
- [11] G. F. Sauter, R. W. Honebrink, and J. A. Krawczak, "Alterable grating fiber-optic switch," *Appl. Opt.*, vol. 20, pp.3566-3572, 1981.
- [12] B. O'Meara, Moose Hill Enterprises Inc., private communication.

Chapter 4

Experimental Set-up and Results

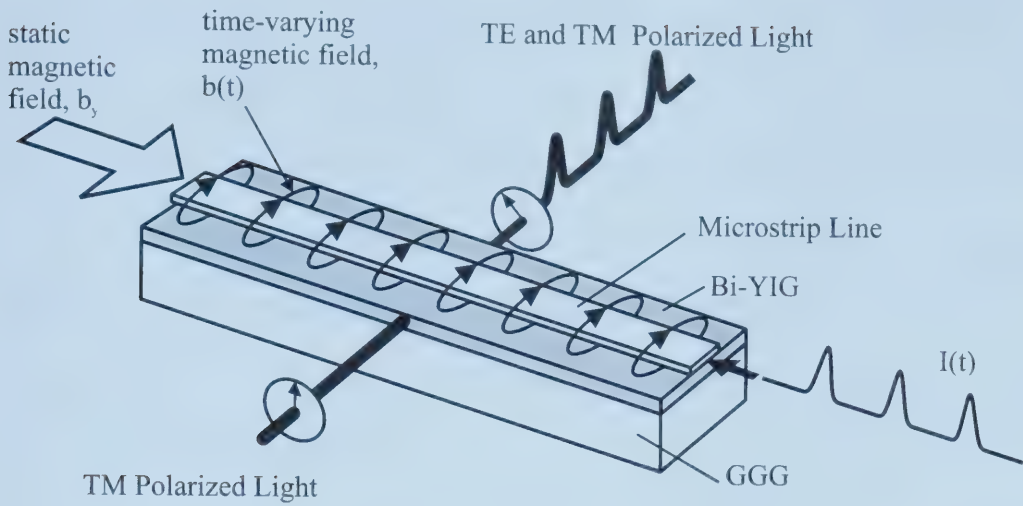
In this chapter, the experimental details of MO modulation are addressed. The construction of an MO modulator is described in detail as is the experimental arrangement used to test and characterize the device. This is followed by a discussion of the experimental results regarding high bandwidth light modulation. First, the resonant mode of operation is discussed, as these results highlight the frequency response of the device. Next, the non-resonant operational mode results are presented, which detail the broadband capabilities of the MO modulator. Finally, the MO modulator is operated at frequencies approaching the limits of the experimental detection arrangement and RF driving circuitry, revealing the possibility of sub-nanosecond optical modulation utilizing the MO effect.

4.1 Experimental Set-up for Magneto-Optic Modulation

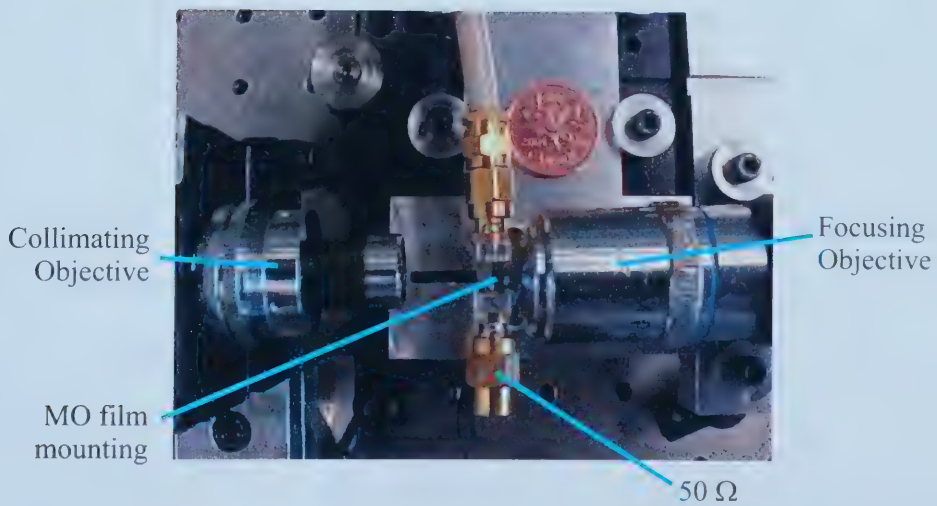
The first section describes the layout of the MO modulator and its important features and dimensions, and the second describes the experimental arrangement and components used to test the modulator.

4.1.1 The Magneto-Optic Modulator

A schematic representation of the device used for MO modulation is shown in figure 4.1a and an actual picture is shown in figure 4.1b. The MO active layer is a 4.5 μm thick



a)



b)

Figure 4.1. a) Schematic diagram of the MO modulator. b) Picture of the MO modulator and surrounding set-up.

(Y_{0.6}Bi_{0.4}LuPr)₃(FeGa)₅O₁₂ film that has been grown on a 450 µm thick (111)-oriented gadolinium gallium garnet (GGG) substrate by means of liquid-phase epitaxy (LPE). The saturation magnetization ($\mu_0 M_s$), specific Faraday rotation (θ_F), and absorption (α) of the film were measured to be 9 mT ($4\pi M_s=90\text{G}$), $\sim 5400^\circ/\text{cm}$, and 400 cm^{-1} , respectively; the latter two of which were measured at a wavelength of 800 nm. As the optical penetration depth, $1/\alpha$, is 25 µm, the length of the device should be on the order of this value for optimal efficiency. Scott and Lacklison [1] have derived the optimal interaction length for an MO modulator, which is given by

$$\frac{1}{2\theta_F} \arctan\left(\frac{2\theta_F}{\alpha}\right). \quad (4.1.1)$$

Using the values listed above for a wavelength of 800 nm, the calculated optical length is 23.4 µm. However, the length of the device was designed to be $\sim 60\text{ }\mu\text{m}$, which was the shortest length achievable with the mechanical polishing process employed.

4.1.2 Fabrication

This section briefly outlines the fabrication procedures for the MO modulator. The construction of the MO modulator involves polishing an MO crystal sample of Bi-YIG to the prescribed thickness of $\sim 60\text{ }\mu\text{m}$ and mounting the polished sample so that it can be manipulated in the experiment.

To thin and polish the sections of MO film a Buehler Ecomet polishing unit was used. Samples to be thinned or polished were held in contact with a spinning brass wheel upon which diamond embedded polishing pads were placed. The grit sizes on the abrasive surfaces used were varied from 30 µm to 0.1 µm to achieve an optical finish at a

desired thickness. This method was performed on both sides of a sample since both faces of the waveguide are required for light coupling/decoupling. Usually before polishing the second side, the sample was mounted on a glass plate to make handling and processing easier once the final thinning was complete (as the thinned sample is very fragile and brittle). After a reasonably polished sample was obtained, it was mounted in an aluminum carrier that protected the sample and brought external electrical connection to it.

4.1.3 The Transmission Line

Prior to thinning and polishing of the sample, a 100 nm thick layer of titanium film was deposited over the MO film to act as an adhesion layer for a 300 nm thick gold transmission line. However, the gold line did not adhere to the titanium properly, and therefore, was replaced with an indium transmission line of $\sim 100 \mu\text{m}$ thickness. Two SMA connectors, held in place by the aluminum casing, were bonded to both ends of the indium transmission line to allow for connection to external signal sources.

4.1.4 Driving Electronics

Electrical driving signals are fed into the device through one of the SMA connectors while the other SMA connector was terminated with a 50Ω load. Single frequency or pulsed electrical sources were utilized to demonstrate the two operational modes of the device: the resonant mode and the non-resonant (or broadband mode). The single frequency RF oscillator used for resonant operation was a Rhode & Schwarz signal generator (model SMT 03 1039.2000.03) with a frequency range of 9 kHz to 3 GHz (maximum voltage output of $3.7 V_{pp}$). Non-resonant, or broadband modulation was

demonstrated using a Stanford Research Systems model DG-535 Digital Delay/Pulse generator. Without modifying the output of the DG-535, the shortest electrical pulse available was a Gaussian-like pulse with an approximate full width at half maximum (FWHM) of 2.3 ns and an amplitude of 0.9 V. However, the pulse unit is equipped with a high-voltage step outputs (up to +35 V, and a 80 ns rise-time) and an additional step-recovery diode module that can be used to achieve fast rise-times of approximately 170 ps. Using suitable RC circuitry, this step can be differentiated to produce a very short electrical pulse that can then be used to test the MO modulator. To accomplish this, the circuit depicted in figure 4.2 was used [2].

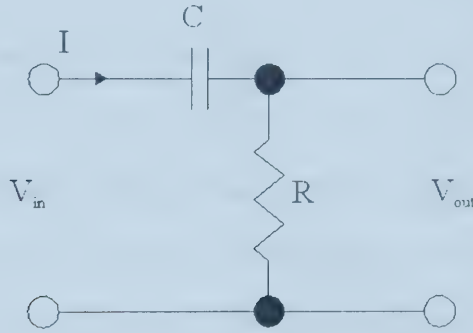


Figure 4.2. Circuit used to differentiate 35 V steps to produce pulses.

By considering a general case, with arbitrary values of I , R , C , V_{in} , and V_{out} as in the circuit diagram. The voltage drop across the resistor is given by

$$V_{out} = IR \quad (4.1.2)$$

and is related to the voltage drop across the capacitor through the current:

$$I = \frac{dQ}{dt} = C \frac{dV_c}{dt} \quad (4.1.2)$$

where V_c is the voltage drop across the capacitor. If the voltage drop across the resistor is small compared to that across the capacitor, then V_c in equation (4.1.2) becomes V_{in} , and the output voltage can be written as

$$V_{out} = RC \frac{dV_{in}}{dt} \quad (4.1.3)$$

The value of capacitance used here was 10 pF, and the resistance is the 50 Ω load on the sample. Using this simple circuit in conjunction with the 35 V step outputs of the pulse unit, the electrical pulse shown in figure 4.19 is generated.

4.1.5 The Lasers

For the optical input, an 800 nm Ti:Sapphire continuous-wave (CW) laser was initially used as the optical input for the MO modulator. However, this laser had a cumbersome start-up procedure (typically requiring 1 hour of warm up time) and its output was also unstable since its cavity is designed for the generation of 10 fs pulses (and not CW output). As a result, the Ti:Sapphire laser was replaced with an 800 nm 100 mW CW laser diode (World Star Technologies.). This diode laser is compact, easier to “turn-on”, and is much more stable than the Ti:Sapphire laser.

4.1.6 The Optical Arrangement and Test Set-Up

The experimental set-up depicted in figure 4.3 was used to test and characterize the device. The light emitted from the laser diode is directed through a polarizer, thus ensuring that the beam has a well-defined linear polarization that can be used for input to the MO modulator. A microscope objective (60x and a focal length of 4 mm) couples this light into the MO film waveguide, where it propagates and accumulates a polarization

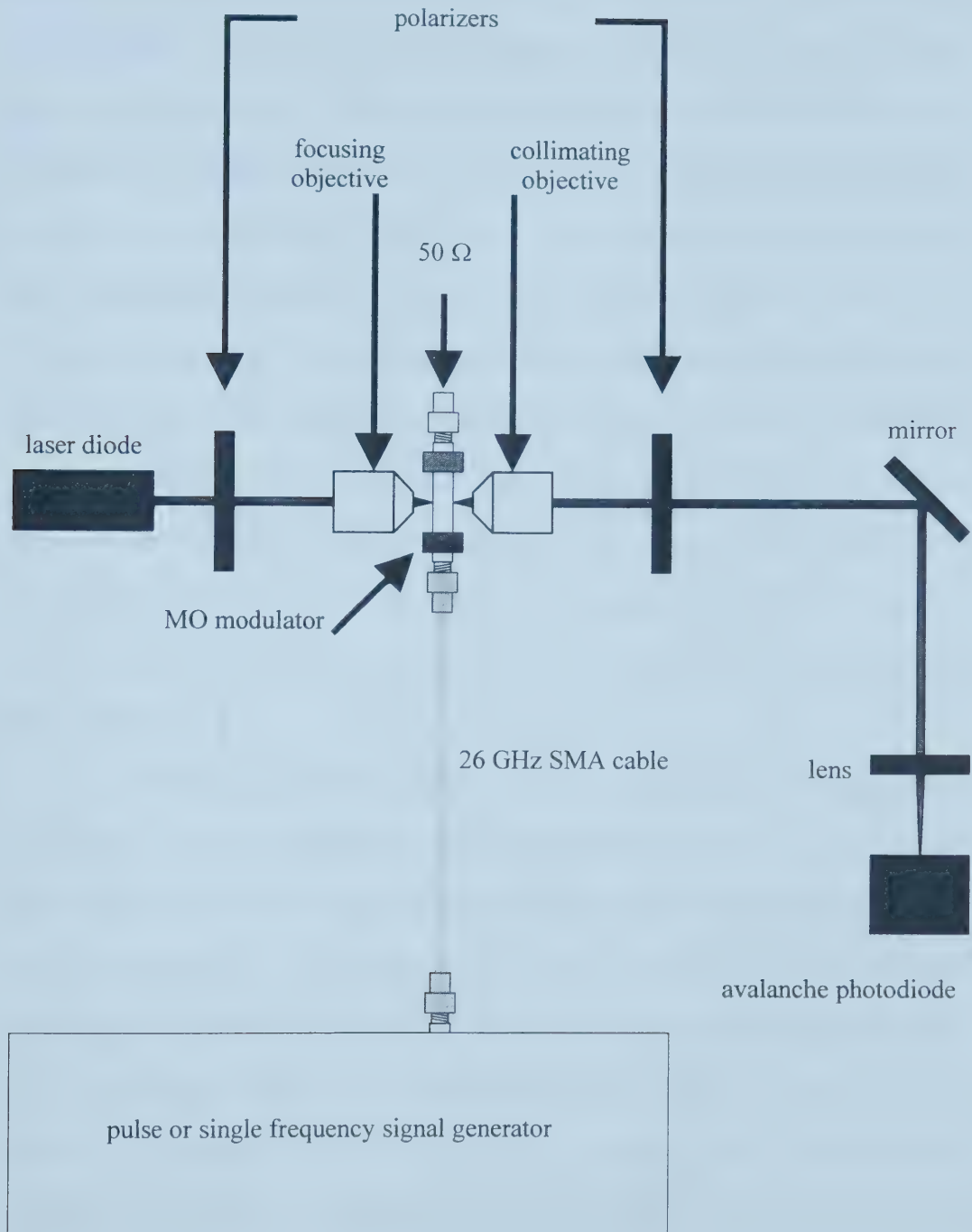


Figure 4.3. Experimental setup used to test the MO modulator.

rotation (according to the state of the magnetization of the Bi-YIG film). The output from the waveguide is collimated with a second objective (5x and a focal length of 1.5 cm), and the resultant beam is then directed through another polarizer to convert the polarization modulation (acquired from the MO film) into an intensity modulation. This modulated light is reflected off a single mirror and focused through a lens onto a high-speed photodiode/transimpedance amplifier (data sheet and mounting procedure are presented in Appendix C). The electrical output of the photoreceiver is connected to a Tektronix CSA8000 Communications Signal Analyzer, which is equipped with an 80E03 sampling module having 2 channels and a bandwidth of 20 GHz (the rise-time of each channel is less than 17.5 ps). This signal analyzer is used to capture digital images of both the optical and electrical waveforms used in this experiment. As well, it is used to measure several aspects of the various signals (i.e peak-to-peak amplitude, rise-time, pulse duration, etc.).

An alternative experimental set-up, in which balanced detection was employed, was initially used to test the MO modulator. The balanced detection set-up is very similar to the single-detector set-up except the second polarizer is replaced with a quarter-wave plate and followed by a Wollaston prism as shown in figure 4.4. This prism splits incoming linearly polarized light into two beams having orthogonal polarizations (the polarization axes are defined by the orientation of the prism). These two beams were then sent off to a balanced detector module, which consisted of two photodiodes and accompanying circuitry that subtracted the individual signals from the two diodes (the schematic is discussed in Appendix C). The output from each photodiode must be equal in magnitude before subtraction and is balanced accordingly using the quarter-wave plate.

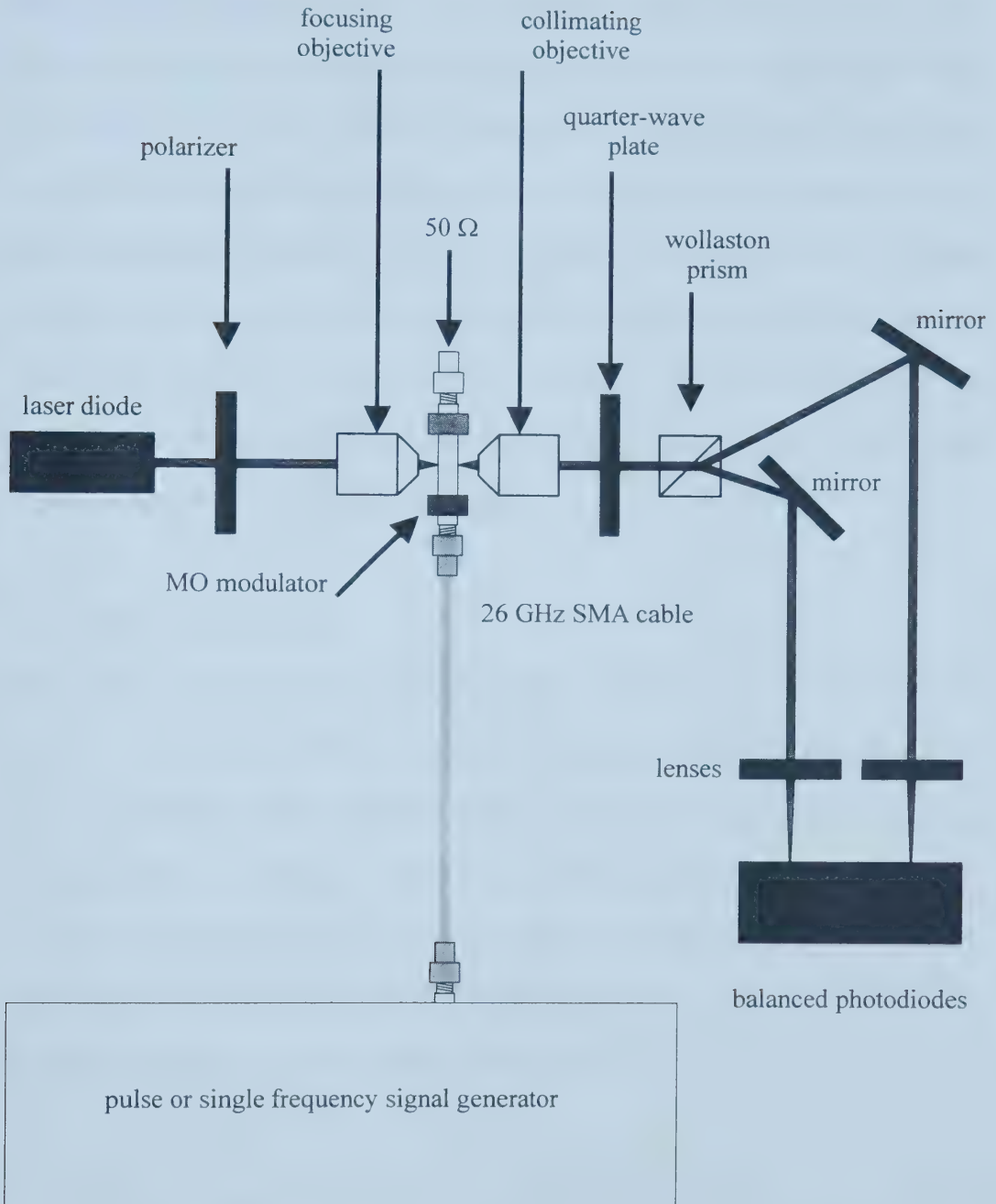


Figure 4.4. Alternative experimental set-up employing balanced detection.

Once aligned and properly balanced, such a system offers a higher signal-to-noise ratio than a single detector, which can be explained as follows. If the polarization of the optical beam before the Wollaston prism undergoes Faraday rotation, the intensity falling on one detector is increased while the intensity on the other is decreased. When the two are subtracted, the overall resultant change in signal is twice as much experienced by a single detector, and common mode noise, such as laser noise will be canceled using this configuration. However, even with these advantages, the signal strength was small and required an additional low-noise amplifier integrated with the diode circuit. This configuration was abandoned for a much simpler design involving a single ended avalanche photodetector/amplifier arrangement.

4.1.7 Static Magnetic Field

For the biasing field, a rectangular magnet is placed in close proximity to the MO sample near the 50 Ω terminator. Here, a samarium cobalt permanent magnet (surface field of 0.35 T) is utilized to apply the static in-plane magnetic fields along the y -direction, and its distance from the sample is varied to adjust magnitude of the magnetic field. To measure the field strengths used to bias the sample, a magnetic field sensor (LakeShore model 410 Gaussmeter) was employed and placed in close proximity to the device near the exiting light to give the most accurate measurement.

4.1.8 Optical Alignment

Before electrical signals were applied to MO modulator, it was ensured that the input beam was properly guided through the optical system. Careful attention was given to beam height and directionality throughout the test apparatus. Most importantly, it must be ensured that optical beam is traversing the MO waveguide and not the GGG substrate. When properly coupled to this waveguide, a small spot can be observed after the MO film, corresponding to the output of the waveguide. By sweeping a permanent magnet back and forth near the sample, an intensity variation could be observed after the second polarizer that was correlated with the motion of the magnet. This modulation verified the fact that optical beam was coupled through the MO film, and that the spot was indeed the output of the waveguide. Furthermore, if the position of the sample was moved slightly in either of the directions perpendicular to the film, the spot vanished and fringes were observed, which are a result of the near field image of the film edges. These facts proved useful in the alignment of the optical beam as it passed through the MO crystal.

After a preliminary optical alignment of the MO modulator and the test system, electrical signals were applied to the device to optimize the set-up further (as the signal amplitude could be directly monitored as components were adjusted). For this optimization procedure, the single frequency source (Rhode & Schwarz signal generator) was used to drive the MO modulator instead of the pulse source. This was beneficial for two principal reasons. First, the resonant mode of operation has much higher optical signal amplitudes than the non-resonant mode, and therefore, the optical signal is much easier to resolve. The second reason is that, unlike pulses, sine waves do not require additional timing synchronization, thus making the electrical sampling much easier. The

input sine wave frequency was set to 750 MHz with an amplitude of 3.7 V_{pp} (corresponding to the maximum output of the signal generator) and the output signal from the photoreceiver was monitored as various positions of various components were changed, including the DC magnetic field, until the signal amplitude was maximized (continued over several iterations if necessary). Since the biasing magnetic field parameter was included in the optimization process, it was adjusted to give maximum response (which occurs at the FMR frequency), and therefore, the system is operating at resonance.

4.2 Experimental Discussion and Results

As mentioned previously, the device has two operational modes, a resonant mode and a non-resonant (or broadband mode.) The first section describes experimental results of the resonant behavior of the device and characterizes its frequency response, while the second section illustrates results pertaining to the broadband capabilities of the MO modulator. Both sections outline the effects of the static magnetic field, and both sections emphasize its integral contribution to the device operation as well as the complexity of the underlying magnetization dynamics. Finally, the third section describes an experiment used to measure the modulation efficiency of the MO modulator at low frequency.

4.2.1 Resonant Mode

Resonant modulation is achieved by driving the modulator at its FMR frequency. Figure 4.5 illustrates the resonant output of the MO modulator for several frequencies. At each frequency, the static magnetic field was adjusted to ensure a resonance condition. In each

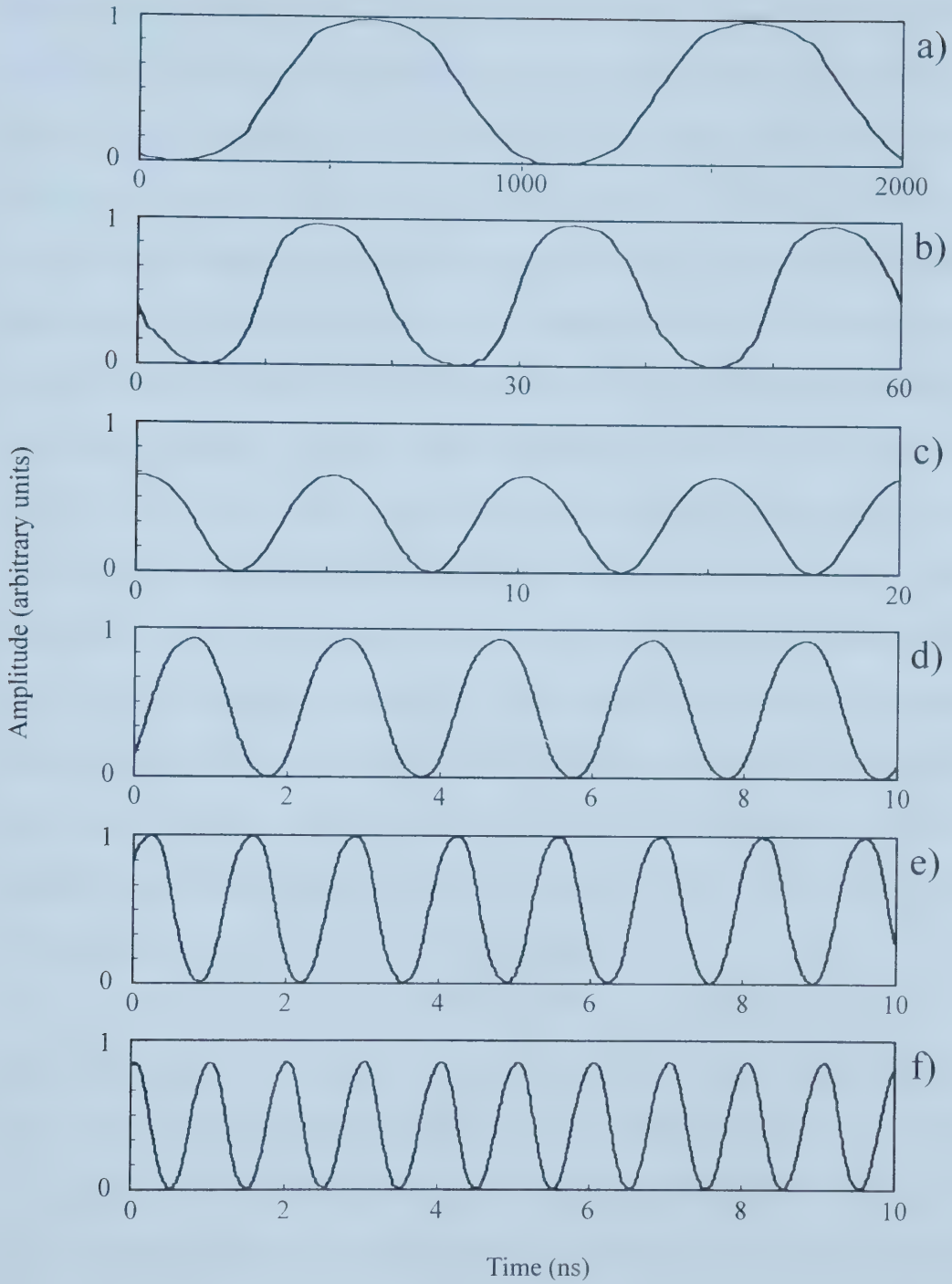


Figure 4.5. Resonant output of the MO modulator for various driving signals at frequencies: (a) 1 MHz, (b) 50 MHz, (c) 200 MHz, (d) 500 MHz, (e) 750 MHz, and (f) 1 GHz. The corresponding biasing field strengths are measured to be (a) 6 mT, (b) 6.5 mT, (c) 8.5 mT, (d) 8 mT, (e) 14 mT, and (f) 20 mT.

case, the RF drive voltage is set to 3.7 V_{pp}, corresponding to a low average drive power of 34 mW in a 50 Ω load. The considerable range of operating frequencies demonstrates the large range of tunability that can be achieved using the inherent FMR of the device. The output sine waves are well defined, and the amplitudes are nearly constant. As observed, the resonance at 200 MHz has an amplitude that is $\sim 20\%$ less than the other frequencies. This is attributed to an incomplete magnetization of the BI-YIG sample, and the details of this are addressed in the related discussion below regarding figure 4.7. It is also observed in figure 4.5 that the 1 GHz amplitude is also reduced by $\sim 20\%$ relative to the 1 MHz case. This is not a result of the magnetization of the sample; rather, it is attributed to a known impedance mismatch in the RF circuit between the transmission line structure of the MO modulator and the SMA components (i.e. SMA cable and 50 Ω terminator). The impedance mismatch of the MO modulator transmission line structure was measured, and the transmission coefficient, defined to be the ratio of the input and output signal amplitudes, is plotted in figure 4.6 as a function of frequency. At 1 GHz, the transmission coefficient is reduced to 80% of its value at 1 MHz. This can be corrected with a proper ground plane and better RF circuit design.

To characterize the dependence of the FMR frequency on the applied biasing field, several operational frequencies are chosen and optimized, and the biasing magnetic field strength is measured. Figure 4.7 illustrates a plot of the FMR frequency, ranging from 1 MHz to 1.1 GHz, versus the applied biasing magnetic field. For frequencies between 400 MHz and 1.1 GHz, the experimental data exhibits a linear relationship of the FMR on biasing field strength with a slope of 42 GHz/T. For comparison, a curve of the FMR frequencies calculated from Kittel's relation, for a ferromagnetic film sample, is

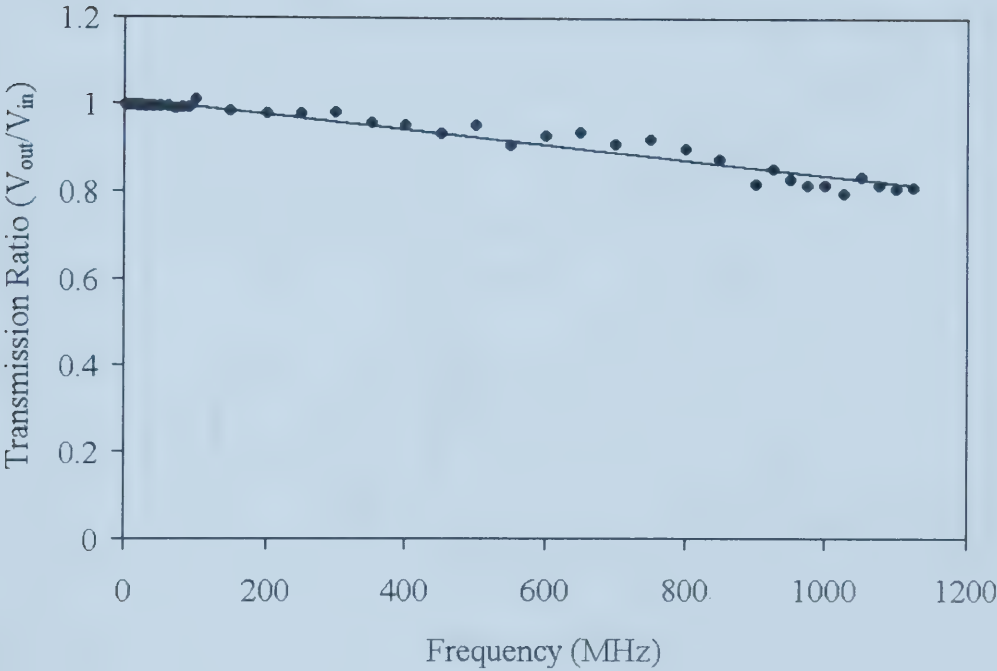


Figure 4.6. Impedance matching characteristics of the MO modulator.

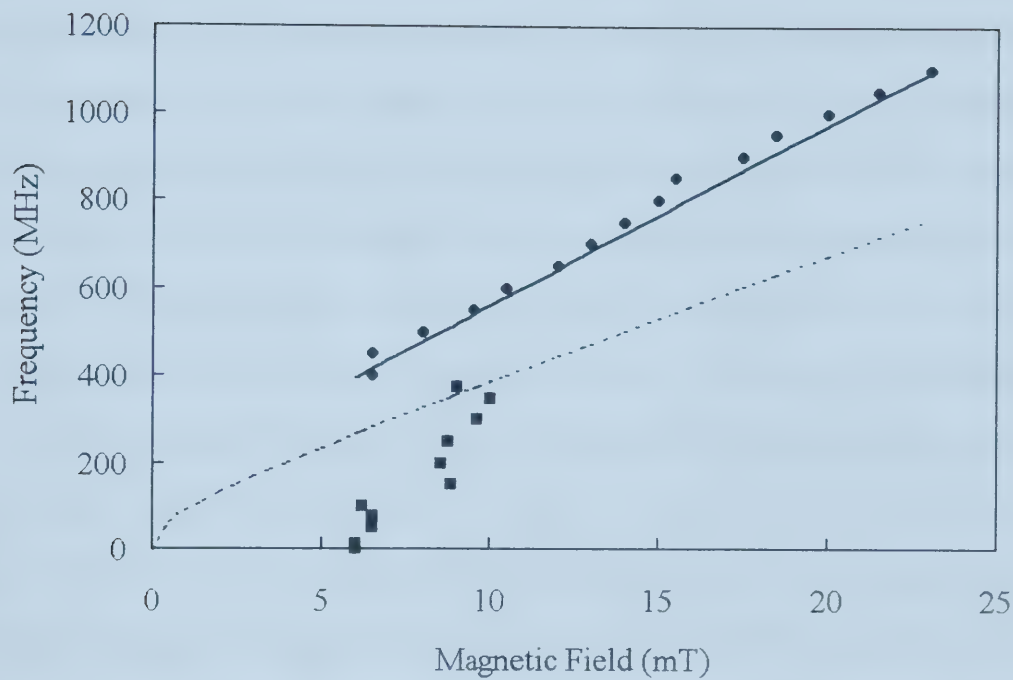


Figure 4.7. FMR frequency as a function of applied biasing magnetic field. Experimental values (circles and squares) and calculated values from Kittel's relation (dashed line) are shown. For frequencies below 400 MHz (squares), the experimental data does not follow any obvious relation.

shown on the same plot. It should be noted that Kittel's relation is derived assuming uniform precession of the magnetization. In the linear regime of Kittel's relation ($b_y > \mu_0 M_s$), the slope of the theoretical curve is 28 GHz/T ($=ge/4\pi m$, with $g=2.0$), which is a factor of 1.5 lower than the experimentally determined value. Previous experiments [3,4], with a uniform driving field and non-resonantly driven out-of-plane magnetization, showed excellent agreement between the experimental and the calculated slopes ($g=2$). In these experiments, the maximum frequencies used were up to two orders of magnitude larger, and thus, much higher biasing field strengths were necessary. It is conceivable that the magnetic field strengths used in these experiments do not overcome internal fields of the sample, resulting in a precessional frequency value that is different from the value predicted by Kittel's relation. Also, a non-uniform RF magnetic field is known to produce a non-uniform precession of the magnetization at a frequency that differs from that predicted by Kittel's relation [5]. In this experiment RF field inhomogeneity arises from the irregularities in the shape of the indium transmission line. Nonetheless, the general trend of a linear dependence of FMR frequency on the static magnetic field strength is apparent for higher frequencies (greater than 400 MHz), and the device performs as it should, simply with a lower than expected value for the static magnetic field. However, this is not the case for frequencies below 400 MHz, as the behavior of the FMR frequency with biasing field strength does not follow any obvious relation. In this region the field values required for resonance are extremely small and most likely do not fully align the magnetization along the applied field direction. This incomplete magnetization allows domain walls to form, and hence, adds complexity to the system. As Kittel's relation is derived under ideal conditions of uniform magnetization and does

not take into account inhomogeneously magnetized samples or domain wall motion, the deviation from the theoretically calculated values is expected at low frequency.

The resonance condition of the device can be verified by sweeping the input frequency over a wide range. To map the frequency characteristics of the MO modulator for a given biasing field after resonance operation has been achieved, the driving frequency is varied between 1 MHz to 1.2 GHz while the amplitude of the optical signal is recorded at each frequency step. During this process of frequency scanning, the static magnetic field was not changed since the resonance conditions would change. This experiment was performed for three individual FMR frequencies of 500 MHz, 750 MHz, and 1 GHz with biasing field strengths of 8, 14, and 20 mT, respectively. The results, shown in figure 4.8, reveal the same overall behavior for each curve, peaking at the selected resonance frequency. Of interest is the relatively flat response below the peak resonance. For the 500 MHz, 750 MHz, and 1 GHz FMR frequencies, these levels correspond to 33%, 21%, and 14% of the resonance peak amplitude, respectively. This offers the possibility of operating the MO modulator below its FMR frequency at the cost of lower signal amplitude but with the advantage of a much higher bandwidth. As demonstrated in section 4.2.2, this feature is essential for pulsed data streams, where a large and nearly uniform bandwidth is required.

Interestingly, it can be seen in figure 4.8 that the width of the resonance peaks vary with applied field. As the biasing magnetic field is increased, the FWHM of the resonance curves decrease, from 223 MHz (for the 500 MHz resonance) to 47 MHz (for the 1 GHz resonance), indicating the presence of a damping mechanism that appears to depend on the biasing magnetic field strength. Additionally, a broad peak slightly below

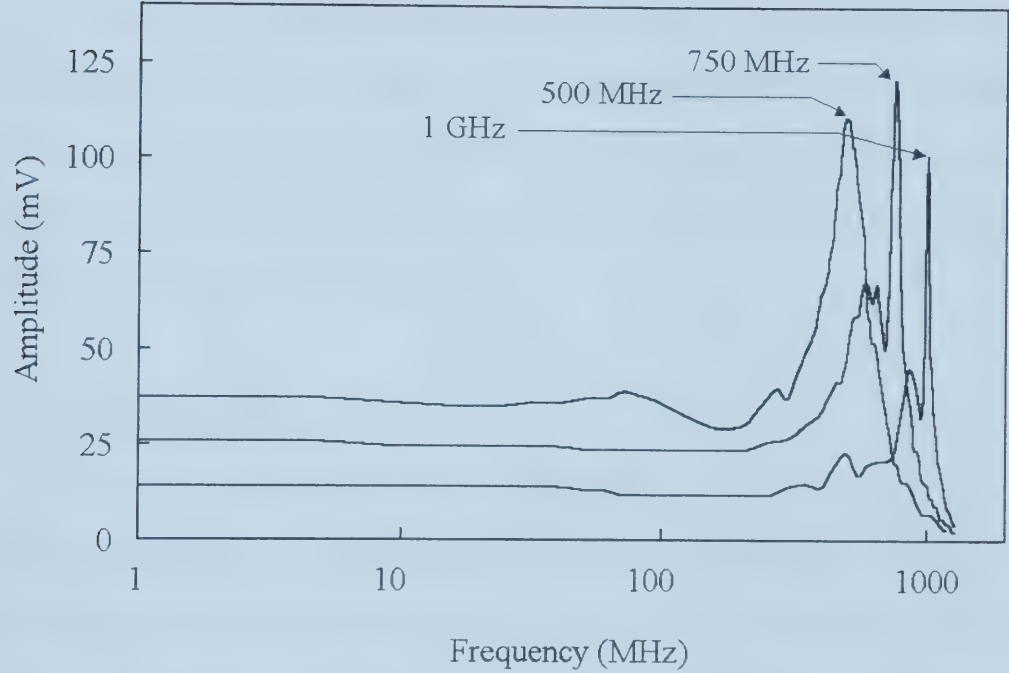


Figure 4.8. The frequency response of the MO modulator for three individual FMR frequencies of 500 MHz, 750 MHz, and 1 GHz with biasing field strengths of 8, 14, and 20 mT, respectively.

the resonance peak is observed in the 750 MHz and 1 GHz curves. This anomalous peak occurs at 600 MHz for the 750 MHz FMR, and at 850 MHz for the 1 GHz FMR. These features are due to the excitation of spin-waves modes in the Bi-YIG. An inhomogeneous RF magnetic field is known to enhance this coupling mechanism [5], and, as addressed in the discussion of figure 4.7, the RF field produced by the indium transmission line is expected to be quite non-uniform.

It should be noted that resonance operation at 1.8 GHz was achieved using a static field strength of 45 mT, and the output of the device at this frequency is shown in figure 4.9. However, the frequency characteristics of the MO modulator could not be mapped, as the flat response level of the frequency sweep curve for this biasing field was too small to be measured using the current system.

4.2.2 Non-resonant Mode

As was previously shown, the frequency characteristics of the MO device show a relatively flat response over a large frequency range before the FMR peak. This feature is used to demonstrate pulsed mode operation of the device, which for example, is important for fiber optic communications. Figures 4.10-4.15 show the measured output of the MO modulator for several driving electrical pulses of varying shape and pulse duration, along with their static magnetic field strengths. The measured optical pulses are well represented and the pulse durations are maintained as the device maps the electrical input onto the optical carrier. For the slower square pulses, with duration more than 200 ns, distinct capacitor-like charging effects are observed in the optical trace, which slightly distort the pulse from its unipolar shape and towards a bipolar shape. This is an artifact

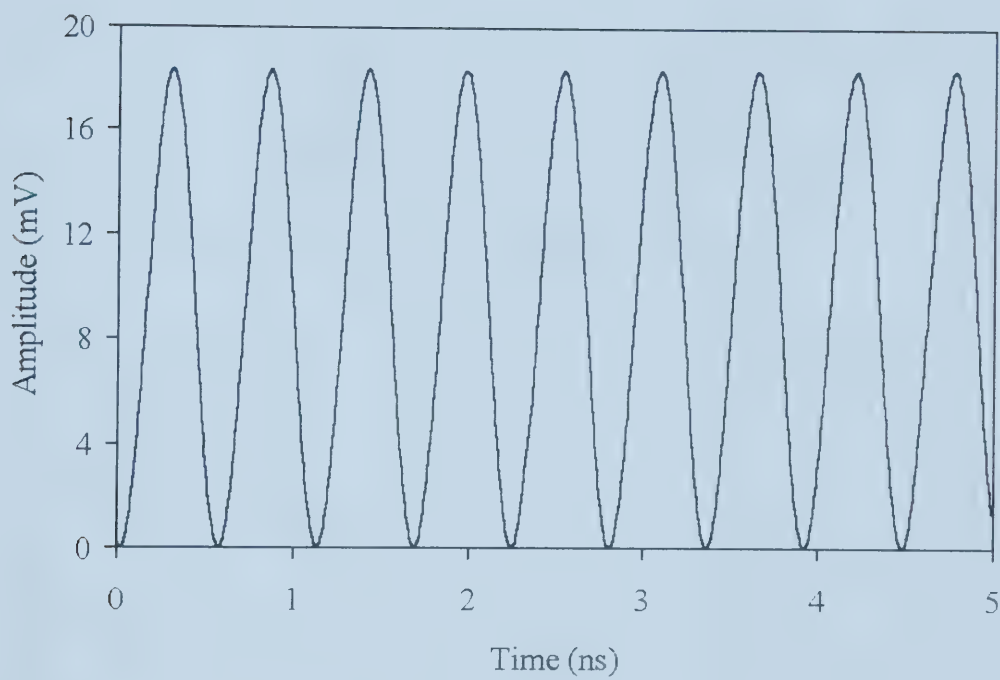


Figure 4.9. Single frequency modulation at 1.8 GHz.

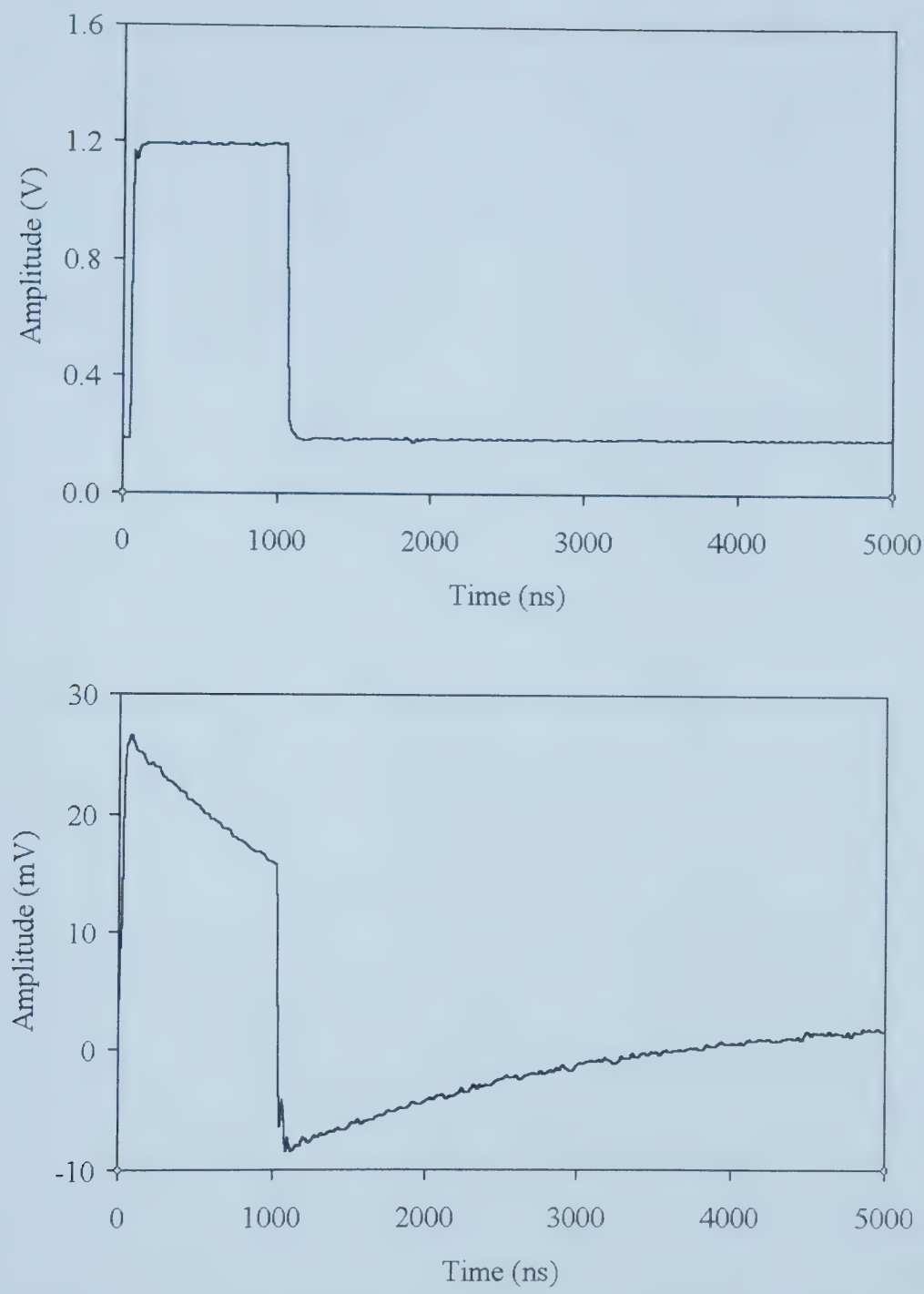


Figure 4.10. Pulse width: 1000 ns. Driving electrical pulse (top) and measured optical pulse (bottom). $b_y=6.8$ mT.

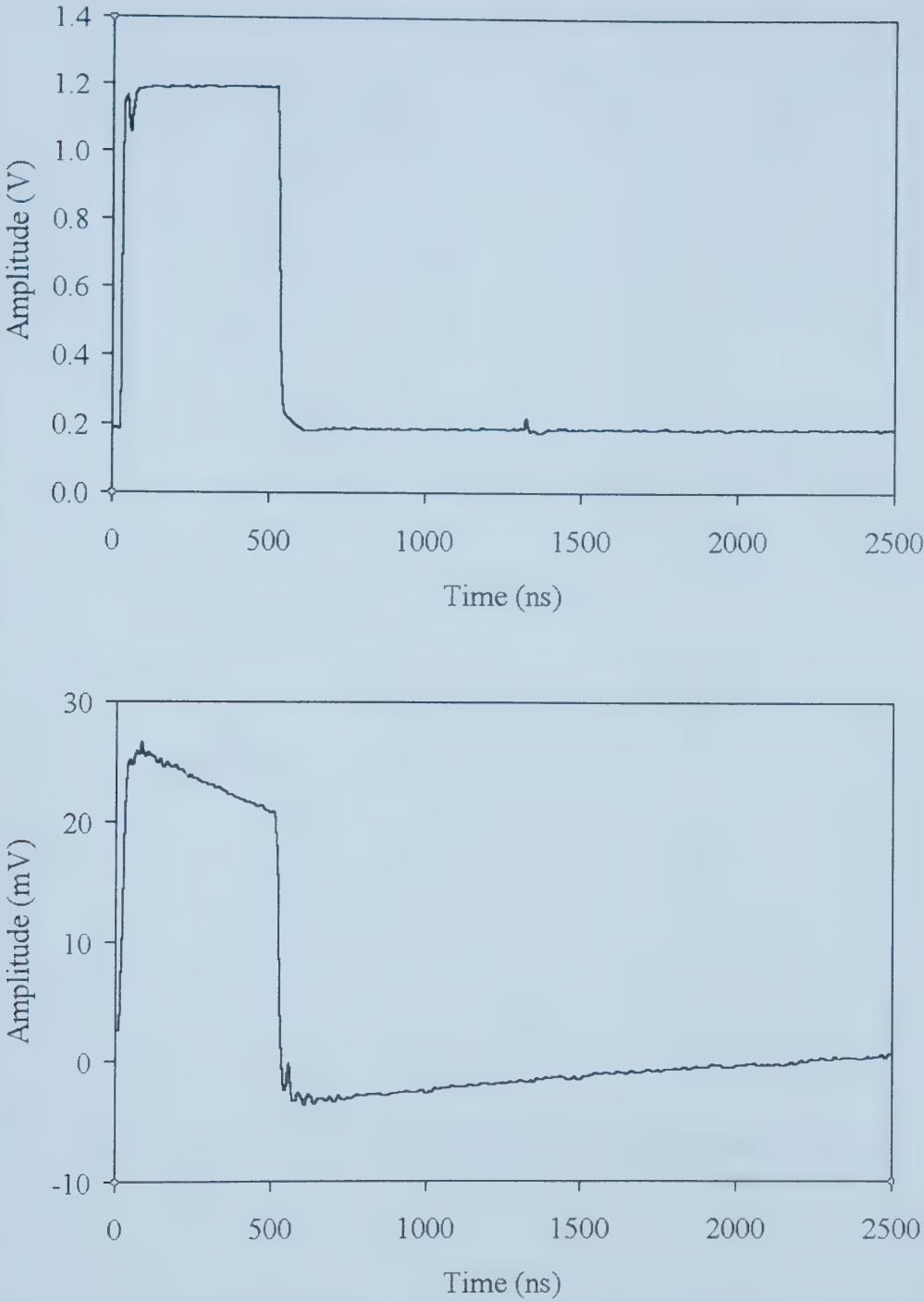


Figure 4.11. Pulse width: 500 ns. Driving electrical pulse (top) and measured optical pulse (bottom). $b_y=6.8$ mT.

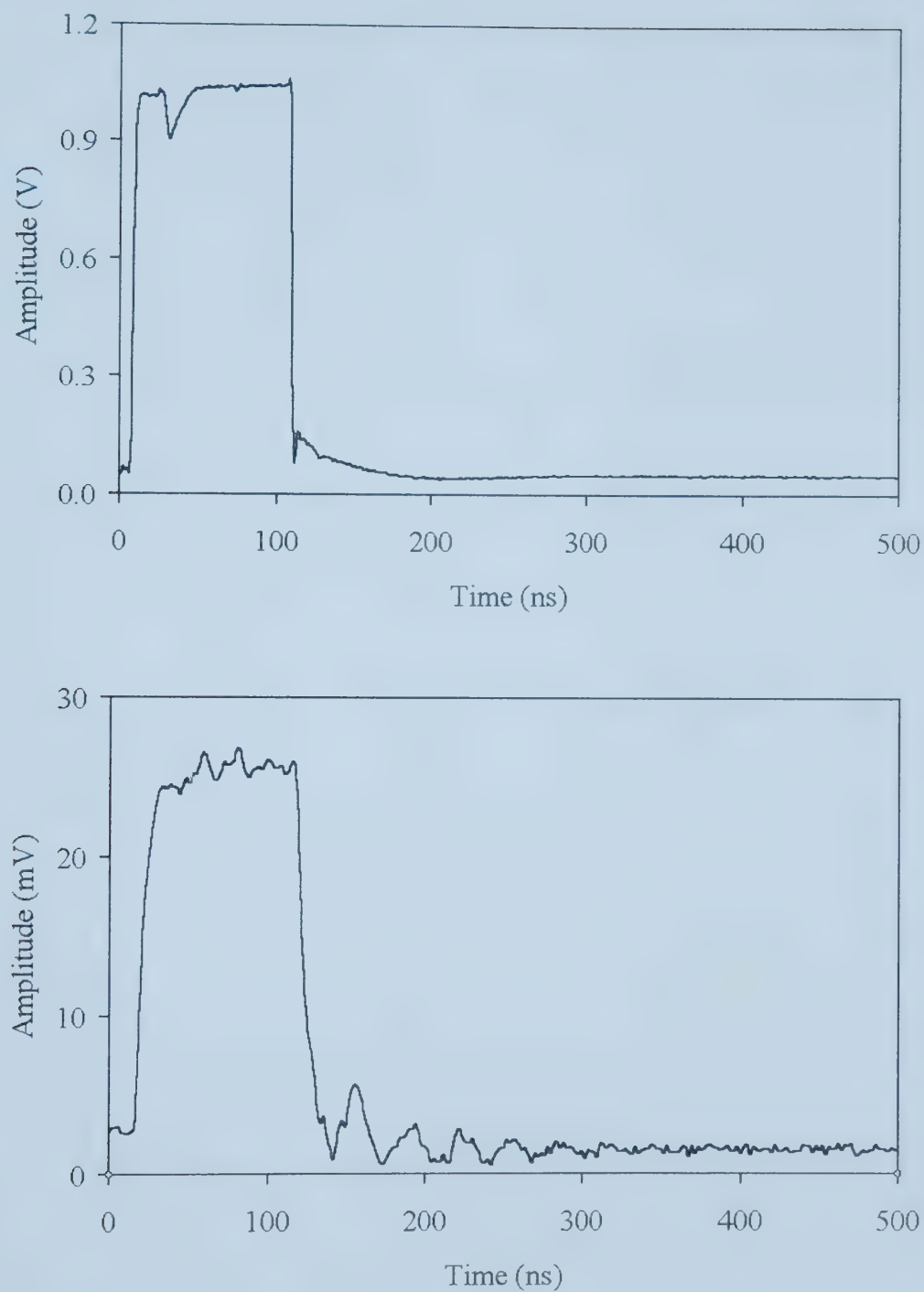


Figure 4.12. Pulse width: 100 ns. Driving electrical pulse (top) and measured optical pulse (bottom). $b_y=6.8$ mT.

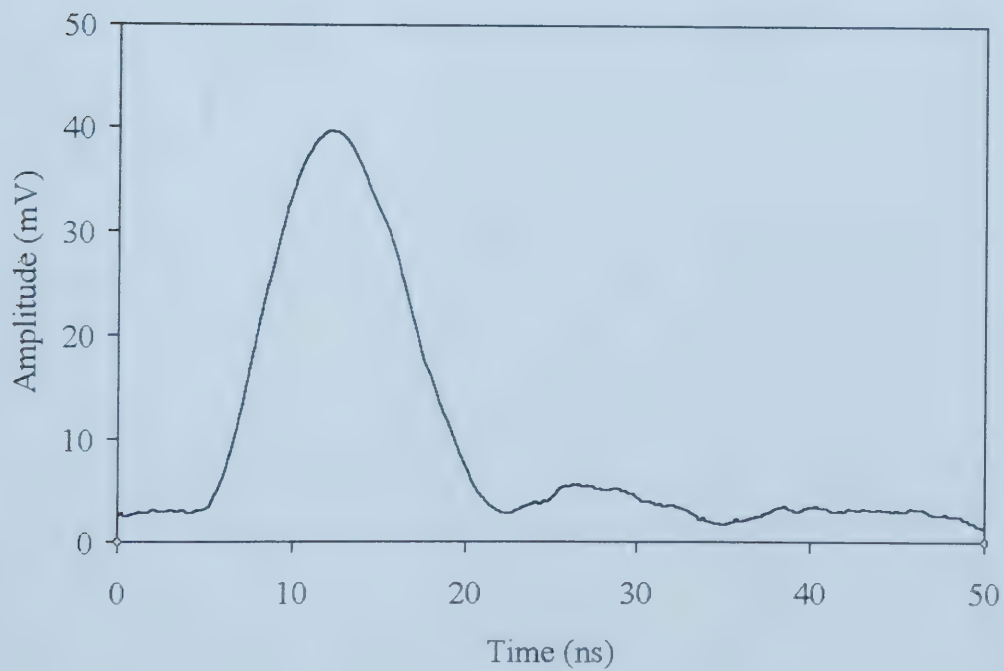
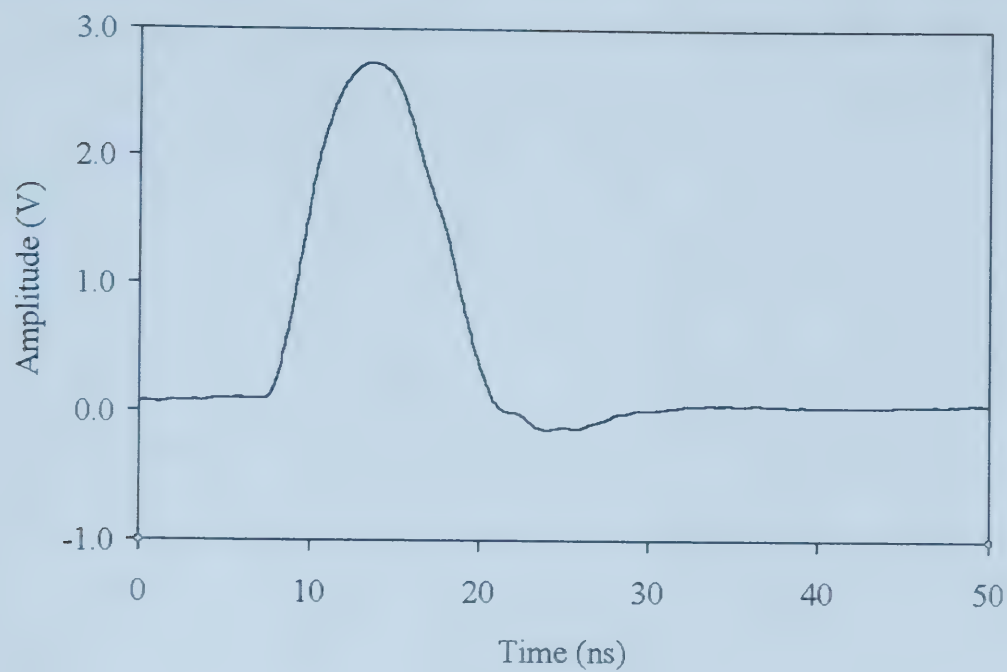


Figure 4.13. Pulse width: 10 ns. Driving electrical pulse (top) and measured optical pulse (bottom). $b_y=7.8$ mT.

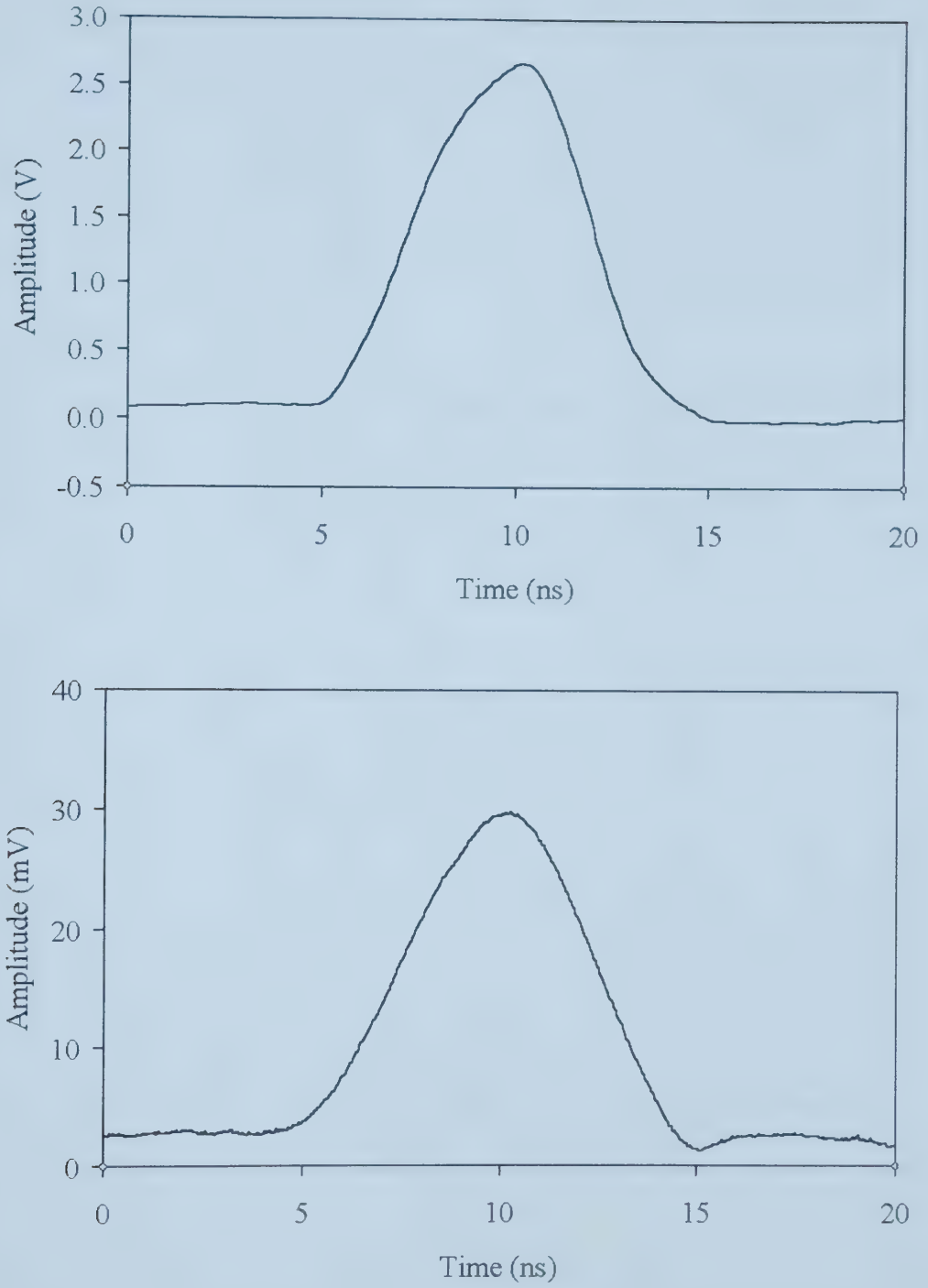


Figure 4.14. Pulse width: 5 ns. Driving electrical pulse (top) and measured optical pulse (bottom). $b_i=8.2$ mT.

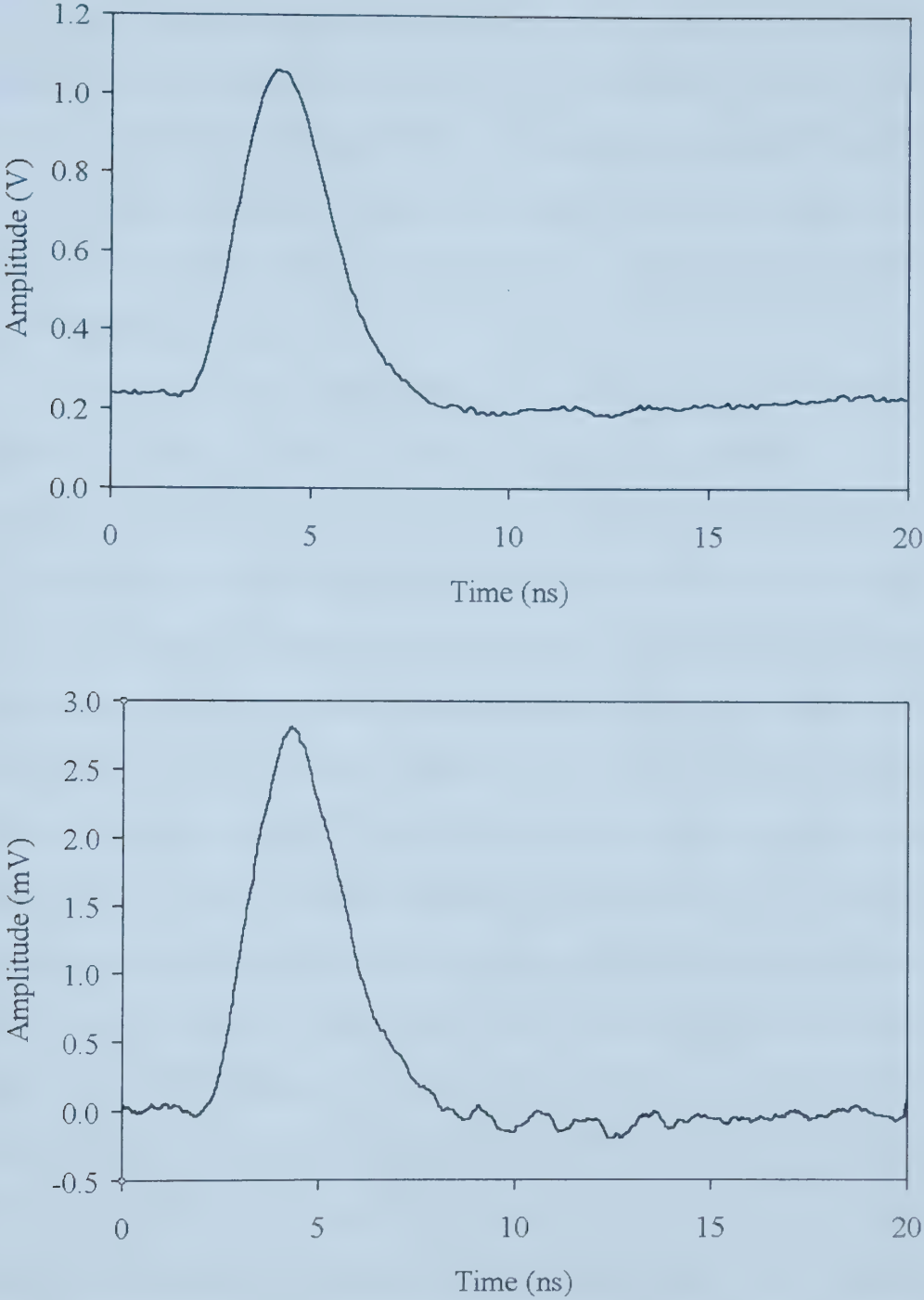


Figure 4.15. Pulse width: 2.3 ns. Driving electrical pulse (top) and measured optical pulse (bottom). $b_j=15$ mT.

due to the low frequency cutoff of the photoreceiver module, quoted to be 44 kHz. The shortest measured pulse shown in figures 4.10-4.15 is a Gaussian-like pulse with a width of ~ 2.3 ns, which can be seen in figure 4.16 with its corresponding electrical input. Here, it is observed that the measured optical pulse is a clear representation of its electrical input. The rise-times and width of the electrical and measured optical pulses differ by only 5 % and 0.3 %, respectively.

For the value of the biasing field used for the pulse in figure 4.16, there corresponds an FMR frequency and similar frequency characteristics for the MO modulator such as those found in figure 4.8. Here, the biasing magnetic field used was 15 mT, corresponding to an FMR frequency of ~ 850 MHz (according to the data in figure 4.7). Figure 4.17 shows the results of a frequency sweep for the MO device at this biasing magnetic field. Here, it is observed that the resonance occurs at 842 MHz, which is consistent with the data presented in figure 4.7. Also plotted in figure 4.17 is the calculated Fourier spectrum of a 2.3 ns Gaussian pulse and the experimentally measured spectrum of the ~ 2.3 ns electrical pulse, the latter of which was obtained with a spectrum analyzer (Hewlett Packard model E4407B, 26 GHz bandwidth). Small deviations from a Gaussian shape are present in the measured spectrum, likely due to fact that the electrical pulses are not ideally Gaussian, but the general shape resembles that of the calculated Fourier transform. The frequency scan indicates that the FMR frequency, which occurs at 842 MHz, is well above both experimental and calculated pulse spectra. In order for the pulse to be well represented, a suitable portion of its spectrum must lie on the flat spectral response region of the MO modulator. A reasonable condition is that all frequencies from DC to the 3-dB point of the Fourier spectrum should lie below resonance. As observed in

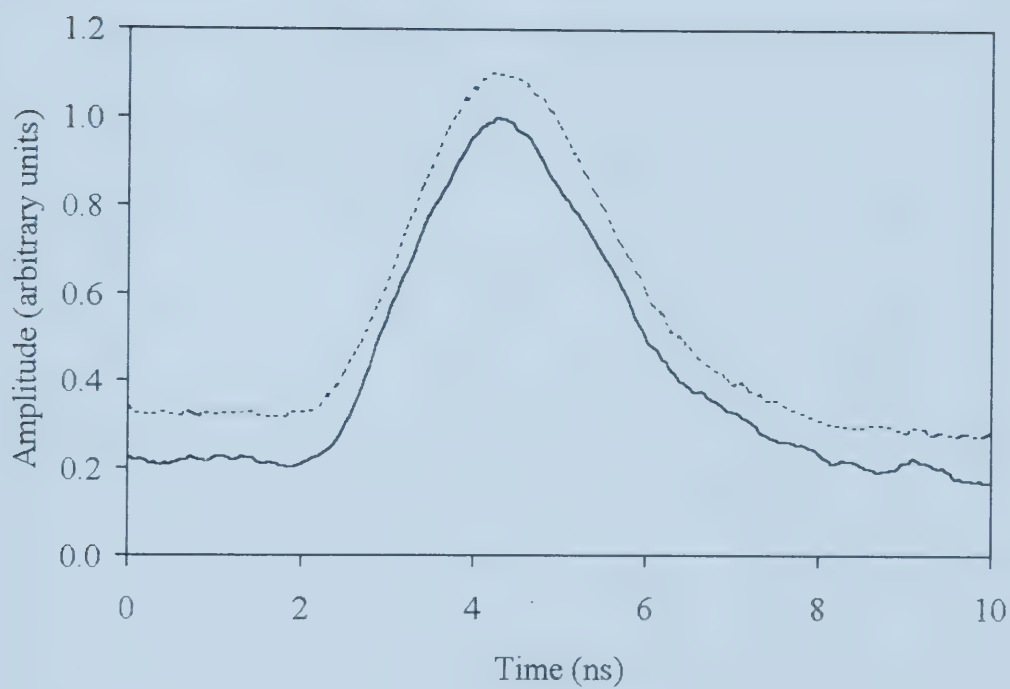


Figure 4.16. Electrical input (dashed line) and optical output (solid line) of the MO modulator for a driving pulse with a FWHM=2.3 ns.

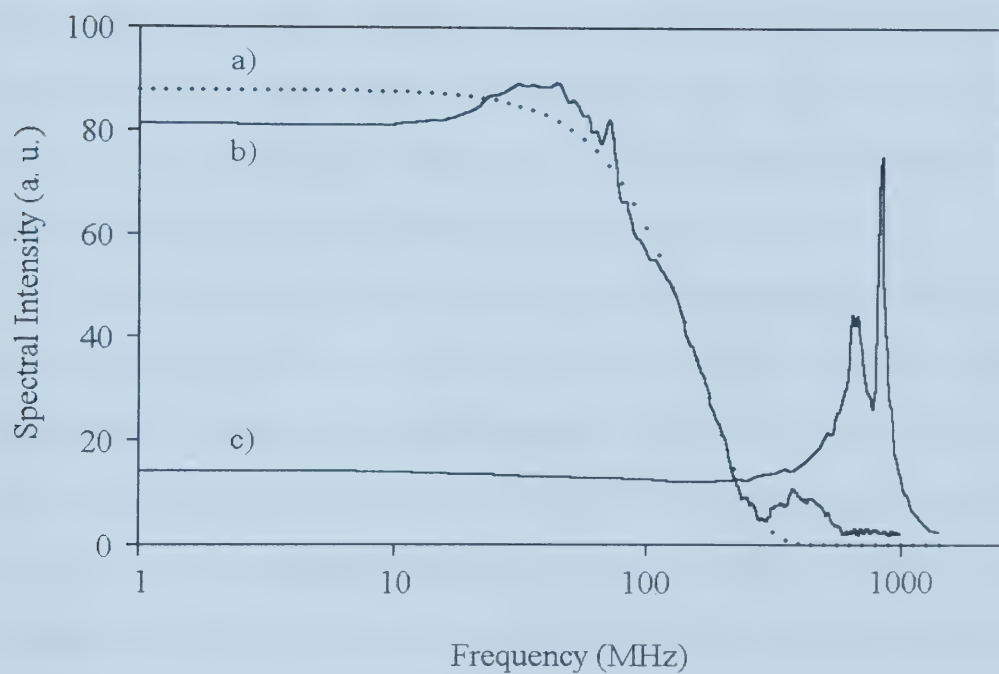


Figure 4.17. The a) calculated and b) measured spectra of a 2.3 ns FWHM Gaussian-like electrical pulse. c) Display of the frequency characteristics of the MO modulator for $b_1=15$ mT.

figure 4.17, the spectrum of the 2.3 ns pulse has its 3-dB point positioned well below the resonance, which supports the fact that the measured time-domain optical pulse is well represented with little distortion.

To highlight the sensitivity of the MO modulator on the externally applied biasing magnetic field, several snapshots of the optical output are taken for slight changes in the biasing field strength and orientation (the maximum change in field strength was less than 5% change). The results are catalogued in figure 4.18. The original optical pulse is plotted along with four others that have had the bias field altered by a small amount. It is clear that as the externally applied field is changed from its optimal value, the measured optical pulse width increases and eventually, the Gaussian-like shape is lost.

The MO modulator is capable of switching times that are much faster than those previously demonstrated. To show this, an electrical pulse with a 10%-90% rise time of 320 ps (generated according to the method described in section 4.1.4) is used to drive the device and the optical output is recorded. The results of this experiment are displayed in figure 4.19 for a biasing magnetic field of 22 mT, where curve (a) is the electrical drive pulse and curve (b) is the measured MO signal. The MO signal rise-time is measured to be 435 ps, which is $\sim 35\%$ larger than that of the electrical pulse. The signature of the FMR is present as a 1.04 GHz periodic modulation on the slow fall.

The application of a stronger static magnetic field eliminates these oscillations and shortens the measured rise-time, but the signal amplitude is reduced, as shown in figures 4.19c and 4.19d. The two curves represent the output of the modulator as the biasing field is increased to 39 mT, and then 52 mT. The measured optical signal rise-times are 357 ps and 343 ps for figures 4.19c and 4.19d, respectively. Increasing the

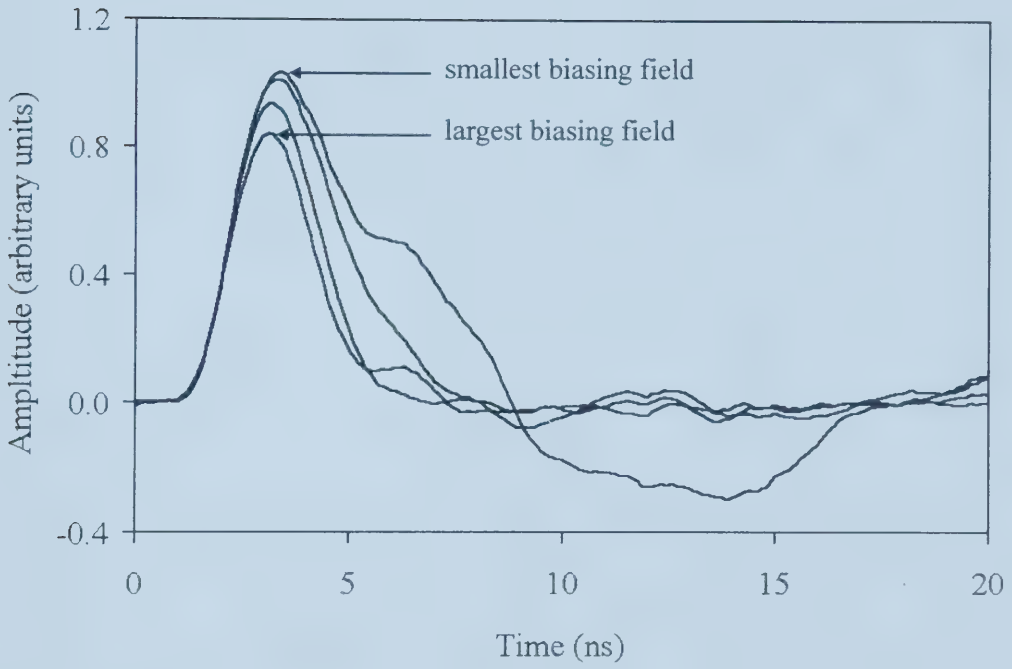


Figure 4.18. Several different outputs corresponding to the same electrical input, but for slight changes in the value of the static field, $b_{y,0}$.

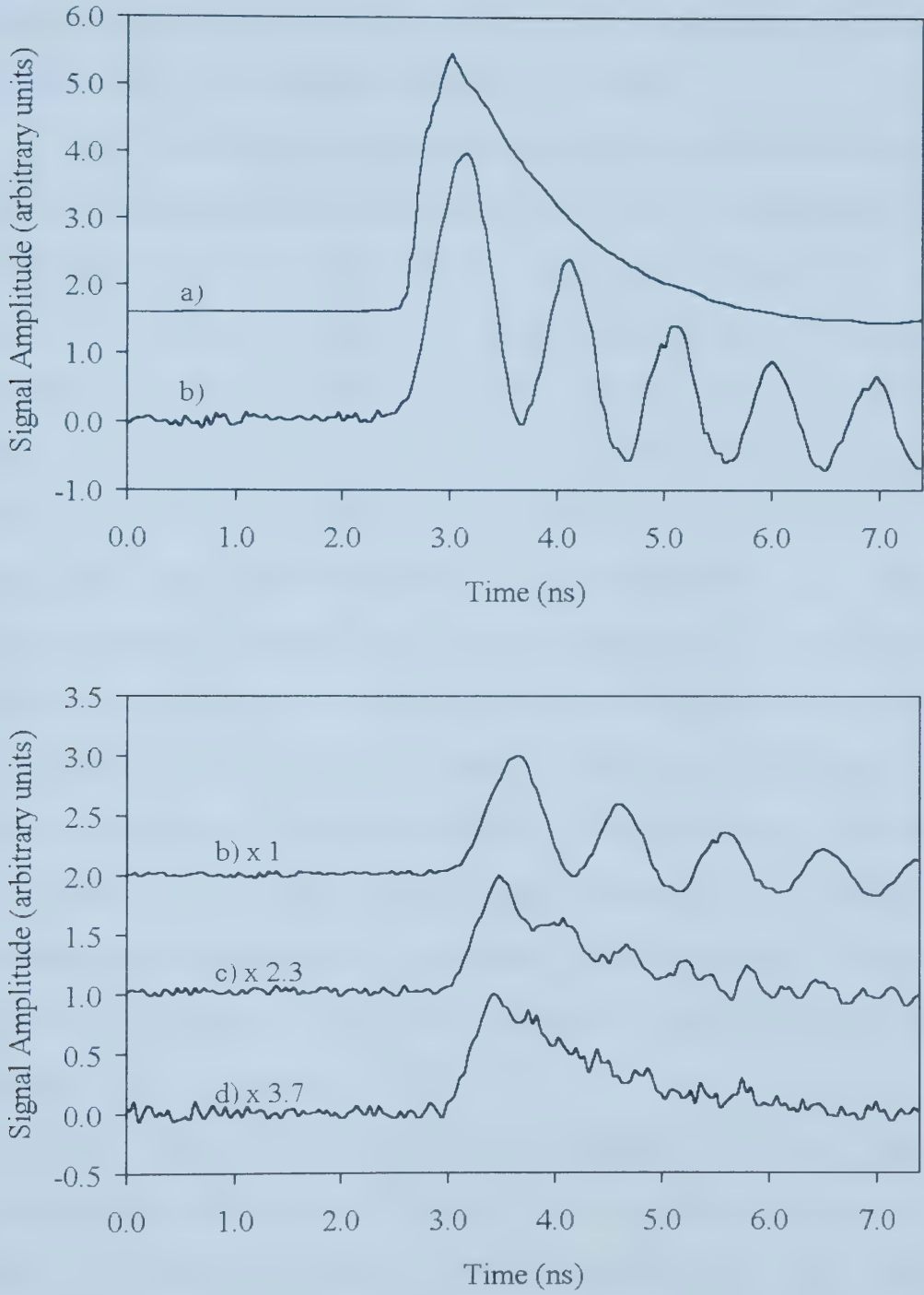


Figure 4.19. a) Electrical driving pulse with a 10%-90% rise-time of 320 ps. Curves b), c), and d) show the corresponding MO modulator output for $b_1 = 22, 39$, and 52 mT, respectively.

amplitude of the drive pulse will increase the MO signal amplitude, but this was not verified, as a high-voltage short pulse generator was not available.

The MO modulator is further pushed to test limits of the experimental set-up. These limits are due to the impedance matching characteristics of the MO modulator and the photoreceiver bandwidth. Even though these characteristics are expected to be less than optimal at frequencies above 1 GHz, useful predictions about the high-speed operation of this device can still be made. As per the discussion in the previous paragraph, a high-voltage short pulse generator was not available. Therefore, the single frequency source was used for this experiment, where an FMR frequency of 1.5 GHz is chosen using a biasing field of 30 mT and the frequency characteristics of the modulator are mapped between 1 MHz and 1.7 GHz. The resulting plot is shown in figure 4.20a and it is observed that the spectral response curve follows the same general trend as the previous frequency sweep curves at 500 MHz, 750 MHz, 1GHz, and 842 MHz. The previous frequency scans showed resonance response amplitudes of approximately 100 mV, whereas in this case, the response amplitude is reduced to 38 mV. This 62% decrease in amplitude at the resonance was expected from the impedance matching and the roll-off of the detector above 1 GHz. Nonetheless, a large and relatively flat bandwidth is observed from 1 MHz to 1 GHz.

Figure 4.20a can be used to make useful predictions on achievable optical modulation pulse durations using the MO device. The Fourier spectra of several Gaussian pulses with a variety of FWHMs are plotted in figure 4.20 (curves b-f). As stated previously, all frequencies from DC to the 3-dB point of the Fourier spectrum should lie on the flat response region below resonance. It can be seen in figure 4.20 that pulses with

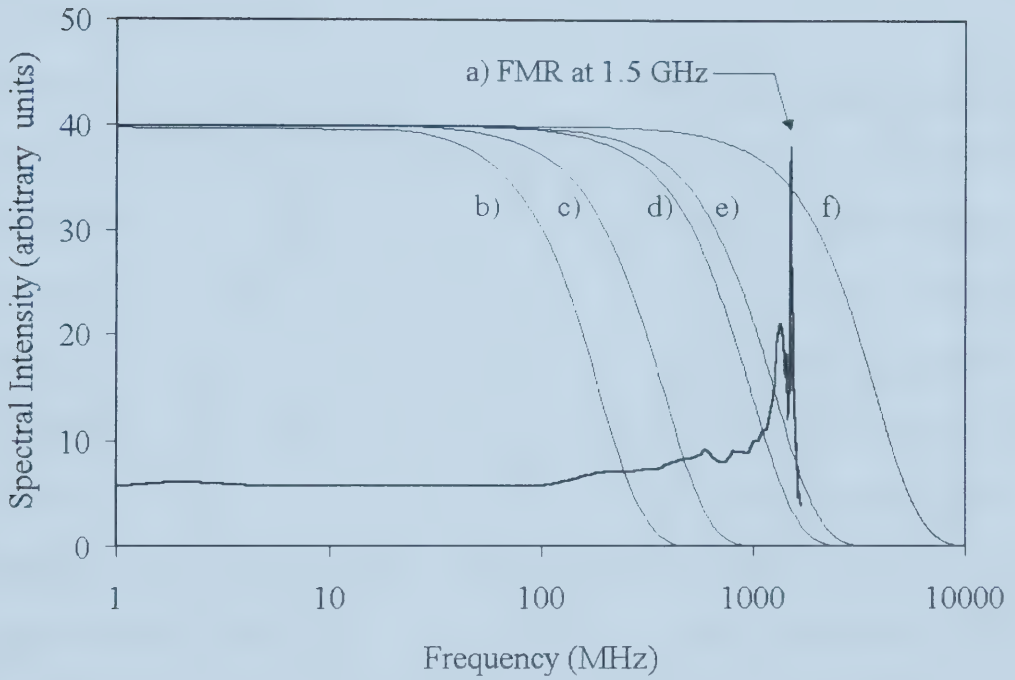


Figure 4.20. a) Frequency characteristics of the MO modulator, exhibiting a 1.5 GHz FMR for $b_y = 30$ mT. Fourier power spectra of Gaussian pulses of various FWHM: b) 2 ns, c) 1 ns, d) 500 ps, e) 300 ps, and f) 100 ps.

FWHM ranging from 2 ns to 300 ps satisfy this criterion. For the 100 ps pulse, a large portion its spectrum lies on or above the resonance, and therefore, the optical trace would not be representative of the input pulse, as the time-domain optical signal would be distorted. Therefore, with the current experimental set-up, the MO modulator is expected to properly modulate pulses as short as 300 ps.

4.2.3 Modulation Depth

An important parameter for practical devices is the modulation depth, which is the quotient of the amplitude of the modulated optical power and the DC optical power. To calculate the modulation depth directly, a low frequency photodetector (UDT Sensors, Inc., 10DP, 2 μ s rise-time) capable of operating at DC is used to measure the optical signal resulting from a 100 kHz sine wave modulation. To perform this, the system was first optimized for resonance operation at 750 MHz, then the driving frequency was lowered to 100 kHz and the beam was directed to the photodetector. Since the output of the detector was not capacitively coupled, a DC offset was measured on the optical signal, on top of which was the modulated signal. The measured modulation amplitude was 0.5 mV and the DC offset was 16 mV. Taking the ratio of the two voltages yields an optical modulation depth of approximately 3% (off resonance). Using this information, the modulation depth at higher frequencies can be calculated using ratios of the intensities. Since the measured resonant amplitude of the signal at 750 MHz is 5 times higher (125 mV_{pp}) than the flat response level (25 mV_{pp}), the modulation depth is calculated to be 15%. Based on these measurements and with the known characteristics of the low-frequency detector (i.e. biasing resistor is 5 k Ω and the responsivity is 0.5

A/W), the optical power amplitude of the 2.3 ns pulse discussed in section 4.2.2 is calculated to be $0.048 \mu\text{W}$.

4.3 Summary

It is evident from the above experiments that modulation techniques based on the MO effect are feasible, and may eventually be competitive with current techniques (such as electro-optic or acousto-optic modulators). Using the simple modulator device constructed here, an optical beam was modulated using electrical pulses as short as 2.3 ns, and single frequency modulation was demonstrated with a maximum effective bandwidth of 1.0 GHz. In the final experiment, the modulator was pushed to a maximum resonance frequency of 1.8 GHz, where it was observed that sub-nanosecond pulse modulation is possible using this device (this maximum frequency was ultimately governed by the test system). In the following Chapter, many improvements are listed, which will increase the operation speed and efficiency of future modulators.

4.4 References

- [1] G. B. Scott and D. E. Lacklison, "Magneto-optic Properties and Applications of Bismuth Substituted Iron Garnets," *IEEE Trans. Magn.*, vol. MAG-12, pp. 292-309, 1976.
- [2] P. Lorrain, D. R. Corson, and F. Lorrain, *Electromagnetic Fields and Waves*, 3rd Ed. New York: W H. Freeman and Company, 1987, pp. 143.
- [3] A. Y. Elezzabi and M. R. Freeman, "Ultrafast magneto-optic sampling of picosecond current pulses," *Appl. Phys. Lett.*, vol. 68, pp. 3546-3548, 1996.

- [4] G. Jones and A. Y. Elezzabi, "Ultrafast broadband tunable-bandwidth magneto-optic modulator," in *Proc. SPIE*, 1999, pp. 145-152.
- [5] R. L. White and I. H. Solt, "Multiple Ferromagnetic Resonance in Ferrite Spheres," *Phys. Rev.*, vol. 104, pp. 56-62, 1956.

Chapter 5

Conclusion

In this thesis, the theory and operation behind MO modulation is described in detail. A new model is outlined and employed to predict the operation of an MO modulator and a novel MO beam deflector. For this theoretical treatment, two models are integrated to provide a more comprehensive description of the performance of the above-mentioned devices. The first model governs light-wave effects (such as waveguide propagation, birefringence, and mode conversion), while the second model describes the time evolution of the magnetization vector. Both of these processes are fundamental to the understanding of MO modulation, as the Faraday effect is linked with the state of magnetization of the iron garnet film used in the construction of the MO devices.

Using this model, an idealized MO modulator is predicted to have a mode conversion efficiency of 42% (at 1550 nm) when driven with 1.0 ns electrical pulses. In addition, the versatility of this model is demonstrated when it is used to simulate the operation of a high-speed MO beam deflector. This novel MO device is described in detail and is predicted to have a deflection efficiency of 20% at multi-gigahertz bandwidths. This actively controlled phase grating could find applications in hybrid time-domain/wavelength division demultiplexing.

After a detailed discussion of the principles of MO modulation and the model mentioned above, the experimental results of a Bi-YIG MO modulator are illustrated. The fabrication procedures of the MO modulator are described, and the experimental

arrangement used to study its operation is explained in detail. Here, two modes of operation are demonstrated: resonant and non-resonant modulation. The mode of operation of the device is determined by the application of a static magnetic field, which determines the FMR of the Bi-YIG. The ability to tune the FMR gives the MO modulator the unique feature of adjustable bandwidth.

To operate the MO modulator resonantly, the device is driven at the FMR frequency, and a maximum single frequency modulation of 1.8 GHz was achieved. For non-resonant broadband modulation, the MO modulator is driven below the FMR resonance where the device is shown to have a large and nearly uniform bandwidth. In this operational mode, pulses as short as 2.3 ns are imparted onto an optical beam. Switching times as short as 343 ps are achieved using a 320 ps driving electrical pulse, demonstrating the high bandwidth capability of the device. For the non-resonant mode of operation, the largest bandwidth of the device is measured to be ~ 1 GHz, revealing the possibility of sub-nanosecond MO modulation.

The theoretical predictions and experimental results of this thesis demonstrate the “proof of principle” of MO modulation utilizing Bi-YIG, however, improvements can be made. As discussed in Chapter 3, the non-matched velocity condition of the TE and TM modes in the Bi-YIG film waveguide leads to a reduction in mode conversion efficiency. For future MO modulators, the polarization modes should be properly matched. This has been accomplished in work performed by Wolfe et al. [1] where a matched condition between the TE and TM modes is achieved by balancing several contributions to birefringence using multi-layered Bi-YIG films. These contributions include stress-induced, growth-induced, and shape or geometrical birefringence. The stress-induced

contribution is due to the film-substrate lattice mismatch, which is inherent in most epitaxial films. Growth-induced birefringence is independent of film thickness, and is specific to garnet materials. Growth-induced birefringence is highly dependent on the material composition and growth parameters [1]. Geometrical birefringence, which depends on the thickness of the MO film, results from the different propagation constants of the TE and TM modes in a slab waveguide. Using the fact that the geometrical birefringence is thickness-dependent, the authors were able to etch a sample until the thickness was reduced to a point where the various contributions to the birefringence cancel each other and the TE and TM mode velocities were matched. Unfortunately, birefringence compensation was not performed for the Bi-YIG film used in this study, as an LPE facility was not available.

As mentioned in Chapter 4, the absorption coefficient of the Bi-YIG film used for the MO modulator is 400 cm^{-1} at a wavelength of 800 nm. Given the absorption and Faraday rotation of this particular Bi-YIG film, a calculation showed that the optimal length of the device should be approximately one absorption depth in the material ($25 \text{ }\mu\text{m}$). However, a length of $60 \text{ }\mu\text{m}$ was used instead, which was the shortest length achievable with the polishing process used. Evolved polishing techniques such as those used in commercial production systems could be applied here to achieve higher quality MO samples with the optimal interaction length.

Another possibility is to tailor the Bi-YIG composition to reduce the absorption at the designed wavelength and allowing the device length to be increased. The obvious goal is to maintain the high Faraday rotation while reducing the absorption, and it is entirely conceivable that such a combination of atomic substitutions exists for a given

wavelength. Additional research is required to determine this combination. Contact with an LPE group has been established in the hope to achieve higher quality Bi-YIG films for modulators and other optical communication devices [2].

The electrical system of the MO modulator is an integral aspect of its operation. It consists of an electrical transmission line that carries high-speed current transients to the MO film. This transmission line is a single current-carrying wire constructed of indium, which was placed in direct contact with the MO film. Typical transmission lines require an accompanying ground line to properly guide electrical signals and minimize losses due to impedance mismatch. As such, future MO modulation designs should have this ground line close to the signal line in order to reduce electrical power loss of the input signal. Additionally, the entire device should be contained within a metal enclosure, which would shield external noise and provide additional mechanical support and stability. The current design of the MO modulator uses free space optics to couple into and out of the Bi-YIG waveguide. The next generation MO modulator could have the optical input and output brought to and from the sample using polarization-maintaining fibre, allowing for a smaller device design, a smaller RF circuit, and a more complete enclosure.

With the above improvements, the MO modulator could compete with contemporary techniques of modulation, having the added features of dual mode operation and tunability of bandwidth. As growth techniques for Bi-YIG films evolve, it is expected that garnets with low absorption, low saturation magnetization, and high Faraday rotation will become readily available, which would increase the efficiency and bandwidth of devices based on such material.

5.1 References

- [1] R. Wolfe, V. J. Fratello, and M. McGlachan-Powell, "Thin-film garnet materials with zero linear birefringence for magneto-optic waveguide devices," *J. Appl. Phys.*, vol. 63, pp. 3099-3103, 1988.
- [2] Eugene Il'yashenko, University of Oslo, private communication.

Appendix A

Computer Algorithm for the BPM-LL Model

This appendix contains Visual C++ code for the BPM-LL model presented in Chapter 3.

This is the *.cpp file for the beam propagation code:

```
// BPM-LL, current geometry: beam deflector
#include "stdafx.h"
#include <math.h>           //math library
#include <iostream.h>       //input and output streams
#include <fstream.h>        //file streams, for writing files
#include <process.h>
#include "mycomplex.h"     //complex number class
#include "new_matrix.h"    //matrix class
#include <afx.h>

#define Pi 3.14159265358979

//define dimensions, all lengths are in microns
#define grating_spacing 6.0           //spacing for the MO deflector films
#define transmission_line_grating_spacing (grating_spacing+1.0)

#define d 150.0           //length of film
#define cladding_layer 1.0 //cladding layer width
#define center_cladding_layer 0.1 //ITO layer width
#define transmission_line_width 0.1 //gold transmission line width
#define transmission_line_depth d //gold transmission line thickness

#define n_mo 2.3           //Bi-YIG refractive index, no birefringence
#define n_third_layer 1.0 //air layer index after the grating
#define n_ito 1.96        //refractive index for ITO
#define n_cladding 1.94    //refractive index for cladding layer
#define theta_f 0.25       //Faraday rotation of the Bi-YIG films

//define other parameters
#define dx 0.1             //x step size
#define dz 0.2             //z step size
#define threshold 1e-40    //threshold parameters used to determine if theta_f is zero
#define current 5.0        //peak current amplitude of the transient pulse
#define line1 1.0          //current direction in transmission line 1
#define line2 -1.0         //current direction in transmission line 1
#define line3 1.0          //current direction in transmission line 1
//the following parameter is a coefficient for the expression which calculates the magnetic
field distribution
```



```

#define prefactor_grating 1.0/transmission_line_depth/transmission_line_width
                                *2.0*(1e-7)*current/(1e-6)

#define m_h 0.02                //Landau-Lifshitz step size
#define m_yi1 0.0               //magnetization initial condition
#define m_yi2 0.0               //magnetization initial condition
#define m_yi3 1.0               //magnetization initial condition
#define m_t1 100.0              //spin relaxation time
#define m_t2 100.0              //spin relaxation time
#define m_Hz 0.0275             //bias field
#define m_FWHM 1.0              //FWHM of input time pulse
#define m_offset 1 2.5          //time center of the gaussian pulse

double m_t=0.0;                 //time at which magnetization response is calculated

#define l 1500                  //number of points along z
#define M 1200                  //number of points along x
#define lambda 1.55              //wavelength
#define eta theta_f*n_mo*lambda/180.0 //off-diagonal tensor parameter
#define z_offset 0.0            //z profile offset
#define x_offset (-dx*M)/2.0    //x profile offset
#define profile_offset (-dx*M)/2.0 //input profile offset
#define k_0 2*Pi/lambda         //free space wave-vector
//the following parameter is the propagation constant
double beta_r=sqrt(k_0*k_0*n_mo*n_mo-Pi*Pi/grating_spacing/grating_spacing);
#define prefactor_mycomplex(0.0,dz/2.0) //coefficient of beam propagation matrices
#define I mycomplex(0.0,1.0)         //the complex unit
#define FWHM 2*grating_spacing      //FWHM of launched radiation
#define n_iter 100                  //number of iterations in Jacobi method
#define start_writing_data 0.0      //beginning of data output along z
#define x_start 200                  //beginning of data output along x
#define x_end 1000                   //last data point along x to be written
#define abc_coefficient 0.001       //absorbing boundary coefficient
#define boundary_points 50           //number of points in absorbing boundary
#define reduction_x 2                //reduction factor for number of x points written
#define number_of_points_in_time 75 //number of points in time
#define end_point_in_time 5.0        //last point in time

double index(double x, double z);    //refractive index profile for TM
double index_y(double x, double z);  //refractive index profile for TE
double rotation(double x, double z); //Faraday rotation profile
double initial_profile(double x); //centered on zero //input to the program
double gaussian(double x); //centered on zero //a gaussian function
int myround(double x);                //rounding function

```



```
//important functions for calculating the BPM matrices and output vectors
```

```
void fillR_l(mycomplex MM_aa[],mycomplex MM_bb[],mycomplex
MM_cc[],mycomplex MM_dd[],mycomplex MM_ee[],int z_step);
void fillS_l(mycomplex MM_aa[],mycomplex MM_bb[],mycomplex
MM_cc[],mycomplex MM_dd[],mycomplex MM_ee[],int z_step);
void zero(matrix& x,matrix& y,matrix& z,matrix& u,matrix& w);
void zero(matrix& x,matrix& y,matrix& z);
void tridiag(mycomplex aa[],mycomplex bb[],mycomplex cc[],mycomplex
rr[],mycomplex uu[],int n);
void iteration(mycomplex aa[],mycomplex bb[],mycomplex cc[],mycomplex
dd[],mycomplex ee[],mycomplex xx[],mycomplex rr[]);
void gauss_jordan(matrix &aa,mycomplex bb[],mycomplex uu[]);
void zero(matrix& x,matrix& y);
void matrix_multiply(matrix& aa,mycomplex rr[], mycomplex xx[]);
void write_parameters(ostream& out);
```

```
//helper functions for calculating the magnetic field distribution from a transmission line
```

```
double x_coord(double x,double y);
double y_coord(double x,double y);
double x_coord_single_line(double x,double y);
double y_coord_single_line(double x,double y);
double yd_atan(double x,double y);
double y_atan(double x,double y);
double xl_log(double x,double y);
double x_log(double x,double y);
double xl_atan(double x,double y);
double x_atan(double x,double y);
double yd_log(double x,double y);
double y_log(double x,double y);
double magnitude(double x,double y);
```

```
//function used to calculate the magnetization response from the LL
```

```
double f1(double t,double y1,double y2,double y3,double m_h_x0);
double f2(double t,double y1,double y2,double y3,double m_h_x0);
double f3(double t,double y1,double y2,double y3,double m_h_x0);
void forward_iterate(double t, double &y1, double &y2, double &y3, double h,double
m_h_x0);
double h_transient(double t,double m_h_x0);
double magnetization_response(double m_h_x0);
```

```
//the main program
```

```
int main(int argc, char* argv[])
```

```
{
```

```
    CTime startTime = CTime::GetCurrentTime();
```



```

//initialize file streams
ofstream output_x,output_time,output_z_te,output_z_tm,number,parameters,
        h_y_profile,rotation_profile,index_profile;

//open files
output_x.open("xdata.txt");
output_time.open("time_data.txt");
output_z_te.open("zdata_te.txt");
output_z_tm.open("zdata_tm.txt");
number.open("number.txt");
parameters.open("parameters.txt");

write_parameters(parameters); //write parameters
CTime time=CTime::GetCurrentTime(); //time the program
CString month_array[12];
month_array[0]="Jan";month_array[1]="Feb";month_array[2]="Mar";
month_array[3]="Apr";month_array[4]="May";month_array[5]="Jun";
month_array[6]="Jul";month_array[7]="Aug";month_array[8]="Sep";
month_array[9]="Oct";month_array[10]="Nov";month_array[11]="Dec";

parameters<<month_array[time.GetMonth()-1]<<" "<<time.GetDay()
<<" "<<time.GetHour()<<":";

if(time.GetMinute()<10){
    parameters<<"0";
}

parameters<<time.GetMinute()<<endl; //write out start time
number<<M<<" "<<1<<endl;

mycomplex RR_aa[2*M+2],SS_aa[2*M+2],RR_bb[2*M+2],SS_bb[2*M+2],
RR_cc[2*M+2],SS_cc[2*M+2],RR_dd[M+1],SS_dd[M+1],RR_ee[M+1],
SS_ee[M+1],Right_aa[2*M+2],Left_aa[2*M+2],Right_bb[2*M+2],
Left_bb[2*M+2],Right_cc[2*M+2],Left_cc[2*M+2],Right_dd[M+1],
Left_dd[M+1],Right_ee[M+1],Left_ee[M+1];

mycomplex vl[2*M+2],aa[2*M+2],bb[2*M+2],cc[2*M+2],dd[M+1],ee[M+1],
xx[2*M+2],rr[2*M+2],uu[2*M+2];

double zcoordinate;
bool yes_no;
int iter_count=0;

//write x-data
for(int llllllllll=x_start;llllllllll<=x_end;llllllllll+=reduction_x){
    output_x<<llllllllll*dx<<endl;

```



```

}
//begin time step
for(int current_time_step=0;
    current_time_step<=number_of_points_in_time;current_time_step++)
{
    m_t=current_time_step*end_point_in_time/number_of_points_in_time;
    for(int ii=0;ii<M+1;ii++){
        vl[ii]=initial_profile(ii*dx+profile_offset);
        vl[ii+M+1]=0.0;
    }//set input vector

    for(int jz=0;jz<l;jz++){
        zcoordinate=jz*dz+z_offset;

        if(zcoordinate<=d){
            yes_no=true;
            beta_r=sqrt(k_0*k_0*n_mo*n_mo-
                Pi*Pi/grating_spacing/grating_spacing);
        }

        else{
            yes_no=false;
            beta_r=k_0*n_third_layer;
        }

        if(theta_f<1e-10){
            yes_no=false;
        }

        //fill propagation matrices
        fillR_l(RR_aa,RR_bb,RR_cc,RR_dd,RR_ee,jz);
        fillS_l(SS_aa,SS_bb,SS_cc,SS_dd,SS_ee,jz);

        for(int i=0;i<2*M+2;i++){
            Left_aa[i]=RR_aa[i]+(-1)*prefactor*SS_aa[i];
            Right_aa[i]=RR_aa[i]+prefactor*SS_aa[i];
            Left_bb[i]=RR_bb[i]+(-1)*prefactor*SS_bb[i];
            Right_bb[i]=RR_bb[i]+prefactor*SS_bb[i];
            Left_cc[i]=RR_cc[i]+(-1)*prefactor*SS_cc[i];
            Right_cc[i]=RR_cc[i]+prefactor*SS_cc[i];
            aa[i]=0.0;
            bb[i]=0.0;
            cc[i]=0.0;
        }

        for(i=0;i<M+1;i++){

```



```

        Left_dd[i]=RR_dd[i]+(-1)*prefactor*SS_dd[i];
        Right_dd[i]=RR_dd[i]+prefactor*SS_dd[i];
        Left_ee[i]=RR_ee[i]+(-1)*prefactor*SS_ee[i];
        Right_ee[i]=RR_ee[i]+prefactor*SS_ee[i];
        dd[i]=0.0;
        ee[i]=0.0;
    }

rr[0]=Right_bb[0]*vl[0]+Right_cc[0]*vl[1]+Right_ee[0]*vl[M+1];
rr[M]=Right_aa[M]*vl[M-1]+Right_bb[M]*vl[M]+Right_ee[M]*vl[2*M+1];
rr[M+1]=Right_bb[M+1]*vl[M+1]+Right_cc[M+1]*vl[M+2]+Right_dd[0]*vl[0];
rr[2*M+1]=Right_aa[2*M+1]*vl[2*M]+Right_bb[2*M+1]*vl[2*M+1]+Right_d
d[M]*vl[2*M+1];

for(int kk=1;kk<M;kk++){
    rr[kk]=Right_aa[kk]*vl[kk-1]+Right_bb[kk]*vl[kk]
    +Right_cc[kk]*vl[kk+1]+Right_ee[kk]*vl[M+1+kk];
    rr[M+1+kk]=Right_aa[M+1+kk]*vl[M+1+kk-1]
    +Right_bb[M+1+kk]*vl[M+1+kk]
    +Right_cc[M+1+kk]*vl[M+1+kk+1]
    +Right_dd[kk]*vl[kk];
}
for(int m=1;m<2*M+1;m++){
    bb[m]=Left_bb[m];
    aa[m+1]=Left_aa[m+1];
    cc[m-1]=Left_cc[m-1];
}
for(m=0;m<M+1;m++){
    dd[m]=Left_dd[m];
    ee[m]=Left_ee[m];
}

bb[0]=Left_bb[0];
bb[2*M+1]=Left_bb[2*M+1];

//if theta_f=0, use tridiag to solve
if(!yes_no){
    tridiag(aa,bb,cc,rr,xx,2*M+1);
}
//if theta_f is not zero, use the iterative method
if(yes_no){
    if(iter_count==0){
        tridiag(aa,bb,cc,rr,xx,2*M+1);
        cout<<"tridiag first"<<endl;
    }
    tridiag(aa,bb,cc,rr,xx,2*M+1);
}

```



```

        iteration(aa,bb,cc,dd,ee,xx,rr);
        iter_count++;
    }

    xx[0]=0.0;
    xx[M]=0.0;
    xx[M+1]=0.0;
    xx[2*M+1]=0.0;

    // absorbing boundary condition
    for(int iiii=1;iiii<boundary_points;iiii++){
        xx[boundary_points-iiii]=xx[boundary_points-iiii]
            *exp(-(abc_coefficient*iiii));
        xx[M-boundary_points+iiii]=xx[M-boundary_points+iiii]
            *exp(-(abc_coefficient*iiii));
        xx[M+1+boundary_points-iiii]
            =xx[M+1+boundary_points-iiii]
            *exp(-(abc_coefficient*iiii));
        xx[2*M+1-boundary_points+iiii]
            =xx[2*M+1-boundary_points+iiii]
            *exp(-(abc_coefficient*iiii));

    }

    for(int ll=0;ll<M+1;ll++){
        vl[ll]=xx[ll];
        vl[M+1+ll]=xx[M+1+ll];
    }

    cout<<jz<<"\t"<<m_t<<endl;//program progress

} //end jz loop
output_time<<m_t<<endl;//write y-data
for(int llll=x_start;lll<=x_end;lll+=reduction_x){
    //the next line writes out the intensity, i.e. the current vector
    output_z_te<<(8.854e-12)
        *n_mo*n_mo*xx[llll].amplitude()*xx[llll].amplitude()
        <<endl;;
    output_z_tm<<(1.2566e-6)
        *xx[llll+M+1].amplitude()*xx[llll+M+1].amplitude()
        <<endl;
}

} //end time loop

```



```

//close file streams
number.close();
output_x.close();
output_time.close();
output_z_te.close();
output_z_tm.close();

CTime endTime = CTime::GetCurrentTime();//write finish time
CTimeSpan elapsedTime = endTime - startTime;//write run time
parameters<<elapsedTime.GetTotalHours()<<" hr "
                <<elapsedTime.GetMinutes()<<" min "
                <<elapsedTime.GetSeconds()<<" sec"<<endl;
time=CTime::GetCurrentTime();
parameters<<month_array[time.GetMonth()-1]<<" "<<time.GetDay()<<" "
                <<time.GetHour()<<":";
if(time.GetMinute()<10){
    parameters<<"0";
}
parameters<<time.GetMinute()<<endl;

parameters.close();//close parameters file
return 0;
}

//refractive index profile
double index(double x, double z) {
    if(z<=d){
        if(abs_val(x)<=center_cladding_layer/2.0){
            return n_ito*n_ito;
        }
        if(abs_val(x)<=grating_spacing+center_cladding_layer/2.0){
            return n_mo*n_mo;
        }

        if(abs_val(x)<=(grating_spacing+center_cladding_layer/2.0+cladding_layer)){
            return n_cladding*n_cladding;
        }
        return n_third_layer*n_third_layer;
    }
    else{
        return n_third_layer*n_third_layer;
    }
}

//refractive index profile

```



```

double index_y(double x, double z) {
    return index(x,z);
}

//Faraday rotation profile
double rotation(double x, double z){
    if(z<=d) {
        if((x>=0+center_cladding_layer/2.0)
            &&(x<=grating_spacing+center_cladding_layer/2.0)){
            return eta*magnetization_response(y_coord(x,z-d/2.0));
        }
        if((x<0-center_cladding_layer/2.0)
            &&(x>=-grating_spacing-center_cladding_layer/2.0))
        {
            return eta*magnetization_response(y_coord(x,z-d/2.0));
        }
        return 0.0;
    }
    else{
        return 0.0;
    }
}

int myround(double x){
    return (int)floor(x+0.5);
}

double gaussian(double x){
    double sigma=FWHM*sqrt(1.0/log(2.0))/2.0;
    return exp(-x*x/sigma/sigma); //centered on zero
}

double initial_profile(double x){
    return gaussian(x);
}

//fill R matrix
void fillR_l(mycomplex MM_aa[],mycomplex MM_bb[],mycomplex
MM_cc[],mycomplex MM_dd[],mycomplex MM_ee[],int z_step){
    double xcoord=0.0,zcoord=z_step*dz+z_offset;//at m,l
    for(int i=1;i<=M-1;i++){
        xcoord=i*dx+x_offset;
        MM_bb[i]=-2*beta_r;
        MM_bb[M+1+i]=-2*beta_r;

        MM_aa[i]=0.0;
    }
}

```



```

        MM_aa[M+1+i]=0.0;
        MM_cc[i]=0.0;
        MM_cc[M+1+i]=0.0;

        MM_ee[i]=-376.73431*k_0
                    *rotation(xcoord,zcoord)/index(xcoord,zcoord)*I;
        MM_dd[i]=0.002654391*k_0*rotation(xcoord,zcoord)*I;
    }
    MM_aa[0]=0.0;
    MM_aa[M]=0.0;
    MM_cc[0]=0.0;
    MM_cc[M]=0.0;
    MM_dd[0]=0.0;
    MM_dd[M]=0.0;
    MM_ee[0]=0.0;
    MM_ee[M]=0.0;

    double fill_in=1.0;
    MM_bb[0]=fill_in;
    MM_bb[M]=fill_in;
    MM_bb[M+1]=fill_in;
    MM_bb[2*M+1]=fill_in;
}

//fill S matrix
void fillS_l(mycomplex MM_aa[],mycomplex MM_bb[],mycomplex
MM_cc[],mycomplex MM_dd[],mycomplex MM_ee[],int z_step){
    double xcoord=0.0,zcoord=z_step*dz+z_offset;//at m,l
    for(int i=1;i<=M-1;i++){
        xcoord=i*dx+x_offset;
        MM_bb[i]=(-2.0)/dx/dx+k_0*k_0*index_y(xcoord,zcoord)-beta_r*beta_r;
        MM_aa[i]=1.0/dx/dx;
        MM_cc[i]=1.0/dx/dx;

        MM_ee[i]=-376.73431*k_0*beta_r
                    *rotation(xcoord,zcoord)/index(xcoord,zcoord)*I;
        MM_dd[i]=0.002654391*k_0*beta_r*rotation(xcoord,zcoord)*I;

        MM_bb[M+1+i]=(-2.0)*index(xcoord,zcoord)/dx/dx/(
            index(xcoord-dx,zcoord)+index(xcoord,zcoord)
        )
        -2*index(xcoord,zcoord)/dx/dx/(
            index(xcoord,zcoord)+index(xcoord+dx,zcoord)
        )
        +k_0*k_0*index(xcoord,zcoord)-beta_r*beta_r;
        MM_aa[M+1+i]=2*index(xcoord,zcoord)/dx/dx/(

```



```

        index(xcoord-dx,zcoord)+index(xcoord,zcoord)
    );
    MM_cc[M+1+i]=2*index(xcoord,zcoord)/dx/dx/(
    index(xcoord+dx,zcoord)+index(xcoord,zcoord)
    );
}
MM_aa[0]=0.0;
MM_aa[M]=0.0;
MM_cc[0]=0.0;
MM_cc[M]=0.0;
MM_dd[0]=0.0;
MM_dd[M]=0.0;
MM_ee[0]=0.0;
MM_ee[M]=0.0;
}

```

//tridiag method, from Numerical Recipes in C

```

void tridiag(mycomplex aa[],mycomplex bb[],mycomplex cc[],mycomplex
rr[],mycomplex uu[],int n)

```

```

{
    mycomplex bet,gam[2*M+2];

    uu[0]=rr[0]/bb[0];
    bet=bb[0];

    for (int j=1;j<=n;j++) {

        gam[j]=cc[j-1]/bet;
        bet=bb[j]-aa[j]*gam[j];
        uu[j]=(rr[j]-aa[j]*uu[j-1])/bet;

    }

    for (j=(n-1);j>=0;j--){
        uu[j]=uu[j]-gam[j+1]*uu[j+1];
    }

}

```

//Jacobi method

```

void iteration(mycomplex aa[],mycomplex bb[],mycomplex cc[],mycomplex
dd[],mycomplex ee[],mycomplex xx[],mycomplex rr[]){
    mycomplex xx_next[2*M+2];
    double error=0.0;
    int spot;

```



```

for(int nn=0;nn<n_iter;nn++){
    xx_next[0]=((-1.0)*cc[0]*xx[1]+(-1.0)*ec[0]*xx[M+1]+rr[0])/bb[0];
    xx_next[M]=(rr[M])/bb[M];

    xx_next[M+1]=rr[M+1]/bb[M+1];
    xx_next[2*M+1]=(
        (-1.0)*aa[2*M+1]*xx[2*M]
        +(-1.0)*dd[M]*xx[M]+rr[2*M+1]
    )/bb[2*M+1];

    for(int mm=1;mm<M;mm++){
        xx_next[mm]=(
            (-1.0)*aa[mm]*xx[mm-1]+(-1.0)*cc[mm]*xx[mm+1]
            +(-1.0)*ee[mm]*xx[M+1+mm]+rr[mm]
        )/bb[mm];
        xx_next[M+1+mm]=(
            (-1.0)*aa[M+1+mm]*xx[M+1+mm-1]
            +(-1.0)*cc[M+1+mm]*xx[M+1+mm+1]
            +(-1.0)*dd[mm]*xx[mm]+rr[M+1+mm]
        )/bb[M+1+mm];
    }
    error=(abs_val(xx[0].amplitude()-xx_next[0].amplitude()));//estimate error
    spot=0;
    for(int mmmm=0;mmmm<2*M+2;mmmm++){

        if(error<(abs_val(xx[mmmm].amplitude()-
            xx_next[mmmm].amplitude()))
        {
            error=(abs_val(xx[mmmm].amplitude()-
                xx_next[mmmm].amplitude()));
            spot=mmmm;
        }
    }
    for(mm=0;mm<2*M+2;mm++){
        xx[mm]=xx_next[mm];
    }
}
cout<<"\t\t"<<error<<"\t\t"<<spot<<endl;
}

//function used to output the program parameters
void write_parameters(ostream& out){
    out<<"grating_spacing: "<<grating_spacing<<endl; //spacing
    out<<"transmission_line_grating_spacing: "
        <<transmission_line_grating_spacing<<endl; //spacing

```



```

out<<"d: "<<d<<endl;
out<<"cladding_layer: "<<cladding_layer<<endl; //spacing
out<<"center_cladding_layer: "<<center_cladding_layer<<endl; //spacing
out<<"transmission_line_width: "
    <<transmission_line_width<<endl; //spacing
out<<"transmission_line_depth: "
    <<transmission_line_depth<<endl; //spacing

out<<"n_mo: "<<n_mo<<endl;
out<<"n_third_layer: "<<n_third_layer<<endl;
out<<"n_ito: "<<n_ito<<endl;

out<<"theta_f: "<<theta_f<<endl;

out<<"dx: "<<dx<<endl;
out<<"dz: "<<dz<<endl;
out<<"threshold: "<<threshold<<endl;
out<<"current: "<<current<<endl;
out<<"line1: "<<line1<<endl;
out<<"line2: "<<line2<<endl;
out<<"line3: "<<line3<<endl;
out<<"prefactor_grating: "<<prefactor_grating<<endl;
out<<"saturation_value: "<<saturation_value<<endl;

out<<"m_h: "<<m_h<<endl;
out<<"m_yi1: "<<m_yi1<<endl;
out<<"m_yi2: "<<m_yi2<<endl;
out<<"m_yi3: "<<m_yi3<<endl;
out<<"m_t: "<<m_t<<endl;
out<<"m_t1: "<<m_t1<<endl;
out<<"m_t2: "<<m_t2<<endl;
out<<"m_Hz: "<<m_Hz<<endl;
out<<"m_FWHM: "<<m_FWHM<<endl;
out<<"m_offset1: "<<m_offset1<<endl;

out<<"l: "<<l<<endl;
out<<"M: "<<M<<endl;
out<<"lambda: "<<lambda<<endl;
out<<"z_offset: "<<z_offset<<endl;
out<<"x_offset: "<<x_offset<<endl;
out<<"profile_offset: "<<profile_offset<<endl;
out<<"FWHM: "<<FWHM<<endl;
out<<"n_iter: "<<n_iter<<endl;
out<<"start_writing_data: "<<start_writing_data<<endl;
out<<"x_start: "<<x_start<<endl;
out<<"x_end: "<<x_end<<endl;

```



```

    out<<"abc_coefficient: "<<abc_coefficient<<endl;
    out<<"boundary_points: "<<boundary_points<<endl;
    out<<"reduction_x: "<<reduction_x<<endl;
}

//the following are helper functions to calculate the magnetic field distribution
double x_coord(double x,double y){
    double return_value=
        line1*x_coord_single_line(x+transmission_line_grating_spacing,y)+
        line2*x_coord_single_line(x,y)+
        line3*x_coord_single_line(x-transmission_line_grating_spacing,y);
    return return_value;
}
double y_coord(double x,double y){
    double return_value=
        line1*y_coord_single_line(x+transmission_line_grating_spacing,y)+
        line2*y_coord_single_line(x,y)+
        line3*y_coord_single_line(x-transmission_line_grating_spacing,y);
    return return_value;
}
double x_coord_single_line(double x,double y){
    double x1=x+transmission_line_width/2.0;
    double y1=y+transmission_line_depth/2.0;

    double return_value1
        =yd_atan(x1,y1)+y_atan(x1,y1)+x1_log(x1,y1)+x_log(x1,y1);

    return -prefactor_grating*return_value1;
}
double y_coord_single_line(double x,double y){
    double x1=x+transmission_line_width/2.0;
    double y1=y+transmission_line_depth/2.0;

    double return_value1
        =x1_atan(x1,y1)+x_atan(x1,y1)+yd_log(x1,y1)+y_log(x1,y1);

    return prefactor_grating*return_value1;
}

// x-coord functions
double yd_atan(double x,double y){
    if(abs_val(y-transmission_line_depth)<threshold){
        return 0.0;
    }
    return (y-transmission_line_depth)*(atan((x-transmission_line_width)
        /(y-transmission_line_depth))-atan(x/(y-transmission_line_depth)));
}

```



```

}
double y_atan(double x,double y){
    if(abs_val(y)<threshold){
        return 0.0;
    }
    return y*(atan(x/y)-atan((x-transmission_line_width)/y));
}
double xl_log(double x,double y){
    if(abs_val(x-transmission_line_width)<threshold){
        return 0.0;
    }
    return 0.5*(x-transmission_line_width)*(log((y-transmission_line_depth)
        *(y-transmission_line_depth)+(x-transmission_line_width)
        *(x-transmission_line_width))-log(y*y+(x-transmission_line_width)
        *(x-transmission_line_width)));
}
double x_log(double x,double y){
    if(abs_val(x)<threshold){
        return 0.0;
    }
    return 0.5*x*(log(y*y+x*x)-log((y-transmission_line_depth)
        *(y-transmission_line_depth)+x*x));
}
// y-coord functions
double xl_atan(double x,double y){
    if(abs_val(x-transmission_line_width)<threshold){
        return 0.0;
    }
    return (x-transmission_line_width)*(atan((y-transmission_line_depth)/(x-
transmission_line_width))-atan(y/(x-transmission_line_width)));
}
double x_atan(double x,double y){
    if(abs_val(x)<threshold){
        return 0.0;
    }
    return x*(atan(y/x)-atan((y-transmission_line_depth)/x));
}
double yd_log(double x,double y){
    if(abs_val(y-transmission_line_depth)<threshold){
        return 0.0;
    }
    return 0.5*(y-transmission_line_depth)*(log((y-transmission_line_depth)
        *(y-transmission_line_depth)+(x-transmission_line_width)
        *(x-transmission_line_width))-log((y-transmission_line_depth)
        *(y-transmission_line_depth)+x*x));
}

```



```

double y_log(double x,double y){
    if(abs_val(y)<threshold){
        return 0.0;
    }
    return 0.5*y*(log(y*y+x*x)-log(y*y+(x-transmission_line_width)
        *(x-transmission_line_width)));
}

double magnitude(double x,double y){
    /*      return sqrt(x*x+y*y);*/
    if(y>saturation_value){
        y=saturation_value;
    }
    if(y<(-1.0)*saturation_value){
        y=-1.0*saturation_value;
    }
    return y/saturation_value;
}

//the following calculates the magnetization response
double f1(double t, double y1, double y2, double y3,double m_h_x0) {
    return 175.63117453*y2*m_Hz-y1/m_t2;
}

double f2(double t, double y1, double y2, double y3,double m_h_x0) {
    return 175.63117453*(y3*h_transient(t,m_h_x0)-y1*m_Hz)-y2/m_t2;
}

double f3(double t, double y1, double y2, double y3,double m_h_x0) {
    return 175.63117453*(
        -y2*h_transient(t,m_h_x0))
        -(y3-sqrt(y1*y1+y2*y2+y3*y3))/m_t1;
}

void forward_iterate(double t, double &y1, double &y2, double &y3, double h,double
m_h_x0) {
    double k11,k12,k13,k21,k22,k23,k31,k32,k33,k41,k42,k43;

    k11=f1(t,y1,y2,y3,m_h_x0);
    k12=f2(t,y1,y2,y3,m_h_x0);
    k13=f3(t,y1,y2,y3,m_h_x0);

    k21=f1(t+0.5*h,y1+0.5*h*k11,y2+0.5*h*k12,y3+0.5*h*k13,m_h_x0);
    k22=f2(t+0.5*h,y1+0.5*h*k11,y2+0.5*h*k12,y3+0.5*h*k13,m_h_x0);
    k23=f3(t+0.5*h,y1+0.5*h*k11,y2+0.5*h*k12,y3+0.5*h*k13,m_h_x0);

```



```

    k31=f1(t+0.5*h,y1+0.5*h*k21,y2+0.5*h*k22,y3+0.5*h*k23,m_h_x0);
    k32=f2(t+0.5*h,y1+0.5*h*k21,y2+0.5*h*k22,y3+0.5*h*k23,m_h_x0);
    k33=f3(t+0.5*h,y1+0.5*h*k21,y2+0.5*h*k22,y3+0.5*h*k23,m_h_x0);

    k41=f1(t+h,y1+h*k31,y2+h*k32,y3+h*k33,m_h_x0);
    k42=f2(t+h,y1+h*k31,y2+h*k32,y3+h*k33,m_h_x0);
    k43=f3(t+h,y1+h*k31,y2+h*k32,y3+h*k33,m_h_x0);

    y1=y1+(1.0/6.0)*(k11+2*k21+2*k31+k41)*h;
    y2=y2+(1.0/6.0)*(k12+2*k22+2*k32+k42)*h;
    y3=y3+(1.0/6.0)*(k13+2*k23+2*k33+k43)*h;
}

double h_transient(double t,double m_h_x0) {
    double sigma=m_FWHM*sqrt(1.0/log(2.0))/2.0;
    return m_h_x0*(
        exp(-(t-m_offset1)*(t-m_offset1)/sigma/sigma)
    );
}

double magnetization_response(double m_h_x0){
    double t=0.0,y1=m_yi1,y2=m_yi2,y3=m_yi3;
    double convert;
    convert=m_t/m_h;
    int upper=(int)convert;
    for(int i=1;i<=upper;i++) {
        forward_iterate(t,y1,y2,y3,m_h,m_h_x0);
        t=t+m_h;
    }
    return y1;
}

```


This is the *.h file for the complex number class (called mycomplex) used in BPM-LL:

```
#if !defined
(AFX_MYCOMPLEX_H__C0247460_58E4_11D5_BB8F_00600832EC0B__INCLUD
ED_)

#define
AFX_MYCOMPLEX_H__C0247460_58E4_11D5_BB8F_00600832EC0B__INCLUDE
D_

#if _MSC_VER > 1000
#pragma once
#endif // _MSC_VER > 1000
#include <fstream.h>

class mycomplex
{
public:
    mycomplex();
    mycomplex(double x,double y);
    mycomplex(mycomplex& x);
    virtual ~mycomplex();
    mycomplex operator*(mycomplex x);
    mycomplex operator*(double x);
    mycomplex operator+(mycomplex x);
    mycomplex operator+(double x);
    mycomplex operator/(mycomplex x);
    mycomplex operator/(double x);
    mycomplex operator-(mycomplex x);
    mycomplex operator-(double x);
    void operator=(double x);
    void operator=(mycomplex x);
    void set(double x,double y);
    void setRe(double x);
    void setIm(double x);
    double Re();
    double Im();
    double amplitude();
    double phase();
    void print(ostream& output);

private:
    double r;
    double i;
};
```



```
mycomplex operator*(double a,mycomplex x);  
mycomplex operator/(double a,mycomplex x);  
mycomplex operator+(double a,mycomplex x);  
mycomplex operator-(double a,mycomplex x);  
ostream& operator<<(ostream& output,mycomplex x);  
double abs_val(double x);  
#endif
```


This is the *.cpp file for the complex number class (called mycomplex) used in BPM-LL:

```
#include "stdafx.h"
#include "mycomplex.h"
#include <iomanip.h>
#include <math.h>
#define Pi 3.14159265358979

mycomplex::mycomplex()
{
    r=0.0;
    i=0.0;
}

mycomplex::mycomplex(double x,double y){
    r=x;
    i=y;
}
mycomplex::mycomplex(mycomplex& x){
    r=x.Re();
    i=x.Im();
}

mycomplex mycomplex::operator*(mycomplex x){
    mycomplex a(r*x.Re()-i*x.Im(),r*x.Im()+i*x.Re());
    return a;
}
mycomplex mycomplex::operator*(double x){
    mycomplex a(x*r,x*i);
    return a;
}
mycomplex mycomplex::operator+(mycomplex x){
    mycomplex a(r+x.Re(),i+x.Im());
    return a;
}
mycomplex mycomplex::operator+(double x){
    mycomplex a(r+x,i);
    return a;
}
mycomplex mycomplex::operator/(mycomplex x){
    mycomplex return_value;
    double a,b,c,d,cd_or_dc;
    a=r;
    b=i;
    c=x.Re();
    d=x.Im();
```



```

        if(abs_val(c)>=abs_val(d)){
            cd_or_dc=d/c;
            return_value.set(a+b*cd_or_dc,b-a*cd_or_dc);
            return_value=return_value*(1.0/(c+d*cd_or_dc));
        }
        else{
            cd_or_dc=c/d;
            return_value.set(a*cd_or_dc+b,b*cd_or_dc-a);
            return_value=return_value*(1.0/(c*cd_or_dc+d));
        }
        return return_value;
    }
mycomplex mycomplex::operator/(double x){
    mycomplex a(r/x,i/x);
    return a;
}
mycomplex mycomplex::operator-(mycomplex x){
    mycomplex a(r-x.Re(),i-x.Im());
    return a;
}
mycomplex mycomplex::operator-(double x){
    mycomplex a(r-x,i);
    return a;
}
double mycomplex::Re(){return r;}
double mycomplex::Im(){return i;}
double mycomplex::amplitude(){
    double a=r,b=i;
    if((abs_val(a)<1e-40)&&(abs_val(b)<1e-40)){
        return 0.0;
    }
    if(abs_val(a)>=abs_val(b)){
        return (abs_val(a)*sqrt(1+b*b/a/a));
    }
    else{
        return (abs_val(b)*sqrt(1+a*a/b/b));
    }
}
double mycomplex::phase(){
    if((r>0.0)&&(i>0.0)){return atan(i/r);}
    if((r>0.0)&&(i<0.0)){return atan(i/r);}
    if((r<0.0)&&(i>0.0)){return (Pi+atan(i/r));}
    if((r<0.0)&&(i<0.0)){return atan(i/r)-Pi;}
    return 0.0;
}

```



```

void mycomplex::operator=(double x){
    r=x;
    i=0.0;
}
void mycomplex::operator=(mycomplex x){
    r=x.Re();
    i=x.Im();
}

void mycomplex::print(ostream& output){
    output<<setprecision(5)<<setiosflags(ios::fixed)<<r;
    if(i<0){}
    else{ output<<'+';}
    output<<i<<'I';
}
void mycomplex::set(double x,double y){r=x;i=y;}
void mycomplex::setRe(double x){r=x;}
void mycomplex::setIm(double x){i=x;}
mycomplex::~mycomplex()
{

}

mycomplex operator*(double a,mycomplex x){
    return x*a;
}
mycomplex operator/(double a,mycomplex x){
    mycomplex b(a,0.0);
    return b/x;
}
mycomplex operator+(double a,mycomplex x){
    return x+a;
}
mycomplex operator-(double a,mycomplex x){
    return (-1.0)*x+a;
}
ostream& operator<<(ostream& output,mycomplex x){
    output<< /*setprecision(5)<<setiosflags(ios::fixed)<<*/x.Re();
    if(x.Im()<0){}
    else{ output<<'+';}
    output<<x.Im()<<'I';
    return output;
}
double abs_val(double x){
    if(x<0) {return (-1.0)*x;}
    else {return x;}
}

```


Appendix B

The Crank-Nicolson Discretization

The BPM-LL model described in Chapter 3 uses the Crank-Nicolson scheme to discretize a system of partial differential equations (PDE), and the difference forms for the derivatives are reproduced here. For complete description of Crank-Nicolson scheme, the reader should consult references below [1,2].

The Crank-Nicolson scheme is designed for parabolic PDE's, that is, a PDE that has first order derivatives in one variable, z , and second order derivatives in another variable, x . In this scheme, all the derivatives are calculated at the coordinate $(x=m\Delta x, z=(l+1/2)\Delta z)$, where the integer l represents points in z and the integer m represents steps in x .

For an arbitrary function, f , the first order z derivatives can be replaced by

$$\frac{\partial f}{\partial z} = \frac{f_m^{l+1} - f_m^l}{\Delta z} \quad (\text{B.1})$$

and the second order derivatives with respect to x in are replaced by

$$\frac{\partial^2 f}{\partial x^2} = \frac{1}{2} \left[\frac{f_{m+1}^l - 2f_m^l + f_{m-1}^l}{(\Delta x)^2} + \frac{f_{m+1}^{l+1} - 2f_m^{l+1} + f_{m-1}^{l+1}}{(\Delta x)^2} \right] \quad (\text{B.2})$$

In addition to this simple second order derivative, a mixed second order derivative with respect to x also appears in the derivation in Chapter 3, which is of the form

$$\frac{\partial}{\partial x} D(x) \frac{\partial f}{\partial x} \quad (\text{B.3})$$

Such a derivative is replaced by

$$\frac{D_{m+\frac{1}{2}}(f_{m+1}^l - f_m^l) - D_{m-\frac{1}{2}}(f_m^l - f_{m-1}^l)}{2(\Delta x)^2} + \frac{D_{m+\frac{1}{2}}(f_{m+1}^{l+1} - f_m^{l+1}) - D_{m-\frac{1}{2}}(f_m^{l+1} - f_{m-1}^{l+1})}{2(\Delta x)^2} \quad (\text{B.4})$$

For $D=1$, equation B.4 reduces to equation B.2.

References

- [1] S. C. Chapra and R. P. Canale, *Numerical Methods for Engineers*. New York: McGraw-Hill, pp. 742-744, 1988.
- [2] W. H. Press, S. A. Teukolsky, W. T. Vetterling, and B. P. Flannery, *Numerical Recipes in C*. New York: Cambridge University Press, pp. 850, 1988.

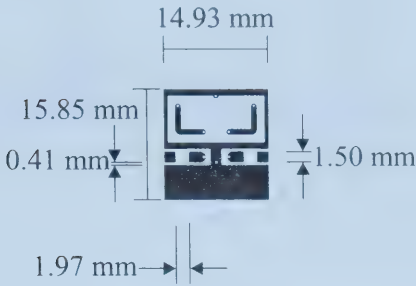
Appendix C

Photodetectors and Circuits

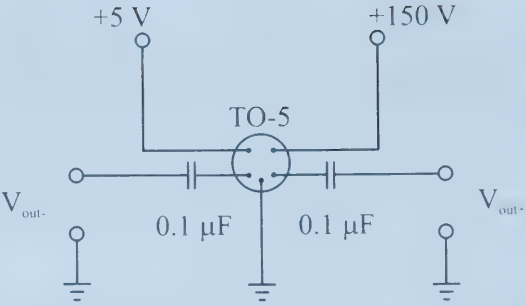
The photoreceiver used in the experiment is a Silicon avalanche photodiode with a transimpedance amplifier. The module was manufactured and prepackaged by Pacific-Silicon Sensor (part number PSS-AD230-2.3G-TO5, website: www.pacific-sensor.com).

A printed circuit board and an aluminum case were constructed to house the module. The circuit board was designed for high-frequency performance. A picture of the detector and a schematic of the mask used to create the circuit board are shown in figure C.1. While the photoreceiver unit has a differential output, it is operated in a single ended fashion, where one output is terminated in $50\ \Omega$ and the other is connected to a signal analysis device, for example an oscilloscope. The data sheet of the photoreceiver is reproduced on the following pages.

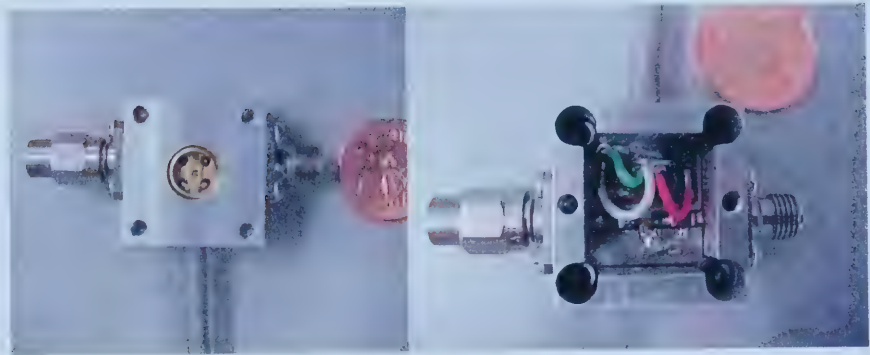
Figure C.1d illustrates a balanced diode schematic. With this configuration, currents from the opposing photodiodes are subtracted. This has the advantage of elimination of common noise between the signals from the photodiodes; however, the relatively simple design does not include any amplification, and therefore is not as sensitive as the photoreceiver module described above.



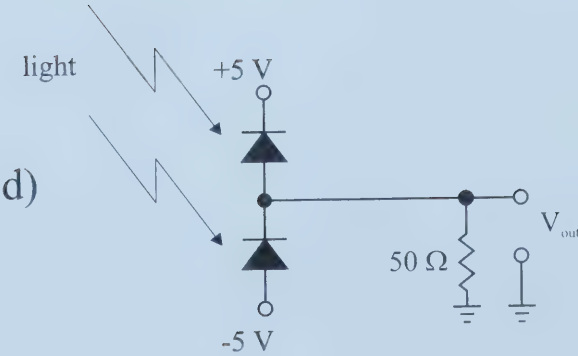
a)



b)



c)



d)

Figure C.1. a) Mask used to create the circuit board. b) Circuit schematic for the photoreceiver module. c) Picture of the front and back of the enclosure containing the photoreceiver and its circuit board. d) Balanced diode circuit schematic.



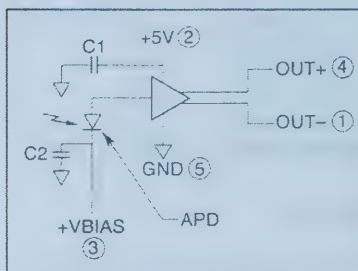
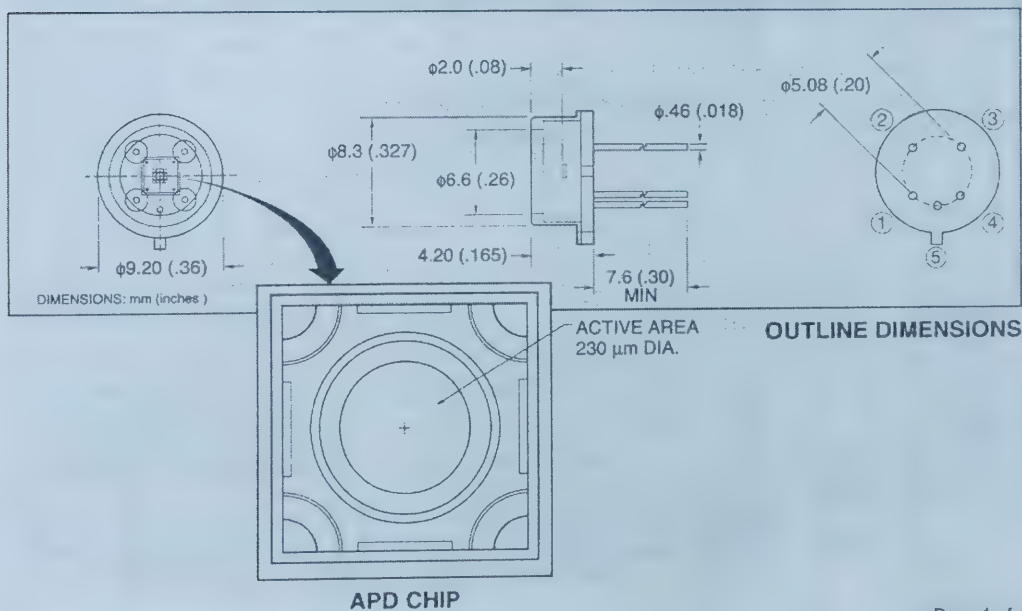
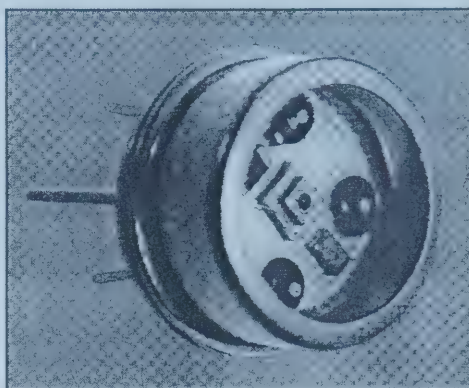
Pacific Silicon Sensor Inc.

Data Sheet


AD230-2.3G-TO5

OPTICAL DATA RECEIVER USING AN AVALANCHE PHOTODIODE AND A 2.3 GHz AMPLIFIER

AD230-2.3G-TO5 is a high frequency optical data receiver comprising an Avalanche Silicon Photodiode and a transimpedance amplifier in a hermetically sealed TO-5 package.

**SCHEMATIC DIAGRAM**

Page 1 of 4



Pacific Silicon Sensor Inc.
AD230-2.3G-T05

Data Sheet

AVALANCHE PHOTODIODE DATA

MODEL	ACTIVE AREA		V_{BR}		C_T	I_d	RESP	GAIN	T_R	CUT OFF FREQUENCY	NEP
	Dia.	mm ²	V	TC of V_{NR} (%/°C)	pF	nA	@ 780 nm A/W		ps	GHz (-3 db)	(W/Hz) ^{1/2}
AD230	230 μ m	0.42	160	0.4	1.5	0.6	0.45	200	180	2.3	1×10^{-14}

Symbols: V_{BR} - Breakdown Voltage
 C_T - Capacitance
 I_d - Dark Current
 Resp. - Responsivity (no avalanche effect)
 T_R - Rise Time
 NEP - Noise Equivalent Power

TRANSIMPEDANCE AMPLIFIER DATA

($V_{CC} = +3.0V$ to $+5.5V$, $T_A = 0^\circ C$ to $70^\circ C$, 100 Ω load between OUT+ and OUT-. Typical values are at $T_A = +25^\circ C$, $V_{CC} = 3.3V$).

PARAMETER	CONDITIONS	MIN	TYP	MAX	UNITS
SUPPLY VOLTAGE		3	5	6	V
SUPPLY CURRENT			26	50	mA
TRANSIMPEDANCE	DIFFERENTIAL, MEASURED W. 40 μ A P-P SIGNAL	1540	1900	2330	Ω
OUTPUT IMPEDANCE	SINGLE ENDED PER SIDE	48	50	52	Ω
MAXIMUM DIFFERENTIAL OUTPUT VOLTAGE	INPUT = 1mA	185	250	415	mV p-p
AC INPUT OVERLOAD		1			mA p-p
DC INPUT OVERLOAD		0.65			mA
INPUT REFERRED RMS NOISE	TO-5 PACKAGE		485	655	nA
INPUT REFERRED NOISE DENSITY	NOTE 2		11		pA/(Hz) ^{1/2}
SMALL SIGNAL BANDWIDTH	SOURCE CAPACITANCE = 0.85 pF NOTE 1	1530	1900	2420	MHz
LOW FREQUENCY CUTOFF	-3 dB, INPUT < 20 μ ADC		44		kHz
TRANSIMPEDANCE LINEAR RANGE	PEAK TO PEAK 0.95 < LINEARITY < 1.05	40			μ A p-p
POWER SUPPLY REJECTION RATIO (PSRR)	OUTPUT REFERRED, $f < 2$ MHz PSRR = -20 LOG ($\Delta V_{OUT}/\Delta V_{CC}$)		50		dB

Note 1: Source capacitance for AD230-2.3G-T05 is the capacitance of APD.

Note 2: Input Referred Noise is calculated as RMS Output Noise/ (Gain at $f = 10$ Mhz)
Noise Density Is (Input Referred Noise)/ $\sqrt{\text{bandwidth}}$

Page 2 of 4

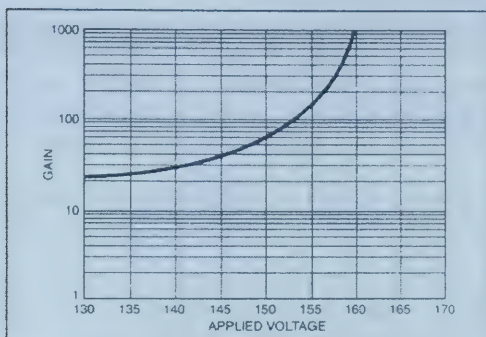
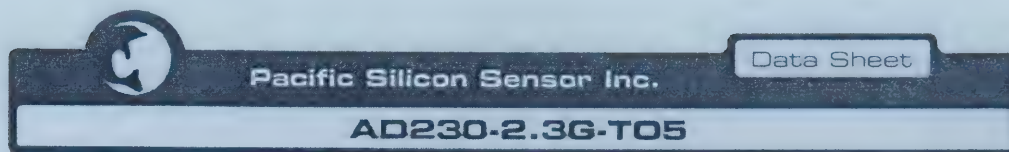


FIG. 1: APD GAIN VS BIAS VOLTAGE

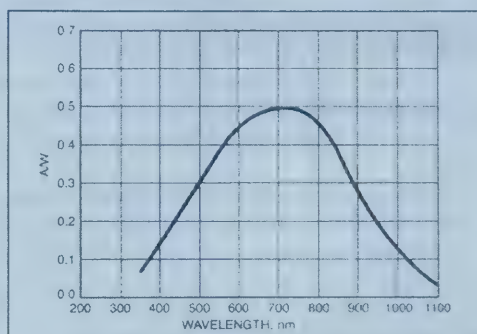
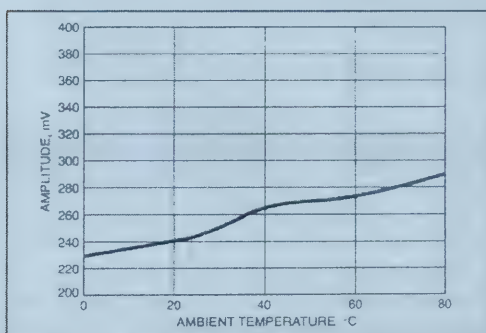
FIG. 2: APD SPECTRAL RESPONSE
(NO AVALANCHE EFFECT)

FIG. 3: AMPLIFIER OUTPUT VS TEMPERATURE

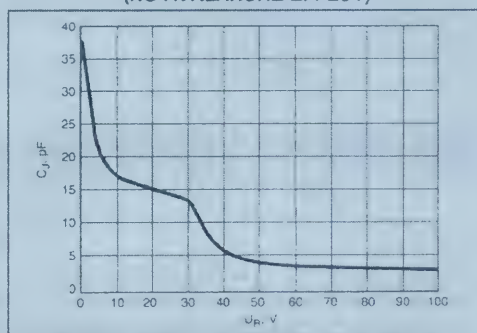


FIG. 4: APD CAPACITANCE VS VOLTAGE

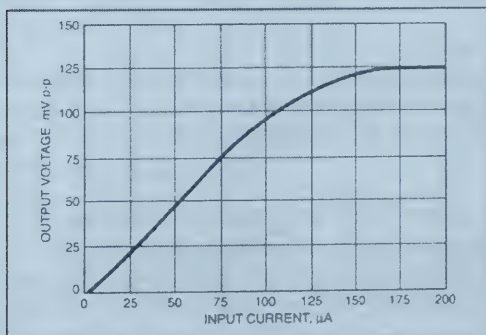


FIG. 5: AMPLIFIER TRANSFER FUNCTION

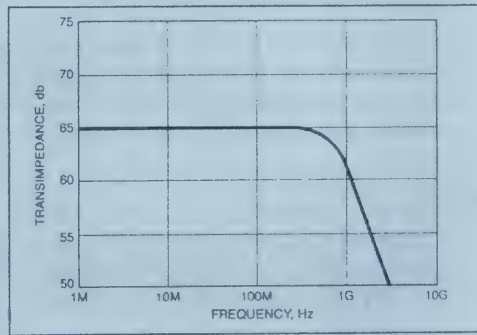


FIG. 6: TOTAL FREQUENCY RESPONSE



HIGH SPEED OPTICAL DATA RECEIVER

The circuit used is an avalanche photodiode directly coupled to a high speed data handling transimpedance amplifier. The output of the APD (light generated current) is applied to the input of the amplifier. The amplifier output is in the form of a differential voltage pulsed signal.

The APD responsivity curve is provided in Fig. 2. The term Amps/Watt involves the area of the APD and can be expressed as Amps/mm²/Watts/mm², where the numerator applies to the current generated divided by the area of the detector, the denominator refers to the power of the radiant energy present per unit area. As an example assume a radiant input of 1 microwatt at 850 nm. The APD's corresponding responsivity is 0.4 A/W.

If energy in = 1 μ W, then the current from the APD = $(0.4 \text{ A/W}) \times (1 \times 10^{-6} \text{ W}) = 0.4 \mu\text{A}$.
We can then factor in the typical gain of the APD of 100, making the input current to the amplifier 40 μA .

From Fig. 5 we can see the amplifier output will be approximately 40 mV p-p.

APPLICATIONS NOTE

The AD230-2.3G-TO5 is a high speed optical data receiver. It incorporates an internal transimpedance amplifier with an avalanche photodiode.

This detector requires +3.5V to +5.0V voltage supply for the amplifier and a high voltage supply (100-180V) for the APD. The internal APD follows the gain curve published for the AD230-TO52i avalanche photodiode. The transimpedance amplifier provides differential output signals in the range of 200 millivolts differential.

In order to achieve highest gain, the avalanche photodiode needs a positive bias voltage (Fig. 1). However, a current limiting resistor must be placed in series with the photodiode bias voltage to limit the current into the transimpedance amplifier. **Failure to limit this current may result in permanent failure of the device.** The suggested initial value for this limiting resistor is 390 k OHM.

When using this receiver, good high frequency placement and routing techniques should be followed in order to achieve maximum frequency response. This includes the use of bypass capacitors, short leads and careful attention to impedance matching. The large gain bandwidth values of this device also demand that good shielding practices be used to avoid parasitic oscillations and reduce output noise.

Caution: These parts are extremely static sensitive. Standard ESD precautions must be followed.

Page 4 of 4

B52450